Master's thesis

NTNU
Norwegian University of Science and Technology
Faculty of Information Technology and Electrical Engineering
Department of Engineering Cybernetics

Tora Grenness Haga

The Ultrasound Cardiac Supercycle - for high temporal *and* spatial resolution

Master's thesis in Cybernetics and Robotics
Supervisor: Lasse Løvstakken
Co-supervisor: Solveig Fadnes & Thomas Grønli
June 2021

NTNU
Norwegian University of
Science and Technology

Tora Grenness Haga

The Ultrasound Cardiac Supercycle - for high temporal *and* spatial resolution

Master's thesis in Cybernetics and Robotics
Supervisor: Lasse Løvstakken
Co-supervisor: Solveig Fadnes & Thomas Grønli
June 2021

Norwegian University of Science and Technology
Faculty of Information Technology and Electrical Engineering
Department of Engineering Cybernetics

NTNU
Norwegian University of
Science and Technology

Abstract

Cardiac ultrasound is widely used for the investigation and detection of cardiovascular diseases as it is a non-invasive medical imaging method that gives data on the structure and function of the heart. Increasing the performance and applicability of cardiac ultrasound possesses potential benefits, as cardiovascular disease represents one of the major causes of death worldwide.

As the physical principles of ultrasound waves introduce a trade-off between spatial- and temporal resolution, ultrasound recordings are often limited in applicability. This thesis aims to create an ultrasound recording of a cardiac cycle, the Supercycle, having both a high spatial resolution and a high frame rate. It further studies the influence of sample rate and data foundation for high performance.

The Supercycle is composed of several consecutive cycles. The cycles are normalized, joined, and further remapped to a uniform time grid by data fitting with cubic B-splines. Simple post-processing methods, as image alignment, are analyzed for the potential of further robustness. The Supercycle is tested and evaluated on brightness mode images (B-mode) and for color flow imaging (CFI).

A Supercycle of 2D duplex triplane ultrasound recordings was increased from 14 Hz to 140 Hz. Results of B-mode acquisition increased the frame rate to $\sim$ 650 Hz and for CFI frame rates of $\sim$ 250 Hz were obtained. As the Supercycle increased most frame rates on a scale of 10, the trade-off between smoothness of the result and flickering artifacts appeared. A further study of the alignment of frames is potentially a solution to overcome the trade-off.

Sammendrag

Hjerteultralyd er en ikke-invasiv medisinsk avbildningsmetode som gir informasjon om hjertets struktur og funksjonsevne. Det er derav en mye brukt metode for å undersøke og oppdage hjerte- og karsykdommer. Ettersom slike sykdommer utgjør en av de største dødsårsakene over hele verden er økt ytelse og anvendelighet av hjerteultralyd fordelaktig.

De fysiske prinsippene som danner grunnlaget for ultralydopptak gjør at en ofte må velge mellom høy romlig oppløsning og høy tidsoppløsning. Dette utgjør en begrensning for anvendbarheten av hjerteultralyd . Denne masteroppgaven ønsker å konstruere et ultralydopptak av en fullstendig hjertesykel, en Supersykel, der både høy bildekvalitet og høy bildefrekvens er ivaretatt. Videre er det gjort undersøkelser på innflytelsen av samplingsfrekvensen og datagrunnlaget. En Supersykel er satt sammen av opptak fra flere påfølgende sykler. Syklene normaliseres og sammenføyes før kubisk B-splines brukes for datatilpassing til et uniformt tidsgrid. Enkel prosessering av data før konstruksjonen av Supersykelen er testet for å undersøke det videre potensialet for en høyere ytelse. Dette innebærer blant annet bildejustering for et konsekvent synsfelt. Supersykelen er testet og evaluert for både gråtonebilde (B-mode) og fargedoppler (CFI).

En Supersykel på et 2D dupleks triplan ultralydopptak ble økt fra 14 Hz til 140 Hz. For B-mode opptak ble bildefrekvensen økt til $\sim$650 Hz og for CFI ble det oppnådd bildefrekvenser på $\sim$250 Hz. Selv om Supersykelen klarte å øke bildefrekvensen med en faktor på 10, ble det oppdaget at en avveining mellom jevne overganger og flimrende artefakter må gjøres. Ved å videre undersøke en metode for bildejustering som gir konsekvente synsfelt kan en potensielt løse dette problemet.

Preface

The following thesis denotes the final work completing the degree of Master of Science at the Department of Engineering Cybernetics at the Norwegian University of Science and Technology (NTNU), Trondheim. The study was conducted at the Department of Circulation and Medical Imaging. The thesis is a further study of the writer's project thesis completed fall 2020. Some sections in the current thesis comprise parts, either directly or revised, from the project thesis.

I would like to express my appreciation to the people guiding me through the process of the thesis. A special thanks to my supervisor Professor Lasse Løvstakken, and co-supervisors Solveig Fadnes and Thomas Grønli, in addition to Morten S. Wigen, at the Department of Circulation and Medical Imaging, NTNU. Your enthusiasm for the project, solid feedback, and valuable knowledge of the field and frameworks, made the process profoundly rewarding. I also want to give some extra credit to Thomas, as I am grateful for his ability to explain and visualize complex concepts, in addition to the work he put down for making Tensorspline a valuable framework used in the Supercycle. I also thank David Pasdeloup for an introduction of the ultrasound machine learning package, in addition to Bjørnar Grenne, Håvard Dalen, Håkon Pettersen, and Sigbjørn Sæbø, who put time and effort into providing useful data materials.

Contents

List of Figures

List of Tables

1 Introduction

1.1 Motivation

A report from the European Society of Cardiology from 2019 states that Cardiovascular disease (CVD) is the most common cause of death for the population of its 56 member countries [1]. In the Norwegian population is approximately 1/5 currently living with CVD or with a high risk of developing it. In addition, 1.1 million Norwegian citizens are using therapeutic medicine for treatment and prevention of CVD [2]. CVD also affects children, being the most common congenital disease in Norway where 500 - 600 babies are born with this disease each year [3]. Predictions state further that an increase in CVD is expected in the future as most people suffering from the disease are over 60 years of age, the population lives longer, and the post-war generation ages.

Ultrasound of the heart, echocardiography, is an important element in the process of discovering CVD as it is non-invasive and provides vital information of the function and structure of the heart. Echocardiography gives qualitative information of e.g. the ventricular motion, cardiac valve motion, pumping capacity, and location of damaged tissue. In addition, can quantitative measures such as blood velocities, and potentially pressure gradients be found through analysis of Doppler ultrasound [4].

With small structures and rapid movement, the heart is a challenging organ to image. Especially challenging is imaging the hearts in small animals, such as mice, which are often used in research of human diseases [5]. Another important application is capturing detailed images and precisely calculating quantitative measures for children. As children also have smaller biological structures and three times higher heart rates than adults the achievable resolutions restrict the image quality.

Due to the physical principles of sound waves, high spatial resolution often comes at the cost of lower frame rates, an inevitable trade-off in the field of echocardiography. State-of-the-art frame rates for B-mode ultrasound are $\approx$ 30 - 60 Hz [6] while CFI rates are $\approx$ 9 - 30 Hz depending on sector size, imaging depth, and the number of transmitted waves. However, for a combination of B-mode and CFI, the duplex mode, the frame rate is often below 15 Hz. For detailed functional descriptions and valid calculation of quantitative metrics [7] [8], research indicates the desired frame rate to be $>$ 200 Hz for B-mode and $>$ 60 Hz for CFI.

Ultrafast ultrasound was proposed as a solution to increase the low frame rates from normally being about 30 Hz to frame rates of 2.5 kHz [9]. However, such methods often suffer from compromised spatial resolution and low signal-to-noise ratio (SNR). In addition, the methods often require changing the physical setup of the ultrasound examination, limiting their applicability. Retrospective methods for increasing the temporal resolution show satisfactory results when used for Magnetic resonance imaging (MRI) [10] and Computer tomography scan (CT scan) [11]. It is deployed and tested for cardiac ultrasound, but mostly for 3D acquisition where i.e. long processing times are required [12] [13] [14]. The retrospective methods increase the frame rates by post-processing the recordings, giving neither limitation during acquisition nor in the examination setup. Increased computer processing capabilities enable such complex image processing without delaying the real-time acquisition. In addition, the retrospective method applies to already recorded data, meaning it can be deployed on old datasets.

1.2 Contributions

The thesis encompasses a method for increasing the frame rate in cardiac ultrasound imaging while simultaneously preserving the spatial resolution. It further uncovers circumstances of importance regarding the sample rate and the data foundation of the method.

The ultrasound cardiac Supercycle is constructed by combining consecutively recorded cycles by retrospective gating. An offset between samples from consecutive cycles occurs when the *sample rate is not a multiple of the heart rate*. Joining samples from several cycles increase the overall number of samples giving a higher frame rate. The idea is thus requiring that samples from different cycles falls at different normalized time. The idea is visualized in Figure 1. The thesis also provides investigations of the relationship between heart rate and sample rate for optimal collection of new information.

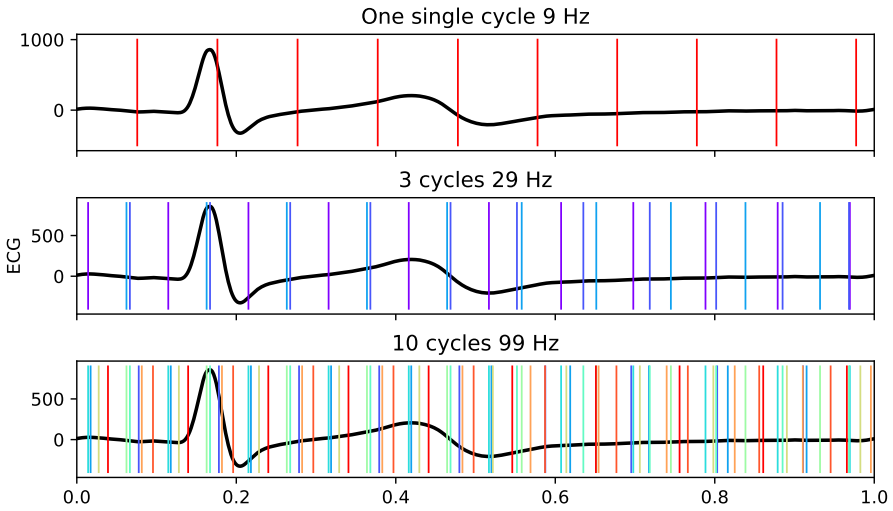

Figure 1: The dataset is originally sampled with a frame rate of 9 Hz. The frame rate is increased to 99 Hz after combining 10 cycles and has increased the temporal information seen by a better coverage of the overall cycle.

A study of the framework for creating a Supercycle is performed, in addition to a proposition of a resulting setup. The settings comprise methods for retrospective gating in time by both ECG and novel timing information from machine learning. Machine learning is further used for feature localization which is vital for quantitative metrics in outlier detection and data stability measures. A uniform time grid for Supercycle is ensured by remapping its time axis by data fitting with higher order B-splines.

The Supercycle is tested on in-vivo ultrasound data containing both the Brightness modality (B-mode) and Color Flow Images (CFI). Evaluation is performed using Motion mode (M-mode) and 2D images, in addition to quantitative metrics and human inspection of video streams.

The goal of the method is to increase the frame rates to a scale where the detailed movement of the mitral valve is visible in B-mode, and the blood flows in CFI. Especially in the case of three plane duplex acquisition (triplane) the state-of-the-art sample rates are particularly low. The thesis specifically aims to increase triplane acquisition in proportion to the amount of recorded cycles to the range of 50-150 Hz.

1.3 Related work

The two following sections give an overview of related research and state-of-the-art methods relevant to the thesis. The part about Electrocardiogram (ECG) gating is adapted from the project thesis [15].

1.3.1 Ultrafast Ultrasound

Temporal resolution depends on the number of transmit events used to construct a single frame. The transmit events are again dependent on the physical principles of wave transmission, such as the constant speed of sound in addition to the fixed depth and size of the captured heart. The dependencies motivate the reduction of transmit events to increase the frame rate. Reducing the number of transmit events will either limit the field of view (FOV) or reduce the spatial resolution [9]. As a result, this gives insufficient imaging quality for several applications.

The concept of ultrafast ultrasound imaging was already proposed in the late 1970s [16]. Current state-of-the-art use multiline acquisition (MLA) where several neighboring lines are constructed simultaneously by only one transmit beam introduced, a concept introduced in the 1980s [17]. MLA requires broadening of the beam to ensure that the physical sector, captured by the neighboring receive lines, is sufficiently covered. Broadening of the beam is performed by decreasing the active aperture on transmit, resulting in a less focused transmit beam and some lack of spatial resolution and SNR. A common setup is using 4 receive lines per transmit line, resulting in a so-called 4MLA and a 4-fold increase in frame rate (approx. 130 Hz for a 90° sector) [9].

MLA could potentially be combined with multiline transmit imaging (MLT), a method that transmits several focused beams simultaneously. It is essential in MLT to ensure that the transmitted beams are non-overlapping, to avoid having artifacts due to interference between simultaneously transmitted beams. However, without such artifacts is MLT providing increased spatial information over MLA, causing the combination of these methods to give sufficient resolution in both space and time [18].

For a further increase in frame rate, are plane wave imaging (PWI) or diverging wave imaging (DWI) applicable. For phased-array transducers, DWI transmits a defocused pulse covering a wide region of interest (beyond the transducer width). It is possible to reconstruct several (or all) lines in parallel with a diverging wave, resulting in frame rates up to 5000 Hz [6] [19]. Less energy is however transmitted in each direction causing reduced spatial resolution and SNR. Coherent spatial compounding of diverging waves was proposed to overcome the issue, where the same area is captured at different locations and averaged in the resulting image [20]. Coherent spatial compounding of DWI with a sufficient overall resolution again reduces the frame rate to approximately the same as 4MLA [9].

ECG gating has been a proposed method for increasing the frame rate in ultrasound imaging. With the use of ECG data, a high temporal representation of a cardiac cycle can be constructed by a combination of sub-images retrieved from consecutive cardiac cycles [9]. The ECG can provide trigger points for the different parts of the cardiac cycle, i.e. diastole and systole. Current research has examined a prospective method where a large imaging sector is divided into several sub-sectors, which all are acquired at a high frame rate for one cycle each. The sub-sectors are then aligned by the gating of these ECG trigger points into recreating the original large imaging sector [5] [7]. ECG

gating relies heavily on the precise alignment of frames between sub-sectors to avoid artifacts. The method also has a trade-off between the number of subsectors combined and the resulting frame rate suffers from challenges for patients with heart rate variability as this inconsistency in heart rate will propagate as artifacts in the combined sector.

Both prospective and retrospective ECG gated methods are commonly used for both MRI and CT imaging [11]. However, in CT imaging is retrospective gating suffering from high radiation doses [11], which has increased the research of prospective gating. Prospective gating in ultrasound gives cardiac images only for a small part of the cardiac cycle, this reduces the temporal information of e.g. the cardiac valve motion and is not desirable.

Kellman et al.[10] propose a similar method as the Supercycle, for MRI. The method is a retrospective reconstruction of a full cardiac cycle from images acquired over multiple heartbeats during free breathing [10]. Kellman et al. use a tolerance window to discard frames with a high influence of respiratory motion. The procedure shows promising results with high temporal resolution and high SNR, also in the case of free-breathing and in the presence of arrhythmias.

1.3.2 Interpolation for frame rate up conversion

Video frame interpolation aims to improve the frame rate and the visual quality by constructing intermediate frames in the video stream. The method is researched for multiple applications, such as video compression, increased frame rates for video games and real-time videos, slow-motion generation, and additional video editing tools. Optical Flow (OF), Convolutional Neural Networks (CNNs), and a combination of the two are commonly used for the intermediate frame calculations in video frame interpolation.

RIFE, a Real-time Intermediate Flow Estimation algorithm comprises a recent study in video frame interpolation, utilizing a combination of a neural network, IFNet, and supervision for estimating the intermediate frames. RIFE shows impressive results for real-time flow-based interpolation methods [21]. For medical imaging, simple interpolation methods such as frame repetition or linear interpolation can be sufficient when having small variations in motion but might introduce blurring and other artifacts for rapidly moving objects. Thus, Mirarkolaei et al. [22] propose a method of motion-compensated frame interpolation in real-time, where the motion of the object is taken into consideration when interpolating the intermediate frame. The method calculates the Euler-Lagrange equations to get the optimal motion field and uses an iterative procedure to get intermediate frames. The results show fewer artifacts due to blurring in rapidly moving objects and an increased SNR.

2 Background

The following section presents background material as an introduction to concepts used throughout the thesis. The material comprises ultrasound theory and applications, anatomy and functionality of the heart, and relevant mathematical concepts. The sections 2.1, 2.3, 2.4 and 2.5 are partly adapted from the project thesis [15].

2.1 Theory of Ultrasound Imaging

2.1.1 History

The concept of echolocation originates from the Italian physiologist and priest Lazzaro Spallanzani (1729-1799) who discovered how bats used sound to navigate [23]. Bats calculate the location of objects in their surroundings by sending high-frequency sound, ultrasound, that causes reflection at the objects, known as echoes. In 1842 the concept of the Doppler effect on light waves was first described by the physicist Christian Doppler (1803-1853). The concept describes a shift in the frequency spectra of light waves when the light source is moving relative to the observer. The Doppler effect, or Doppler shift, was later proven to also apply to sound waves, making both distance and velocity measurements of objects by ultrasound waves possible. With the tragedy of the sinking ship Titanic in 1912, ultrasound was investigated as a method for underwater collision avoidance. The method was further developed for submarines in both first- and second World War [23] [24]. With the discovery of the piezoelectric materials by the Curie brothers, the frequency of the ultrasonic waves increased [25]. Increased frequencies made the concept of echolocation with ultrasound applicable for medical examination as the medical field required higher frequency spectera. In the 1950s the first research in medical ultrasound was conducted. These studies included the first cross-sectional images, tissue differentiation for cancer detection, closed head imaging, and recordings of the heart valves [26]. Accordingly, with all these discoveries at hand, the field of medical ultrasound showed promising results in terms of imaging performances, cost-effectiveness, and safety restrictions.

2.1.2 Ultrasound physics

Ultrasound is longitudinal sound waves with frequencies over the audible range. The typical range of ultrasound frequencies in a medical examination is between 2.5-10 MHz, where in comparison humans can hear sound with frequencies between 20 Hz and 20,000 Hz.

The ultrasound waves can be described by the relation of wavelength, frequency, and propagation speed given as

$$\lambda = \frac{c}{f}, \tag{2.1}$$

where λ is the wavelength (distance between sound waves), f is the frequency (number of cycles per second) and c is the propagation speed (the speed at which the waves travel through the medium). The propagation speed is approximately constant through most body tissue and commonly used as 1540 m/s.

When an ultrasound wave propagates through a non-homogeneous medium it causes reflected waves as it hits tissue boundaries. The reflections are due to differences in acoustic impedance between different biological tissues, and the reflected wave is varying in amplitude corresponding to the magnitude of the (relative) difference. The distance between a wave source and a tissue boundary can be calculated by the propagation speed and the time-of-flight. Time-of-flight is the time it takes from the wave is transmitted from the source to the reflected wave is received at the source.

An ultrasound transducer can transmit and receive ultrasound waves, and by sending a pulse it is possible to obtain a scanline through a medium. The scanline shows the distance and amplitude of reflected boundaries and is the building block of all ultrasound modes. By sending waves in multiple directions it is possible to i.e. create 2D images of the medium by concatenating the corresponding scanlines.

The transducer usually transmits ultrasound waves in pulses to be able to correctly determine the distance of the reflected waves. This compromises a limit in the pulse repetition frequency (PRF) such that the time between consecutive pulses is larger than the time it takes to travel twice the distance, d, to the point of interest,

$$PRF < \frac{c}{2d}. \tag{2.2}$$

If PRF is chosen too high, we cannot distinguish the reflected waves, possibly resulting in wrong distance calculations [27](chapter 1).

2.1.3 Doppler ultrasound physics

An object in motion will create a frequency shift between the transmitted and received ultrasound wave, described as the Doppler effect. The frequency shift happens as the waves are either compressed or expanded in contact with a moving object. The Doppler frequency shift, f_d in equation (2.3), can be used to measure the velocity of the moving object.

$$f_d = 2f_0 \frac{v \cos\theta}{c}, \tag{2.3}$$

where f_0 is the center frequency of the transmitted wave, c is the speed of the ultrasound wave, v is the velocity of the scatterer and θ is the angle between the ultrasound beam and the scatterer velocity direction [26]. By this concept, it is possible to measure the velocity of the blood cells and investigate the blood flow through the cardiac cycle.

From the Doppler frequency shift equation (2.3) the following relation can be found

$$v = \frac{c}{2\omega_0 T}\bar{\omega}, \tag{2.4}$$

where $\bar{\omega}$ is the mean angular frequency, ω_0 is the transmitted angular frequency and T is the sampling interval. By estimating the autocorrelation function we can find $\bar{\omega}$ as

$$\bar{\omega} = \angle R(1). \tag{2.5}$$

For a time-discrete process where $z(n)$ is a complex sample at time $t = nT$, and T is the sampling interval we can write the auto-correlation function as

$$R(\tau) = E[z(t+\tau) \times z^*(t)], \tag{2.6}$$

where τ represents the time lag between t_1 and t_2. The power spectrum is the Fourier transform of the auto-correlation function $R(\tau)$ is given as $G(\omega)$ [28]. From these relations we can find a auto-correlation estimator at $\tau = 1$

$$R(1) = \frac{1}{2\pi} \int_{-\pi}^{\pi} G(\omega) e^{i\omega} d\omega. \tag{2.7}$$

With a scaling factor we then obtain the mean velocity in [m/s] by

$$v = \frac{cPRF}{4\pi f_0} \angle R(1), \tag{2.8}$$

where PRF is the inverse of the sampling interval T for pulsed-wave Doppler.

The limitation in PRF described in equation (2.2) also limits the maximum measurable blood velocity given by the Nyquist sampling theorem. Doppler shifts greater than $\frac{\text{PRF}}{2}$ will give rise to aliasing artifacts in the Doppler measurements. The PRF limits the maximum measurable blood velocity to

$$v_{nyq} = \frac{cPRF}{4f_0}. \tag{2.9}$$

2.1.4 Views and modes

As the heart is located behind the ribs, the ultrasound probe is placed to avoid having the ribs as a part of the view and to reduce the acoustic shadowing effect from such strong reflective tissues. Four commonly used positions are the parasternal, the apical, the subcoastal, and the suprasternal position. These all produce different views by tilting and rotating the probe [27](chapter2). For the current thesis, the Apical 4-Chamber (A4C) view is mostly used as seen in Figure 2.

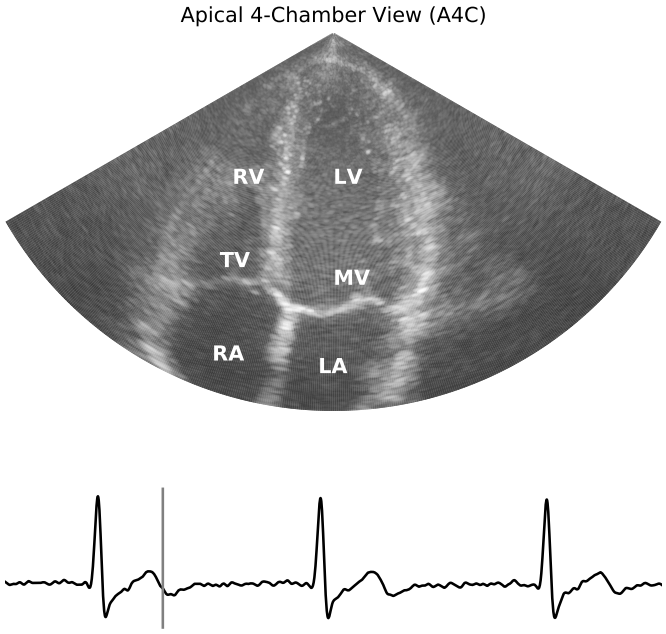

Figure 2: A4C view shows the left ventricle (LV), right ventricle (RV), left atrium (LA), right atrium (RA), mitral valve (MV) and tricuspid valve (TV). The ECG graph indicates where in the cardiac cycle the A4C view is obtained.

B-mode images are produced by multiple scanlines in different directions resulting in a two-dimensional (2D) image of the structures of the heart. The scanlines are obtained by electronically steered phased array transducers and the amplitude of the reflected waves are interpreted as a brightness value (between 0-255).

In M-mode echocardiography a single scanline is manually steered towards the reflecting structures of interest. M-mode displays the distance to the structures on the y-axis and the recorded time on the x-axis. With M-mode changes of structures at a particular direction or slice are observed over time.

CFI echocardiography visualizes blood velocity and direction in 2D. The 2D image is colored red for blood particles traveling towards the probe and blue for blood particles traveling away from the probe. CFI is not able to capture neither perpendicular movement nor velocities above the Nyquist limit.

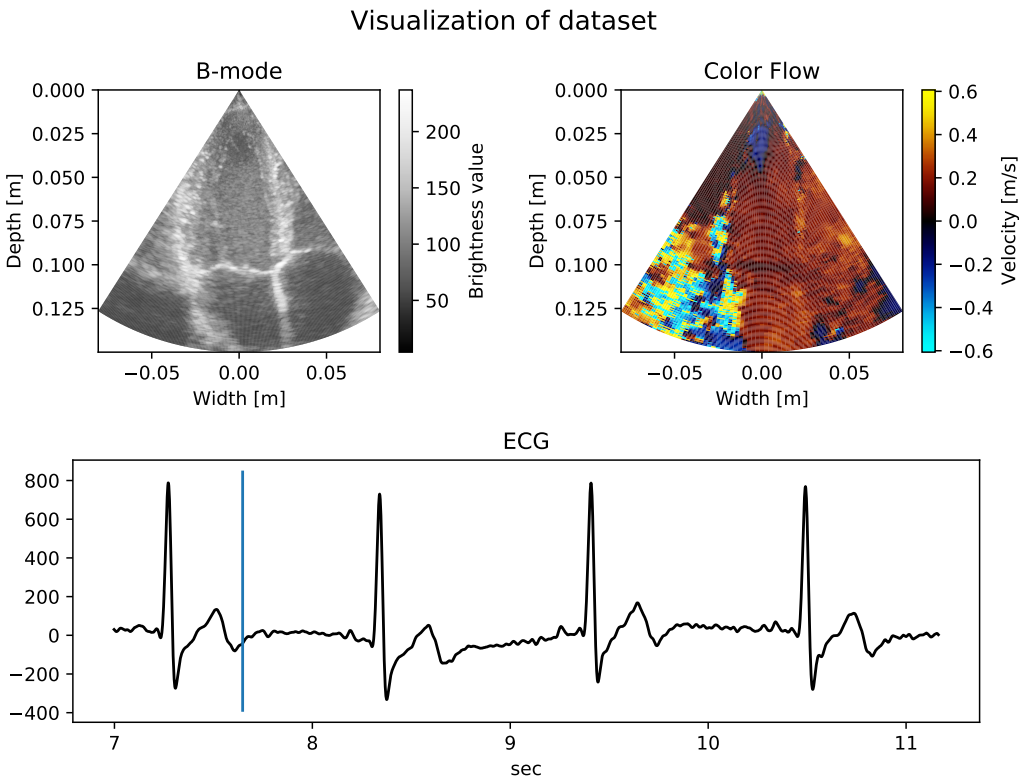

Figure 3: Visualization of one dataset containing B-mode data, CFI data and ECG signal. The B-mode data shows brightness levels corresponding to the reflection of a tissue boundary. The CFI data shows blood flow, where the red color is velocities towards the transducer and blue color is velocities away from the transducer. The ECG data is used for timing purposes, here showing which frame in the dataset that is visualized in the B-mode data and CFI data.

The combination of modes and views gives multiple applications such as Duplex and Triplan imaging. A Duplex image is a combination of a B-mode and a CFI image. It is obtained by masking the CFI image and use it as a layer on top of the B-mode image. The masked CFI contains only the velocities of the blood particles and has removed all velocity information from the surrounding tissue. Triplan imaging is images from three planes of the heart for the same cardiac cycle. The planes obtained are the A4C in addition to Apical 2-Chamber (A2C) and Apical Long Axis (ALAX).

2.1.5 Limitations and artifacts

Physical background for obtained frame rate The typical round-trip propagation distance in cardiac ultrasound imaging is ∼30 cm, which at a velocity in soft tissue, ∼1540 m/s, causes a measurement time for one beam to be ∼200 μs. About 180 beams in different directions are measured in a conventional 2D cardiac image sector of 90°. The total time for one sector scan is thus 36 ms, meaning ∼28 frames per second [9]. Similarly, to obtain a color flow map with the round-trip propagation distance still being ∼30 cm, with 50 scan lines repeated 10 times we achieve a temporal resolution of ∼10 Hz [29].

These frame rates are not feasible for several cardiac examinations but originate directly from the physical principles of ultrasound imaging. A high-frame rate is required for early detection of

cardiac disease in the case of fast movement and detailed observations. With the acquired frame rate of 2D cardiac imaging being ∼28 Hz, we need to scale it by ∼6 to reach the goal of 200 Hz. Such an increase in frame rate could be achieved by reducing the number of scan lines in the imaging acquisition. However, reducing this number is also reducing either the sector width or the spatial resolution. These performance goals and the physical background of ultrasound imaging comprise the foundation of challenge in ultrafast ultrasound.

Resolution vs. penetration High spatial resolution is desirable to distinguish details. The minimum spatial resolution of ultrasound images is defined as approximately one-half of the wavelength of the transmitted wave. The resolution is improved by increasing the frequency, which is the inverse of the wavelength. However, high-frequency waves are more attenuated as they propagate through tissue, giving a decreased penetration depth. For shallower imaging, e.g. hearts in children, high-frequency waves can be used to obtain higher spatial resolution while achieving sufficient penetration depth. However, for adults, such high-frequency waves cannot be used to image the deepest segments of the heart due to attenuation. The described challenge gives rise to the trade-off between spatial resolution and penetration depth.

Aliasing artifacts The relation in equation (2.9) gives the velocity range in which the ultrasound machine can correctly calculate the true velocities. Outside this range the velocities are exceeding the Nyquist velocity limit, creating difficulties calculating the velocity and flow direction of the blood particles. The artifacts are seen in CFI images as incorrectly colored velocities and directions from the true velocities.

If we increase the PRF we increase the possibility to measure higher velocities. However, increased PRF is firstly limited due to the relation in equation (2.2), and secondly it limits the sensitivity to low velocities. This is due to the higher similarity between the Doppler shifts between the low velocities and the tissue Doppler shifts, which will cause the low velocities to be potentially removed by the clutter filter.

Clutter filtering, dropouts and flashing artifacts The information of interest in Color Flow Doppler is from blood particles. Clutter filters are needed to remove acoustic noise from surrounding tissue. High-pass filters are commonly used to remove the signals of nearly stationary tissue, as these will have lower Doppler shifts than the faster-moving blood particles. However, clutter signals often have significantly larger signal power than blood (in size range of 70-80 dB larger) [30]. The high signal power of stationary tissue requires high stop-band attenuation, but due to limited sample per packet in CFI imaging, the high-pass filters are non-ideal as the filter order is restricted to this packet size. As a result, the CFI image is potentially suffering from attenuation of blood signals, called clutter filter dropouts, and improper coloring of areas with tissue, called flashing artifacts.

Respiratory motion artifacts Respiratory motion is movement in the thorax and abdomen during free breathing. Such motion artifacts caused by respiratory motion are known challenges in CT and MR imaging, but less discussed in the field of ultrasound imaging [31]. The easiest solution to overcome respiration is for the patient to hold their breath. However, breath-holding limits the image acquisition time to around 30 sec which in several applications is not satisfactory.

Another proposed solution is respiratory gating, where the acquisition of images is only conducted at specific times during the respiratory cycle. However, this method also puts restrictions on the acquisition time. Motion tracking of the region of interest is also a proposed solution, where the tracking can be used as a tool for motion correction. Other applications implant a marker into the region and track it with i.e. X-ray which makes the procedure invasive [31], however, meaning all the methods are either compromising the time schedule or the non-invasive advantage of using ultrasound.

2.2 The Cardiac Cycle

The functionality of the heart is to provide each organ in the human body with oxygenated blood. The human heart consists of two parts as seen in Figure 4, the right heart chamber and the left heart chamber. Both chambers have an atrium and a ventricle, in addition to two valves each. The right heart chamber receives oxygen-depleted blood and leads it into the lungs to be concentrated with oxygen and CO2 to be removed. The left heart chamber takes the re-charged blood from the lungs and pumps it back out to the organs. The process of filling and pumping is repeated and together composes the cardiac cycle.

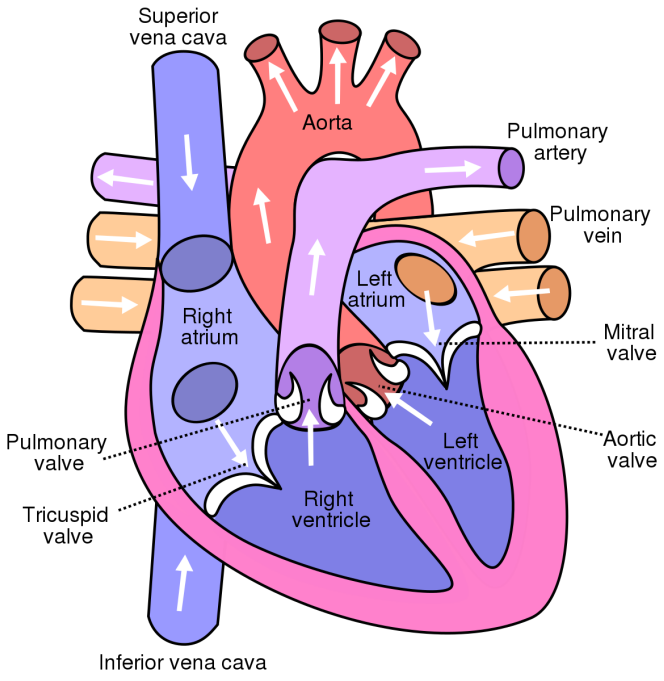

Figure 4: An illustration of the human heart with its chambers, valves, veins and arteries [32].

The cardiac cycle can be described both by mechanical events and electrical events as seen in Figure 5. The mechanical cycle is usually divided in two main phases: *the systole* and *the diastole*.

Isovolumetric contraction is the first part of systole where the pressure of the left ventricle (LV) increases without any change in its volume. The aortic valve (AV) opens when the LV pressure reaches the aortic pressure, leading to *ejection* which ends when AV again closes.

From the closure of AV to the opening of the mitral valve (MV) is the part called *isovolumetric relaxation* and marks the start of the diastole phase. The pressure of the LV decreases with

no change in volume, and the relaxation part ends when the LV pressure reaches the left atrial pressure. In *early diastolic filling* MV opens starting rapid filling of LV. The pressure gradient between the left atrium (LA) and LV decreases and stops the rapid inflow in LV early in diastole. In the following part, *the diastasis*, the pressure in LA and LV reaches equilibrium almost stopping mitral inflow. *Atrial systole* starts when the left atrium contracts and the pressure increases, which again changes the pressure gradient leading to a second flow into LV. After atrial relaxation, the pressure again decreases which closes MV and ends diastole [33].

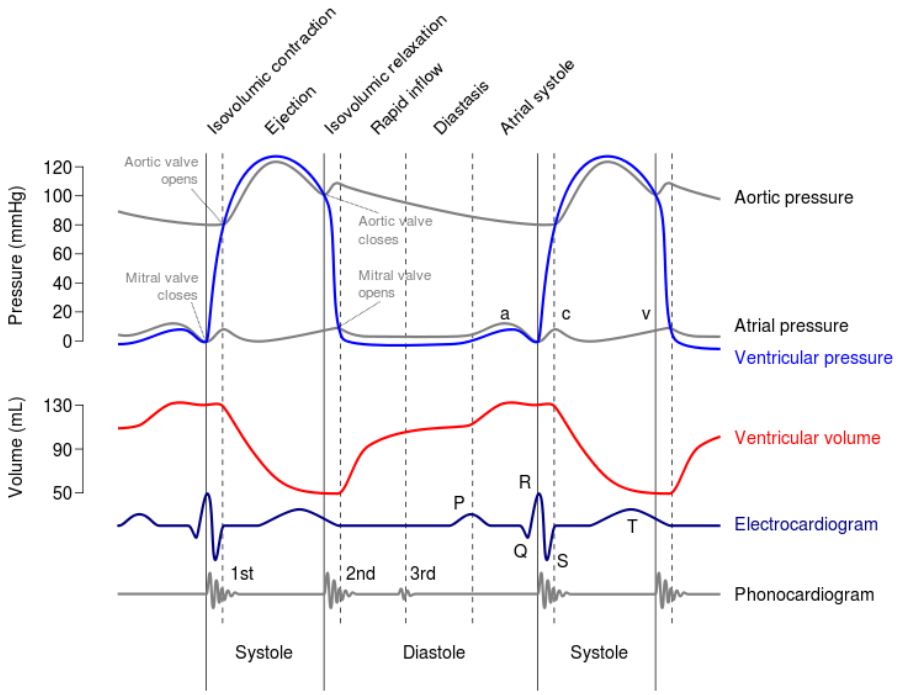

Figure 5: The Wiggers diagram [34] visualize the cardiac cycle by different measures. Along the x-axis is the time of the cycle, while the y-axis contains information on mechanical events such as pressure and volume changes, electrical events detected by echocardiography and sound events detected by the phonocardiogram.

2.3 Retrospective gating with Electrocardiogram triggers

ECG gating is a method for synchronizing data with the use of ECG trigger times. ECG is a time-varying signal representing the electrical potential that causes the muscles in the heart to contract and relax [35]. An ECG signal thus contains timing information of the cardiac cycle. The timing information, the trigger times, can be used as reference points between consecutive cycles when ECG signals and image acquisition are conducted synchronously.

ECG gating is also a proposed method for increasing the frame rate for ultrasound imaging. Current research uses a prospective gating method where a large imaging sector is divided into several sub-sectors as seen in Figure 6 and described in Section 1.3.1.

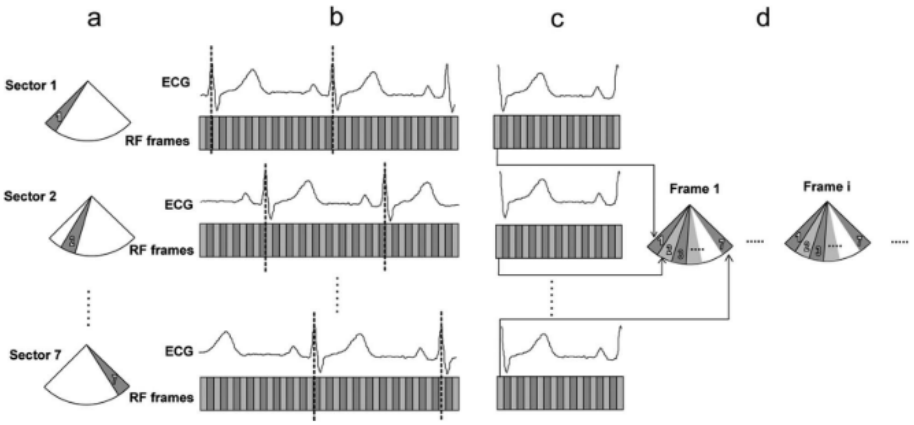

Figure 6: (a) Main sector is divided into 7 sub-sectors. (b) ECG and RF signals are measured for 7 consecutive cycles in a continuous sequence. (c) One cycle is extracted from both ECG and RF signals. (d) Frames from different sub-sectors are aligned for a full sector view [7].

Another gating method is the retrospective ECG gating which is not constrained by precise sub-sector stitching. Retrospective ECG gating records the whole imaging sector during several consecutive cycles and combines the image frames retrospectively by ECG trigger times into one cardiac cycle. Retrospective gating is visualized in Figure 7. The method is frequently used in both Computed Tomography (CT) and Magnetic Resonance (MR) imaging to increase the temporal resolution when imaging the heart [11] [36] [10].

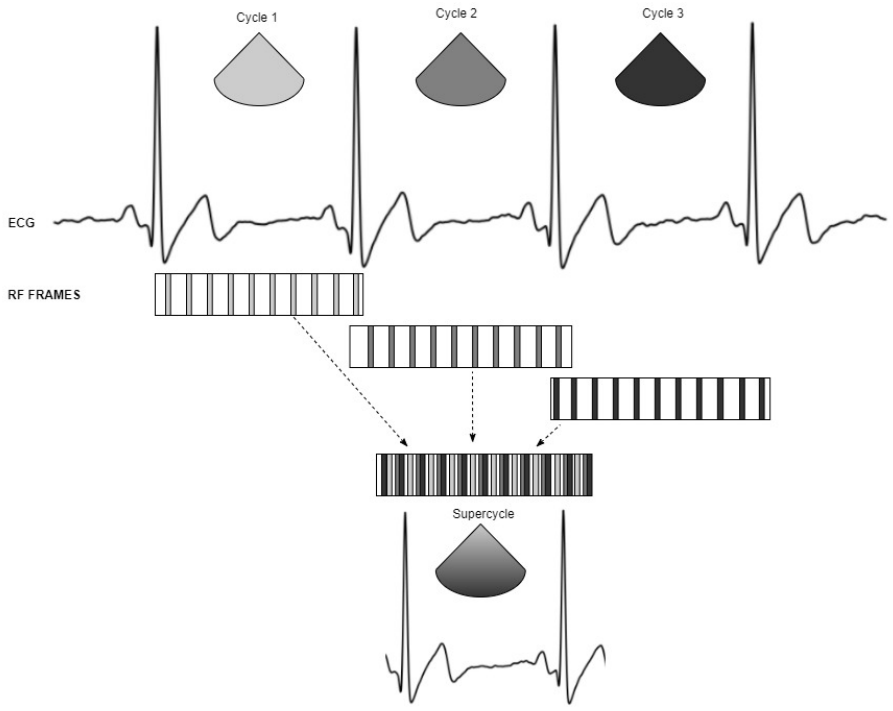

Figure 7: Proposed method of retrospective gating to create a Supercycle. The figure shows an example of three cycles combined to a Supercycle. When assuming that FR is not a multiple of HR will the samples from the three different cycles cover different parts of the Supercycle. The figure is adapted from the project thesis.

2.4 B-spline interpolation and data fitting

Interpolation and data fitting determine the image frames between known frames, and thus increase the number of frames per second. Interpolation is mathematically the estimation of a value of the function $f(x)$ based upon already known values of it, where $f(x)$ will pass through all the original data points. Data fitting is also an estimation of $f(x)$, but fits the curve of the original data points with a limited degree of freedom, as best as possible rather than restricting the estimation to pass through all original points.

If we at each time step, $t_0, t_1, ...t_n$ obtain an image frame $(x_0, z_0), (x_1, z_1), ...(x_n, z_n)$ we can determine the function $(x, z) = I(t)$ whose graph will estimate the image frames between the known times. The determination of this function is based on the chosen complexity. The nearest-neighbor interpolator and the linear interpolator are rather simple functions that respectively select the estimated point as its nearest value or as a point at the straight line between the two nearest points. Higher-order polynomials will increase the complexity of the estimated function for a more specific and weighted contribution of neighbors.

Splines are piecewise polynomials, that for interpolation pass through the $n+1$ points to fit the points as best as possible. When using splines for data fitting the piecewise polynomials might not pass through all $n+1$, but rather try to fit each spline as best as possible to the $n+1$ points. Such splines could be linear combinations of basis splines, called B-splines, where each B-spline is a polynomial of degree d.

B-splines are based on a non-decreasing sequence, $\mathbf{u} = (u_i)$ of knots partitioning the data points into $u-1$ intervals, i [37]. The $i'th$ B-spline for a spline degree of d and a knot vector $\mathbf{u}$ is defined by

$$B_{i,d,u}(x) = \frac{x - u_i}{u_{i+d} - u_i} B_{i,d-1,u}(x) + \frac{u_{i+1+d} - x}{u_{i+1+d} - u_{i+1}} B_{i+1,d-1,u}(x) \tag{2.10}$$

for all x, with

$$B_{i,0,u}(x) = \begin{cases} 1, & \text{if } u_i \leq x < u_{i+1} \\ 0, & \text{otherwise.} \end{cases} \tag{2.11}$$

A visualization of third order (cubic) B-splines is shown in Figure 8.

This method is the foundation of the framework *tensorspline*. Grønli, Wigen et al. [38], describe tensorspline as a solution to the challenge of model-based reconstruction and regularization in vector flow imaging. The framework has the advantage of utilizing several information sources for the interpolation, such as both noisy sensor data and the physical models of the system [38] [39].

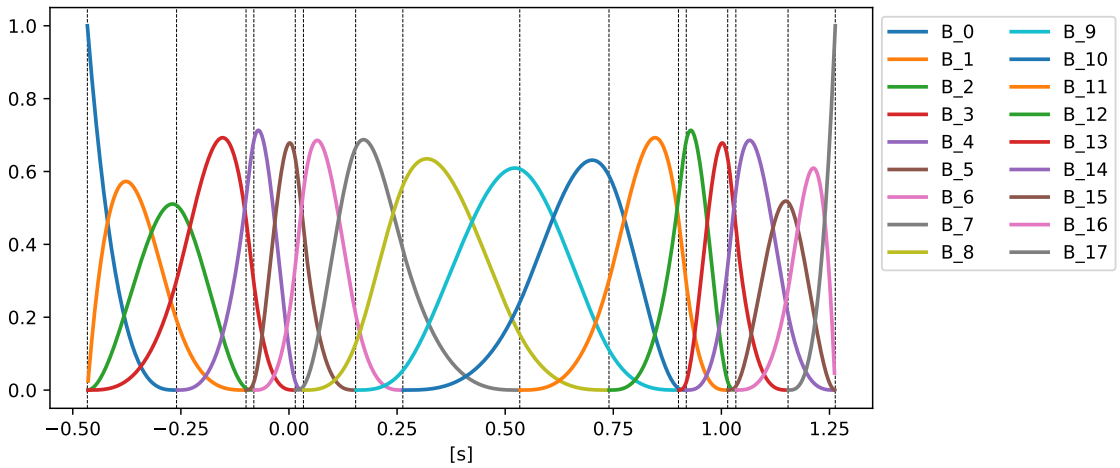

Figure 8: Cubic B-splines (d=3), defined for each data point. This shows a non-uniform B-spline basis as the u knots, marked as vertical lines, are placed non-uniformly in time (along the x-axis).

2.5 Pearson Correlation Coefficient

The Pearson Correlation Coefficient (PCC), r, is a measure of linear correlation between two sets of data points described in equation (2.12). PCC is invariant to linear scaling as the denominator adjusts the data points to have equal units and scale. This makes r a normalized measure with values between -1 and 1. The interval [-1,1] indicates whether the datasets have strong negative correlations, no correlations or strong positive correlations [40].

$$r = \frac{\sum(X_i - \bar{X})(Y_i - \bar{Y})}{[\sum(X_i - \bar{X})^2 \sum(Y_i - \bar{Y})^2]^{\frac{1}{2}}} = \frac{\sigma_{XY}}{\sigma_X \sigma_Y} \tag{2.12}$$

3 Methodology

The idea of the ultrasound supercycle is to sample data from consecutive cycles and combine these into one cycle, a *Supercycle (SC)*. The set of consecutive cycles to be combined, *the cycle basis*, consists of n cycles. They have to be *separated in time* as they are sampled sequentially in the original dataset. The separation process is described in Section 3.1. The cycle time vectors are further *normalized to a standard length*, described in Section 3.2, so the timing of the cycle phases is preserved. Lastly, a *spline interpolator* is used to get the combined cycles on a uniform time grid, which is described in Section 3.3. Also a proposed method of filtering outlier cycles for increased robustness is described in Section 3.4. The described pipeline is visualized in Figure 9.

The method utilizes the fact that new information of an overall cardiac cycle is gained when samples from the combined cycles occur at different times relative to a normalized cycle time. This idea is shown in Figure 10, for the reconstruction of a simple sinusoidal wave.

The frame rate of the resulting Supercycle is optimally increased by a factor of n compared to the sampling rate, when assuming that samples from the n cycles fall at different and perfectly equally spaced times relative to the normalized cycle time. The estimated resulting frame rate of the Supercycle is called the *target frame rate*. The increase in frame rate is without compromising the ultrasound setup or examination. The Supercycle has thus the potential of retrospectively increase the frame rate while keeping the spatial resolution by a combination and interpolation of n cycles. This retrospective method is shown in Figure 7. The case of which $n = 3$ is especially investigated as most old ultrasound recordings in practice normally have at least $n = 3$ cycles available and less time is needed for acquiring the recording making it easier for the patient to hold their breath.

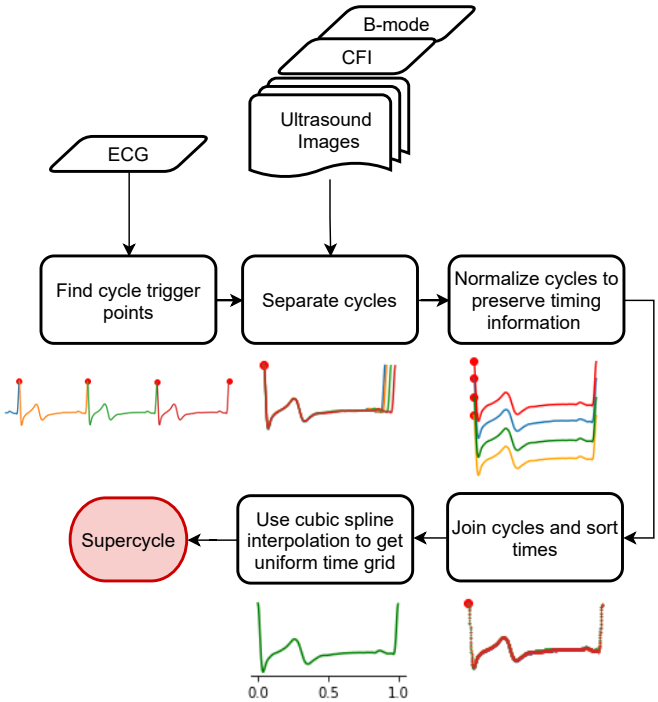

Figure 9: Pipeline of proposed method showing the main stages of the Supercycle after data fetching of ECG, B-mode and CFI.

In addition to creating the actual Supercycle, the relation between heart rate and the sampling rate is studied to get an idea of how to gain maximum information of the sampled cycles. This part is adapted from the project thesis. Also, a study of the translation between frames is performed, leading to an attempt of pre-processing the data to remove excessive translation described in Section 3.5 and 3.6.

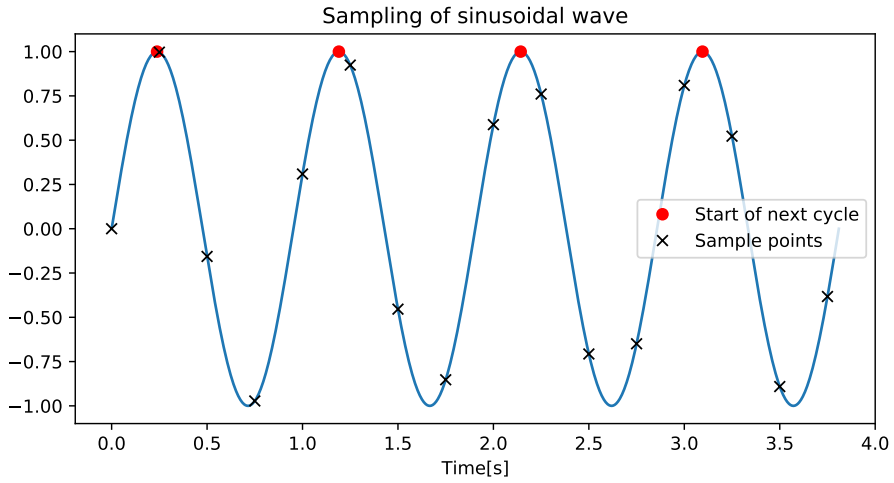

(a) Three consecutive cycles sampled at a constant frame rate equal to 4 Hz. The period of the wave is a simulation of a heart rate corresponding to $\frac{63}{60}$ Hz. (Figure from project thesis.)

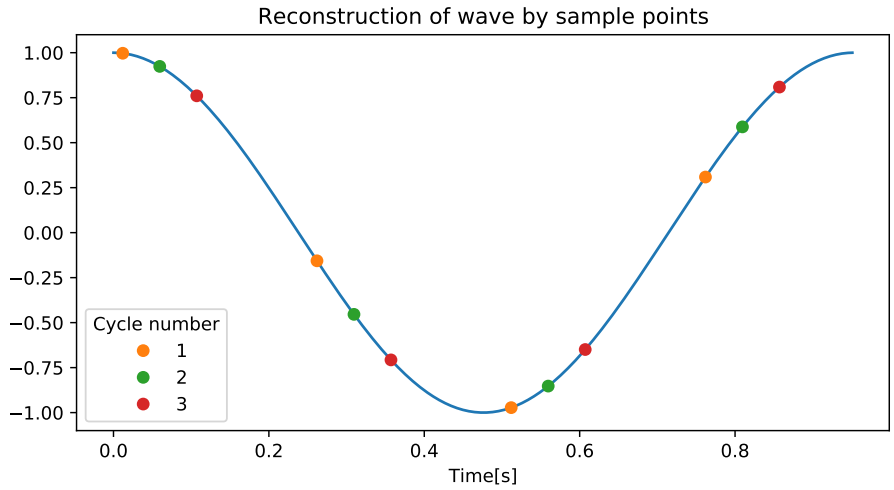

(b) Reconstructed sinusoidal wave from sampling of the three consecutive cycles shown in (a). (Figure from project thesis.)

Figure 10: A simple example of reconstruction of a periodic signal by combination of information from consecutive cycles.

3.1 Cycle Separation

The datasets in Appendix C are ultrasound imaging data of several sequentially recorded cardiac cycles. Timing information is needed to split the data into disjoined cycles. The point in time for the transition from one cycle to the next, the trigger time, is extracted by several methods.

In Figure 11 the green x's are trigger times from ECG, described in Section 2.3. An ECG recording contains times giving reference points for the beginnings of the contraction cycles, the edge of the R−peaks [41], see Figure 5. These reference points can be used as trigger times for splitting cycles. The trigger times are given as times from the ECG signal, a conversion to the corresponding nearest point in time for the ultrasound data must thusly be found.

The red x's in Figure 11 are trigger times from the machine learning (ML) package, described in Section 3.5. ML provides a list of trigger times for the end of systole (ES), based on measuring the size of the heart chamber as this varies through the cycle.

A third method of using the periodicity of the mean of pixel values in B-mode images is also investigated, shown as the blue x's in Figure 11. This method assumes that the mean of pixel values in each frame varies with the cycle period. Trigger times can be found by temporal localization of the periodically repeated features in the mean. The mean is computed for all pixels in a frame as this shows reasonable periodicity. The periodic features are localized in time by extremum points of the time series of the mean. The method requires at this point manual tuning for extremum localization. The mean of frame is calculated as followed

$$I_{mean}(t) = \frac{1}{N_x * N_z} \sum_{i=1}^{N_x} \sum_{j=1}^{N_z} I(t, i, j), \tag{3.1}$$

where N_x is the number of pixel values in x-direction, and N_z is the number of pixel values in the z-direction (often y-direction in an image frame in Cartesian coordinates, but z-direction in this ultrasound setup, as z equals depth). The difference of means, the error in equation (3.2), between ground truth and the supercycle was plotted over time to evaluate differences in performance during the cycle.

$$e(t) = I_{GT_{mean}}(t) - I_{SC_{mean}}(t) \tag{3.2}$$

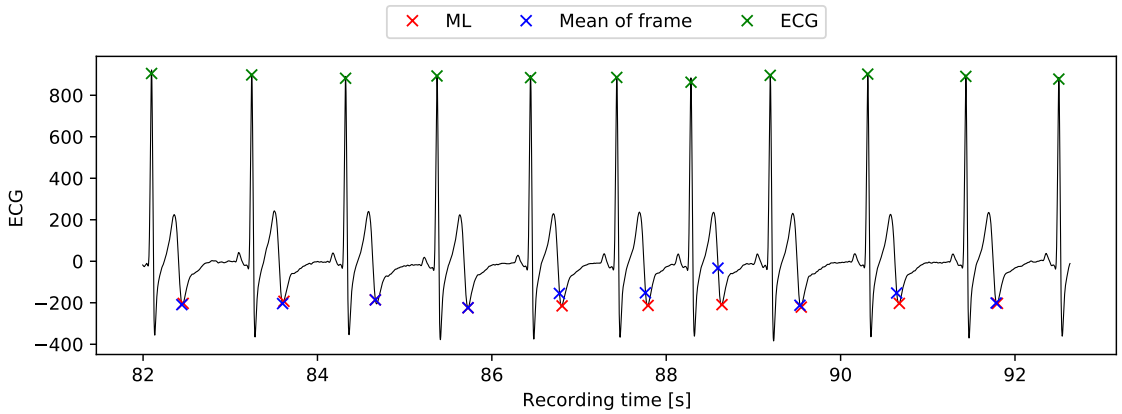

Figure 11: The 10 cycles in dataset A0 are plotted from the ECG signal. The colored x's mark the potential trigger times used for separating the continuious signal. Three methods are used for localizing such trigger times, here differentiated by different colors.

3.2 Normalization and Cycle concatenation

The cycles are extracted from the recordings based on trigger times such as R-triggers and ES triggers. These trigger times depend on the heart rate which is varying slightly over time. As consequences, the lengths and cardiac phases of the separated cycles are slightly varying from each other.

A normalization procedure is performed to preserve this temporal information before joining the cycles. A uniform normalization is performed when assuming that the cardiac temporal information is linearly varying with the cycle length. However, research shows that the variations appear mostly in the diastolic phase [42], a fact that corresponds well with inspection of the investigated datasets. In Figure 12 are the variations seen as the cycle lengths differ, marked with x's, but the phase of systole and early diastole still correspond well.

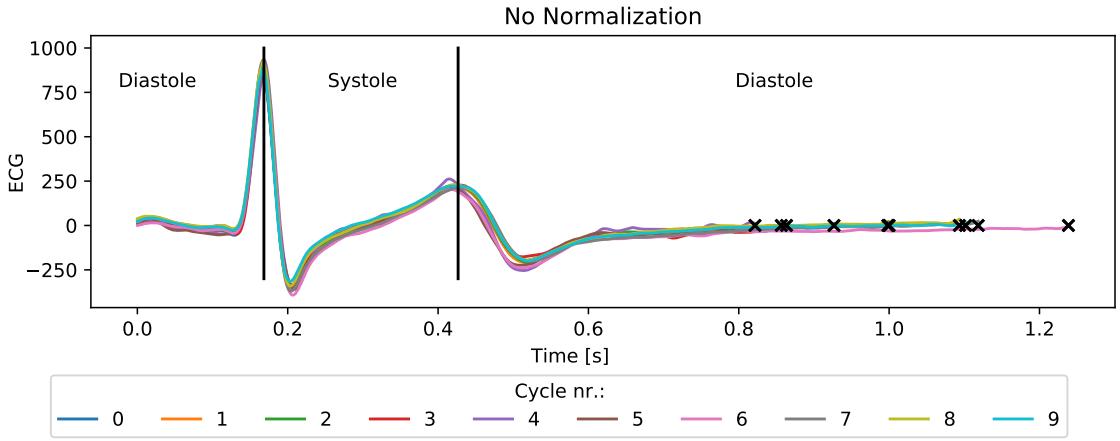

Figure 12: The 10 extracted ECG cycles from dataset A10 are plotted. The x's mark the cycle lengths. Dataset A10 has a cycle mean of 1.003 s and standard deviation of 0.129 s.

This forms the idea of normalizing only the diastolic phase. To split the cycles into systole and diastole a trigger time of the transition between systole and diastole, the end of systole (ES), is needed. ES is provided by the ML package. In addition, ES is calculated based on the HR, from equation (3.3) given by J.Pouget et al. [43]. J.Pouget et.al determined this relationship for male subjects with a sample standard deviation from regression equal to 0.014 s.

$$\mathrm{ES} = 0.546 - 0.0021 \cdot \mathrm{HR} \tag{3.3}$$

After normalizing the cycle times, the cycles are joined. The time vectors are firstly joined and sorted. Further are the ultrasound image samples joined and arranged based on the sorted order of the corresponding time vectors.

3.3 Remapping of time axis with B-splines

A non-uniform B-spline basis is used as a tool for remapping the time axis to a uniform grid as the sampling distribution after joining the cycles is not uniform. A B-spline of chosen order, o, is created for each pixel and a combination of weighted B-splines for each time step in the output axis is determined. Figure 13 shows an example of 16 data points, representing 16 sample times, in addition to 2 endpoints. For each data point is a cubic B-spline, $o = 3$, constructed as shown in Section 2.4, Figure 8. To fit the data points a weighted sum of these B-splines is calculated for each point in time by an optimization algorithm. This results in a continuous function, a fitted curve, as seen in Figure 13. The fitted curve is used to remap the data points to an arbitrary time grid. For Supercycle is the time grid a uniform parametrized (time) axis from 0.0-1.0, with the temporal resolution of the sum of data points provided by each of the combined cycles divided by the mean cycle length of the cycles. E.g. Supercycle consists of n=3 cycles. Cycle 1 is of length 0.9 s and has 14 sample times, Cycle 2 is of length 0.85 s and has 12 sample times, and Cycle 3 is of length 1.0 s and has 15 sample times. The temporal resolution of Supercycle is calculated as $\frac{sum(14,12,15)}{mean(0.9,0.85,1.0)} \approx 45$ Hz, denoted as the target frame rate.

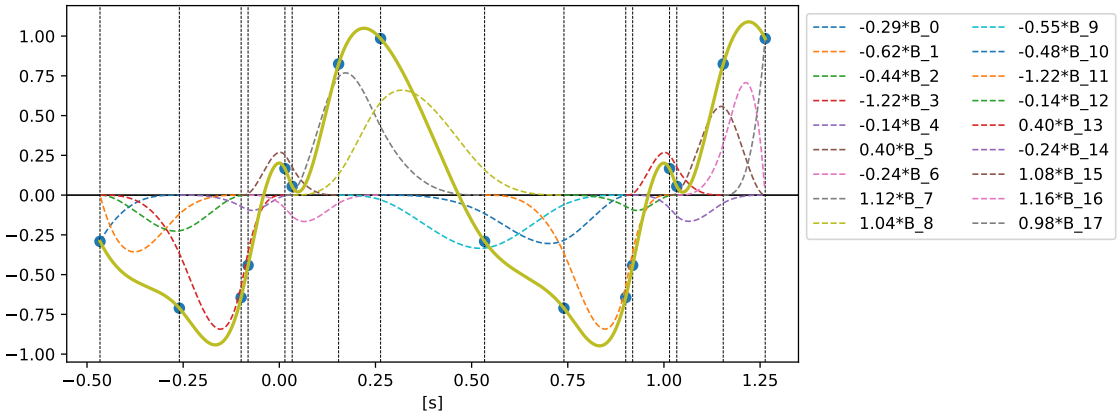

Figure 13: The green thick line is the resulting fitted curve. The label on the right lists the optimized weight of each B-spline, seen as the dotted colored lines. A similar curve is calculated for each pixel.

In some situations, the fitted curve contains spikes or sharp curves, as seen in Figure 14, giving unnatural effects in the resulting frames of the Supercycle. A regularization constraint is added to the optimization algorithm, limiting the curvature of the spline and introducing a smoothness effect. The weight of this constraint can be chosen by a smoothness factor, s. Figure 14-16 are constructed by three different smoothness factors $s = [1 \cdot 10^{-5}, 1 \cdot 10^{-4}, 1 \cdot 10^{-3}]$. For $s = 1 \cdot 10^{-5}$ the spikes are shown as in Figure 14, while for $s = 1 \cdot 10^{-4}$ they are less evident seen in 15. When the smoothness factor is chosen high, such as in Figure 16, for $s = 1 \cdot 10^{-3}$, the fitted curve no longer goes through all the data points.

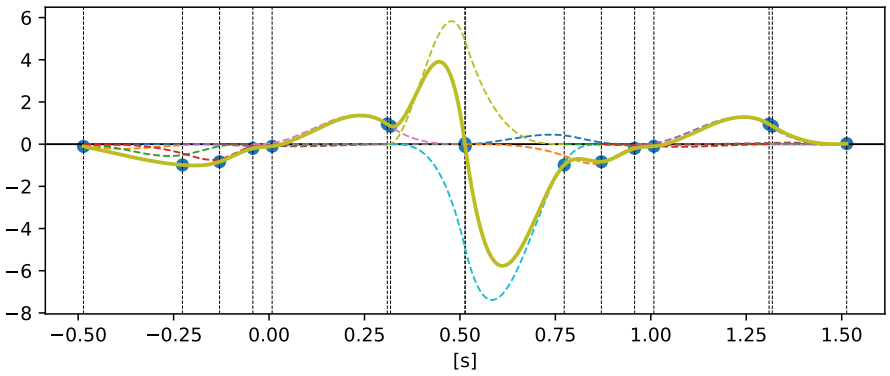

Figure 14: Cubic B-spline fitted curve with smoothness factor, $s = 1 \cdot 10^{-5}$

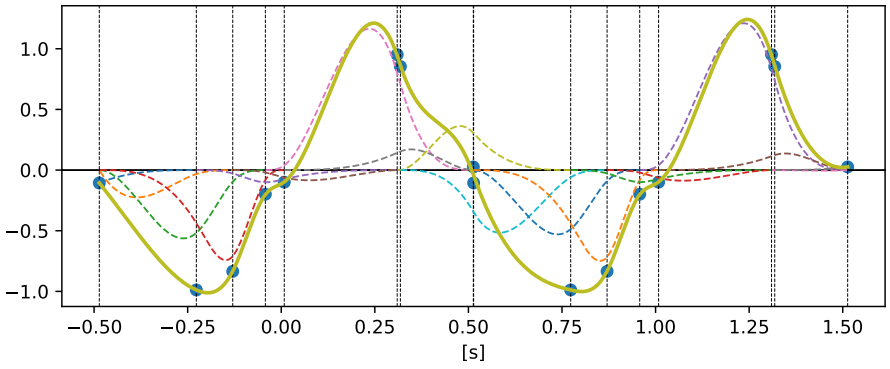

Figure 15: Cubic B-spline fitted curve with smoothness factor, $s = 1 \cdot 10^{-4}$

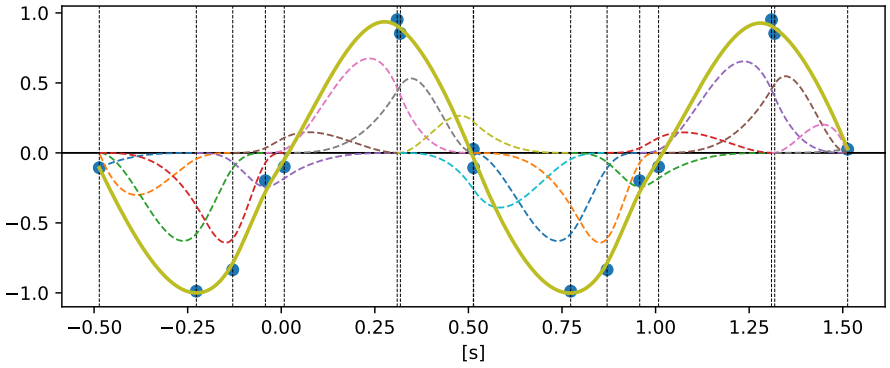

Figure 16: Cubic B-spline fitted curve with smoothness factor, $s = 1 \cdot 10^{-3}$

3.4 Outlier detection and correlation investigation for optimality in the cycle basis

The Supercycle is mainly constructed by the so far described methods, but an additional feature was however tested to increase performance and robustness. An outlier detector and similarity measurement technique are further described for choosing which cycles that should be joined for the Supercycle.

All available cycles should in theory be used for best utilizing the available information. However, some cycles vary more, both in cycle length and translation amount, and could potentially reduce the temporal and spatial resolution of the Supercycle. In practice is an optimal selection of the cycle basis desirable, to obtain maximum valid information about an overall cardiac cycle. For this to be fulfilled it is desirable to include as many cycles as possible, but exclude the outliers, those differing noticeably from the rest

The outlier cycles are detected by calculation of the *Z-score* of the position of key features at trigger times. The score is defined as

$$\text{Z-score} = \frac{\text{observation} - \mu}{\sigma}$$

where the observation is the mean of the pixel position (x, z), μ is the mean of all observations and σ is the standard deviation of all observations. A threshold for the Z-score is chosen to decide whether the observation is an outlier or not. A Z-score of zero indicates that the observation is identical to the mean. The Z-score is calculated for the three Base key features in all trigger time frames, and further compared to the threshold value. If one of the three features in a frame is over the threshold, the cycle is categorized as an outlier.

The size of the cycle basis, n can be chosen arbitrarily as long as it is less than the number of recorded cycles. For n less than the number of recorded cycles, the selection of cycles is firstly performed by filtering the outliers. Further is the selection based on finding the Pearson correlation coefficient between the normalized ECG signals for all remaining cycles, and choosing those with the highest correlation. The coefficient ensures that the n cycles have at least the most similar shape, of all recorded cycles, in terms of the ECG signal.

3.5 Field of view translation detection

In addition to the methodology for the construction of Supercycle is the data foundation investigated. The investigation is to gain information on how the surrounding situation of the ultrasound examination influences the data and the Supercycle. With this type of information at hand, methods to improve Supercycle's robustness can be performed. Which can further potentially increase Supercycle's applicability. As a medical ultrasound examination is conducted on humans, by humans, and over a period of time, the recordings might contain respiration artifacts and transducer movement. These movements cause small displacements in the FOV between frames. The displacement at a relatively equal time in the cardiac cycle will be noticeable after the concatenation of cycles as the movements proceed over time. The displacements will further propagate into the interpolation part of the Supercycle, making the basis of the interpolation improper. For satisfactory performance is it desirable to measure these translations between frames. The measures could ultimately detect unstable datasets, and further either discard them or correct them for the instabilities.

Multiple methods for detection of translation due to respiratory motion are presented in Section 2.1.5. These methods are, however, either invasive or limit the acquisition time. Detection of translation is in this thesis conducted by tracking the movement of key features in the image at trigger times. A machine learning package developed in the Department of Circulation and Medical Imaging at Norwegian University of Science and Technology is used to extract key features and timing information. The package provides easy use of ML algorithms for ultrasound image processing, with the use of tensorflow based Convolutional Neural Networks. Timing information is given as trigger points for the end of systole (ES), which will happen at an equal time relative to the cardiac cycle. There are five key features given by the ML package as can be seen in Figure 17. The positions of the key features are extracted for each ES trigger frame.

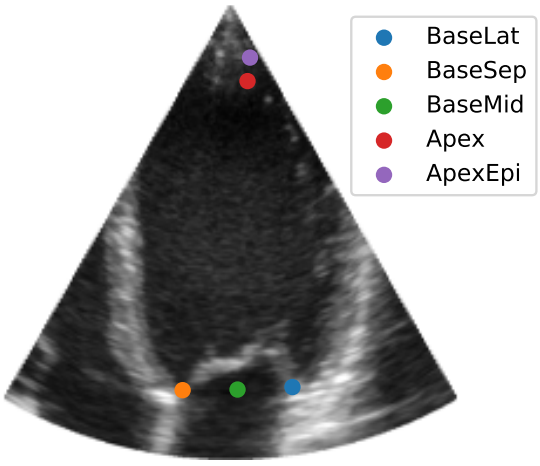

Figure 17: A 2D B-mode sector with it's key features marked. The Base features are mostly used. These features are provided by the ML package for ultrasound image processing.

The position displacement between ES trigger times, which describes the translation, is investigated through simple pixel displacement and variance measurements in lateral and axial direction respectively. In addition is the Euclidean distance used for displacement detection independent of direction. These metrics form the basis of the translation investigation for each dataset.

3.6 Rigid Co-Registrated transformations

Co-registration for the transformation of frames to increase their alignment is a proposed method for increasing the robustness and performance of the Supercycle. The co-registration is based on the key features BaseSep, BaseLat and BaseMid found at specific trigger times. The trigger times are either extracted as R-peaks from the ECG signal or as ED and ES times from the ML package.

The 2D view of the ultrasound recordings are originally given in beamspace, which is represented as a grid of the distance, r and angle, θ. A conversion is needed to obtain the characteristic 2D sector as seen in Figure 18. The sector is the image representing the true distances in practice, giving the lateral direction, the width as x, and axial direction, the depth as z.

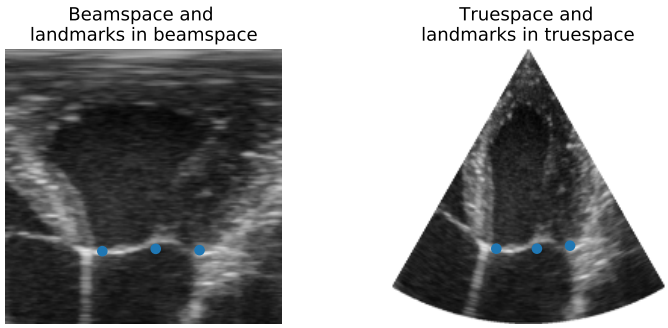

Figure 18: Cardiac ultrasound in the beamspace (r, θ) and the truespace (x, z) representation.

The co-registration utilizes the Base key features, found in truespace, as tie points. Since a small area around the apex in truespace maps to a big area in beamspace, small variations in Apex and ApexEpi are thus mapped to a big region in beamspace. Apex and ApexEpi are thus less trustworthy tie points for the rigid co-registration and the reason why only the Base key features are used.

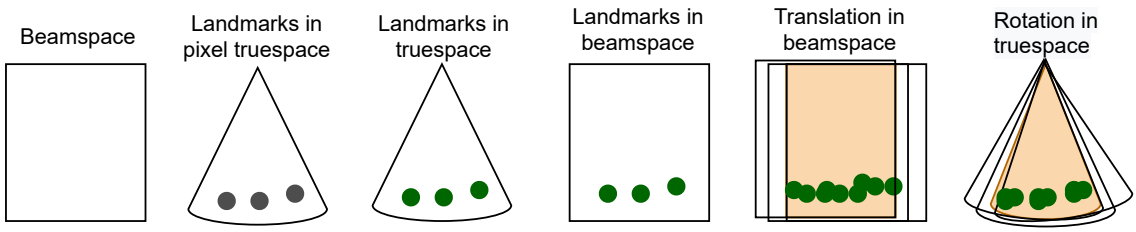

Figure 19: The conversion between beamspace and truespace for the rigid co-registration. The size of the resulting frames are given as the minimum common beam grid marked by the shaded area in the two last representations.

The rigid transformation is calculated by finding the mean translation in all Base key features, between all trigger frames and trigger frame zero. Each trigger frame has now a transformation matrix that transforms its frame to match the base key features of the first trigger frame. It is used a linear interpolation of these transformation matrices to determine the transformation matrices for all intermediate frames. Lastly, is the dataset transformed with these matrices. The linear transformation is performed in beamspace which translates to a simple rotation around apex in truespace, giving translation in both depth and width in the transformed sector, seen in Figure 19.

3.7 Analysis and validation

3.7.1 Qualitative analysis

As Supercycle intends to increase temporal resolution while preserving the spatial resolution the evaluation methods for qualitative analysis has been mainly human investigation of video streams. Additionally, M-mode imaging can be utilized for extracting a dense visualization of the video stream while still preserving the information about the temporal resolution. Evaluation is also conducted by visual comparison of images at the same relative times during a cardiac cycle, i.e. trigger times extracted from ECG or the ML package.

3.7.2 Quantitative validation

Quantitative measures are desirable as some metrics give information challenging to perceive by the human visual system while others effectively capture the same information as human inspection and can be used for automatic decision making. Discovering and quantizing image information is a whole topic itself. Metrics that capture findings have been investigated throughout the thesis. Mutual Information (MI), Dynamic Time Warping, the Structural Similarity Index (SSIM) and the Feature Similarity Index (FSIM) [44] showed potential in quantizing cycle similarity. A small research of MI, SSIM, FSIM and Pearson Correlation was performed by comparing different M-mode images to an M-mode reference image. The research was based on checking whether the similarity metrics corresponded with human perception of the similarity between an image and the reference, a validity check. The results from the research showed FSIM to most often agree with human perception, however, are most of these procedures often shown to be unreliable and haven't been used throughout the thesis.

Pearson correlation is however good for ECG cycle similarity. In addition to Pearson Correlation are mean and standard deviation, together with max euclidean distance used.

3.8 Data foundation

The in-vivo datasets used are obtained by a GE M5Sc phased array probe with a frequency bandwidth of 1.5-4.5 MHz and aperture dimensions 17 x 28 mm. The transmitted focal point is at depth 30 cm with a varying FOV. The B-mode datasets consist of a grid of elements each containing the brightness value at their respective positions. These brightness values correspond to the reflection of scatterers at the specific point in space. The CFI data is obtained with a pulse repetition frequency (PRF) of ∼3.5 kHz and is composed of a grid of R1 values, where R1 is a complex value of the mean angular frequency found by the autocorrelation estimator given in equation (2.7). Both imaging modalities are shown in Figure 3.

There are in total 46 datasets obtained from three different patients A, B, and C. Dataset B and C were also used for the project thesis. The datasets vary in frame rate from 6-149 Hz for B-mode and 9-34 Hz for CFI, and contains between 10-12 cardiac cycles each. In addition are the datasets from patient A (Data A) recorded in four different patient situations. These are: *Breathing normally*, *No breathing*, *Breathing heavily*, and *High pulse after activity*. Detailed information of the actual datasets represented in this report can be found in Table C.1 in Appendix C.

4 Results

The result section consists of five parts, beginning with a comparison between state-of-the-art methods for increased frame rate and the proposed method of the Supercycle. The second part shows the performance of the different choices for cycle separation, normalization type, and B-spline settings. Examples of Supercycle deployed on triplane imaging for B-mode and CFI are presented in the third part. The fourth part comprises methods for artifact reduction and improved data foundation, while the last part presents investigations on the correlation between heart rate and frame rate.

A default setup viewed in Table 4.1 is further chosen for the construction of Supercycle. These settings are used in the results to follow, if not stated otherwise. They are determined based on the results of the second result part. A Supercycle-object is further implemented in Python. The initialization of the object's tunable parameters are shown in Appendix A. An application of the Supercycle is further shown for B-mode and CFI and different parameters in Appendix B.

	Default Supercycle Settings
Number of cycles, n	10
Split method	R-peaks from ECG
Normalization method	Normalizing non-scaled diastole with ES trigger from equation (3.3)
B-spline order	Cubic (o = 3)
Smoothness factor	B-mode: $s = 1 \cdot 10^{-5}$ CFI: $s = 1 \cdot 10^{-4}$
Additional info	When n is chosen <10 the outlier detection and Pearson similarity check choose an optimal cycle basis. No transformation is used on any datasets.

Table 4.1: The default settings of the Supercycle framework. The settings are used for the results of Supercycle, if not specified otherwise.

Note that the given frame rates for the Supercycle, is as mentioned the *target* frame rate and is differing from the *optimal* frame rate as it is determined from not uniformly distributed sample times. This means that the *true* Supercycle frame rate has non-uniformly variations in temporal resolution over the normalized cycle time. As the concatenated cycles vary in length and are normalized between 0.0-1.0 the target frame rate of Supercycle is a scaled version of the optimal divided by the mean cycle length of the concatenated cycles. The target frame rates through the results are thus estimations of the true temporal resolution of Supercycle. With the standard deviation of the cycle lengths before normalization being at maximum for dataset A5 with standard deviation of 0.138 s, the estimates are however good predictions of the actual frame rates.

4.1 Supercycle's performance compared to a Single cycle

Figure 20 and Figure 21 show M-mode images from B-mode and CFI for state-of-the-art and Supercycle. The state-of-the-art is shown in the two first plots where a single cycle is firstly remapped to a uniform axis and secondly, a single cycle linearly upscaled to the same frame rate as for a Supercycle with $n = 10$. The third and fourth plot are constructed Supercycles with respectively $n = 3$ and $n = 10$ cycles.

4.1.1 B-mode comparison

The M-mode shows that even in the case of only $n = 3$ the movement of the valve is more defined through a bigger part of the overall cycle. Especially between 0.3 to 0.5, where the opening and closure of the valve happens, is the movement denser and with increased precision. For even higher $n = 10$ is the target frame rate increased from 64 Hz to 648 Hz. The valve movement is still more precise and denser than the single cycle case, and even for single cycle linearly interpolated to the same target frame, 648 Hz, an information increase is evident for $n = 10$. Especially around $t = 0.4$ is the movement smoother and contains less dense flickers in the $n = 10$ case compared to the single cycle and $n = 3$ cycle case. However, $n = 3$ case shows brighter valve movement over the whole normalized cycle time.

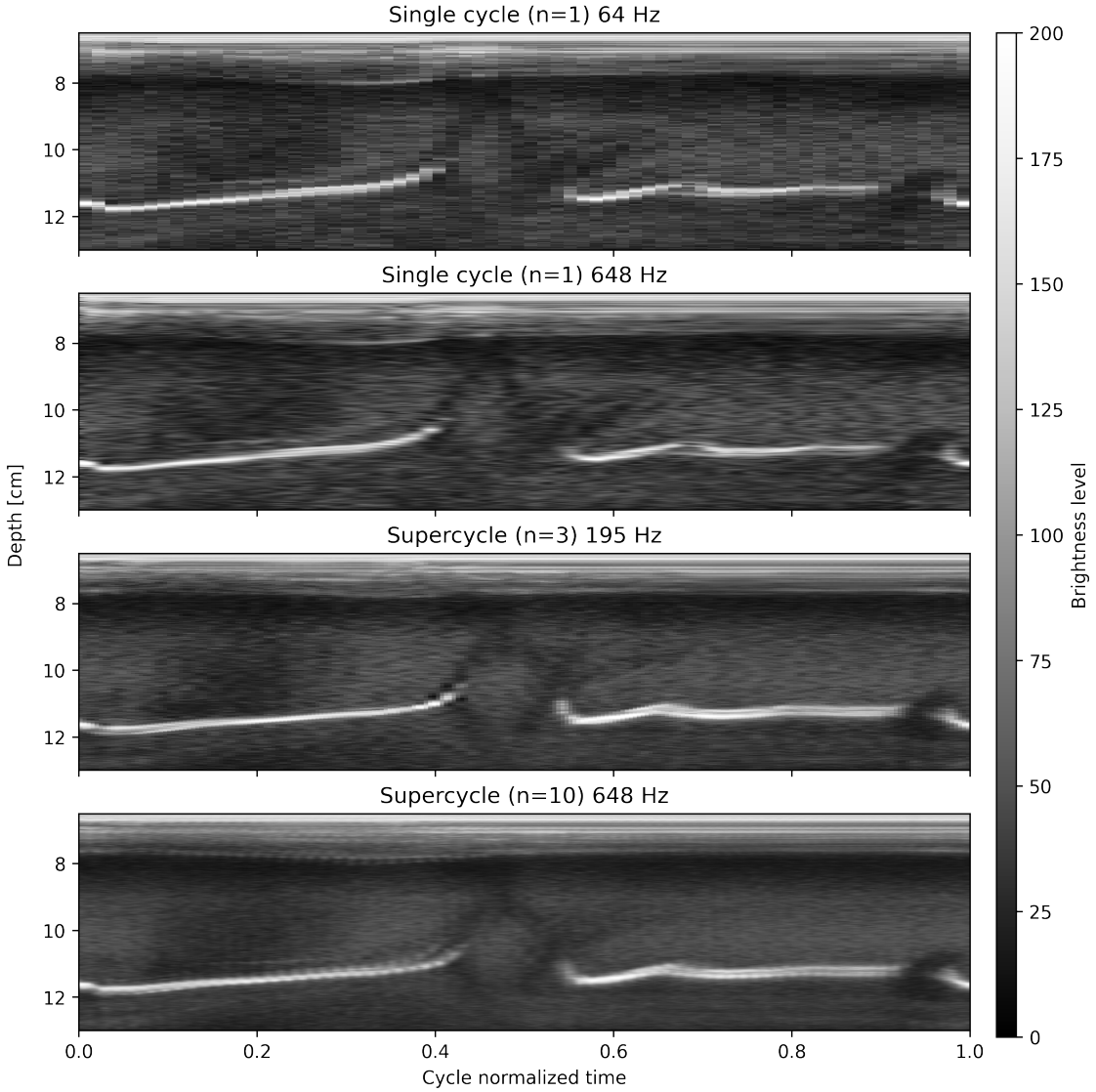

Figure 20: M-mode comparison of one single cycle and Supercycle for different settings from dataset A1. Note that the second plot, $Singlecycle(n = 1)$ 648 Hz is composed of only a single cycle but linearly interpolated to the scale of the Supercycle for $n = 10$ for further comparison of the two methods.

4.1.2 CFI comparison

The results from Supercycle performed on CFI also show potential for increased frame rate. In Figure 21 the improvements from going from a single cycle to a Supercycle with $n = 3$ cycles and further to a Supercycle with $n = 10$ cycles are apparent. The single cycle is sparse and without continuity, and for the upscaled single cycle are unwanted artifacts due to lack of information especially evident. Already with a Supercycle of $n = 3$ a lot more details are shown. Going from $n = 3$ to $n = 10$ shows even smoother transitions and overall better continuity now with a target frame rate of 265 Hz.

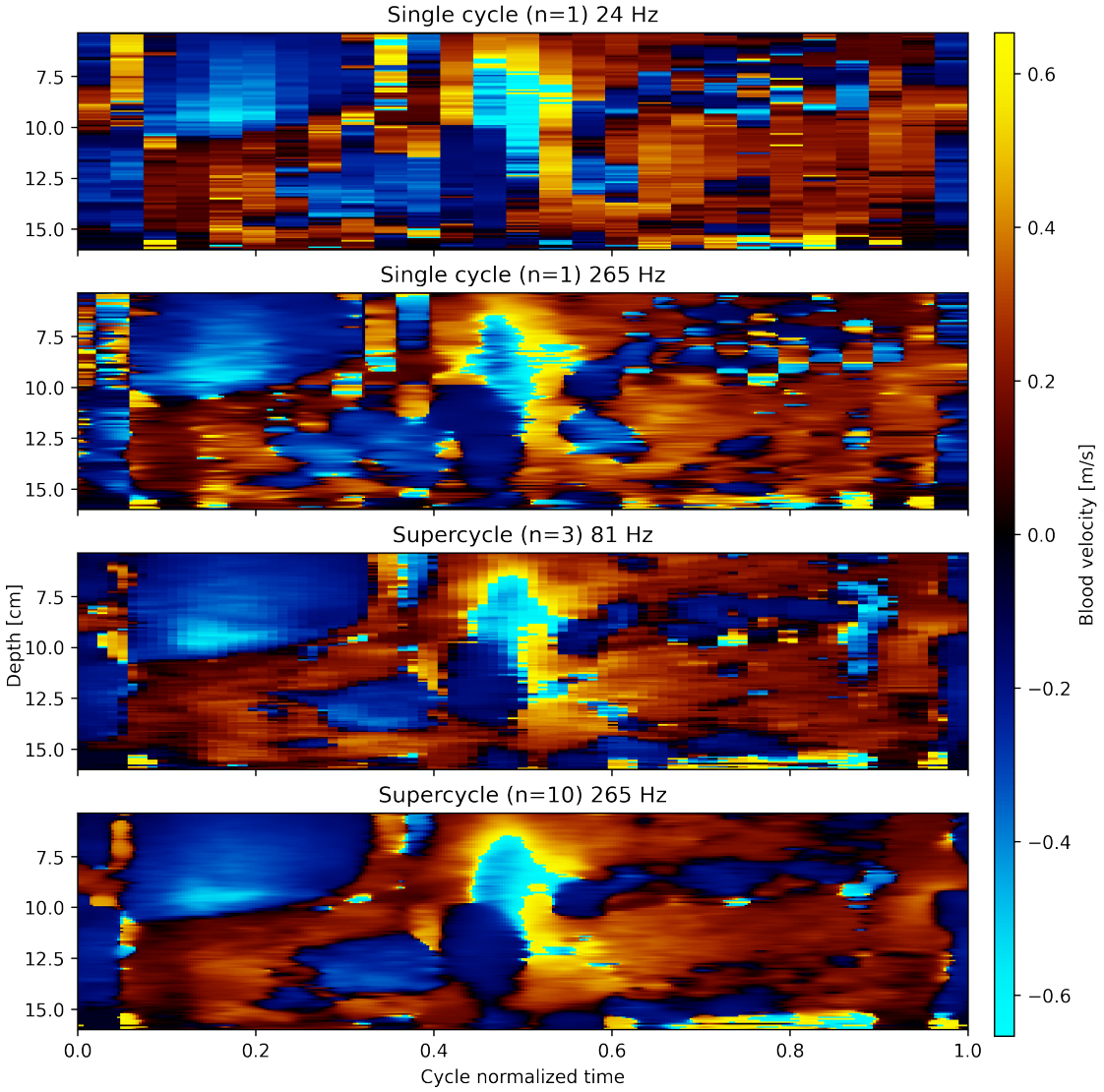

Figure 21: M-mode comparison of one single cycle and Supercycle for different settings from dataset A4. Note that the second plot, *Singlecycle*$(n = 1)$ 265 Hz is composed of only a single cycle but linearly interpolated to the scale of the Supercycle for $n = 10$.

4.2 Results of the Supercycle framework

4.2.1 Separation of cycles by different trigger times

A robust and precise splitting method is needed to join several, originally sequentual, cycles. Three methods for separating cycles are investigated on datasets recorded in different situations, to uncover their potential of precision and robustness. Split method 1 uses R-peak triggers from ECG, split method 2 uses ES triggers from machine learning, and split method 3 utilizes the mean brightness value over each frame during a cycle to localize periodic peaks used as trigger times. The methods are further described in Section 3.1.

Split method 1: R-peak triggers from ECG
The results of the three methods for separating cycles are seen in the Figures 22-28. Split method 1 shows overall robustness in finding periodic trigger values, also in challenging situations where the patient breaths heavily or has a high pulse as seen in Figure 22 and Figure 23.

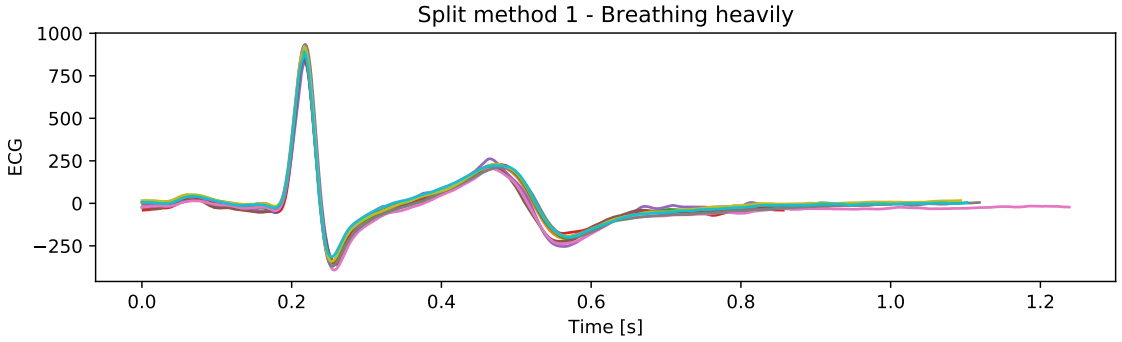

Figure 22: Dataset A10 for *Situation III: Breathing heavily* separated with R-peak triggers provided with the ECG signal.

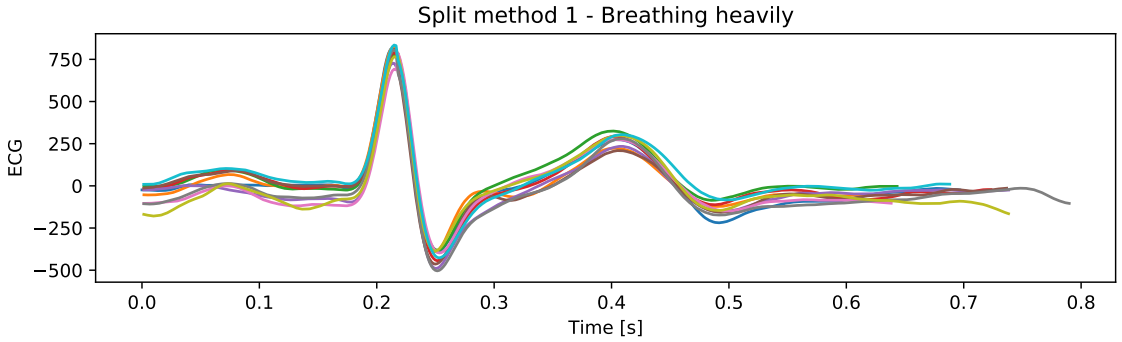

Figure 23: Dataset A17 for *Situation IV: Breathing with high pulse* separated with R-peak triggers provided with the ECG signal..

Split method 2: ES triggers from ML

Split method 2 works well for datasets with consistency in FOV, as ML finds ES based on the image of the heart ventricles seen in Figure 24 and Figure 25. In the situation of a high pulse is more spread in ECG values again evident, as seen in the results from split method 1. For the situation of heavy breathing is the method less precise as seen in Figure 26. Split method 2 miss separating one to three cycles which are expected as some frames during heavy breathing are totally out of the FOV. This makes it difficult to utilize B-mode information for the cycle separation.

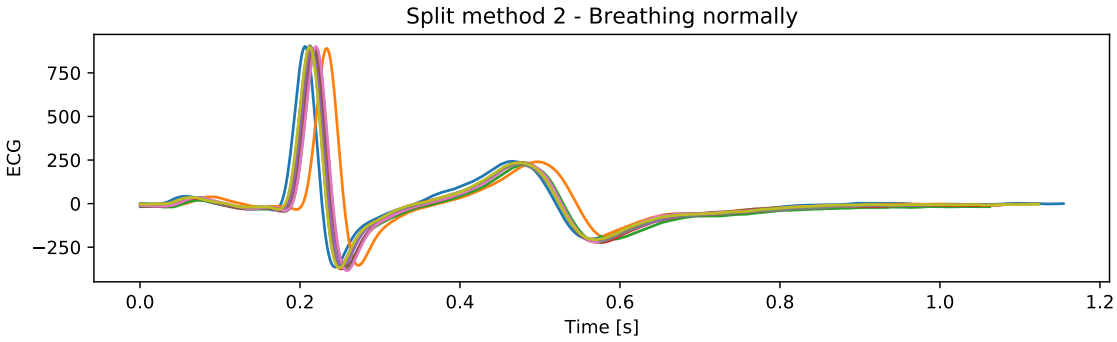

Figure 24: Dataset A0 for *Situation I: Breathing normally* separated with ES triggers provided by the ML package.

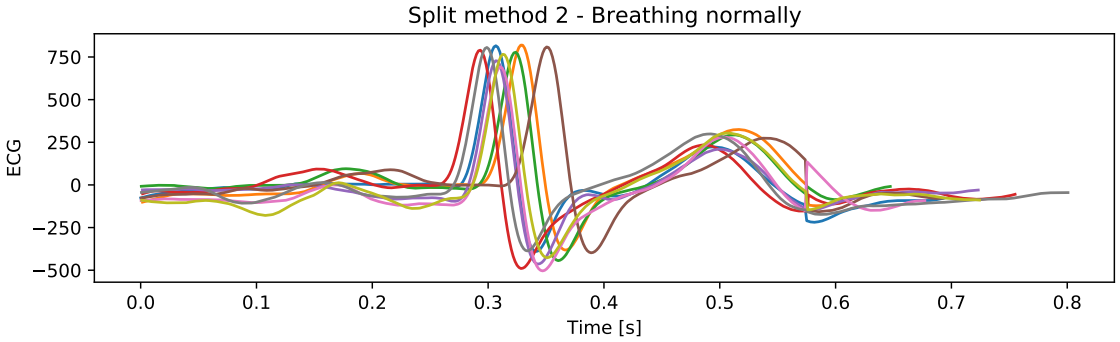

Figure 25: Dataset A17 for *Situation VI: Breathing with high pulse* separated with ES triggers provided by the ML package.

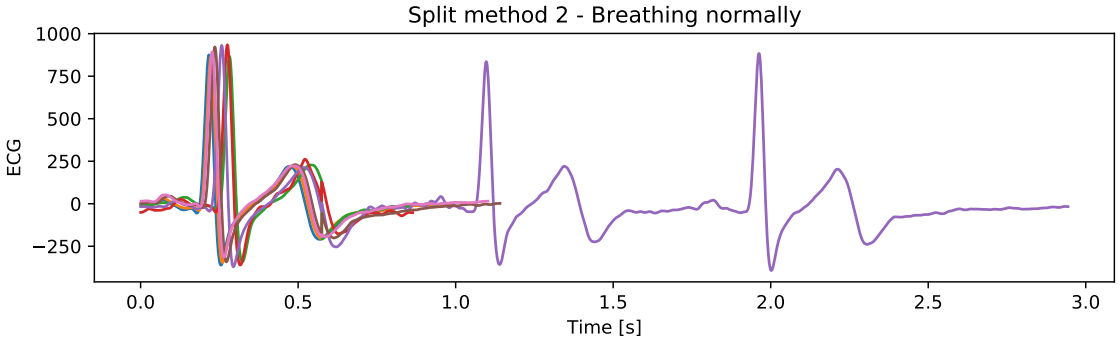

Figure 26: Dataset A10 for *Situation III: Breathing heavily* separated with ES triggers provided by the ML package.

Split method 3: Periodic triggers from the mean of frame

Split method 3 shows potential with the results in Figure 27. However, the method has increased variation between cycles as a result of missing trigger times when missing distinct periodic information in B-mode frames. Split method 3 is sensitive to translation in view and spread in ECG values giving unsatisfactory results of separation of cycles as seen in Figure 28.

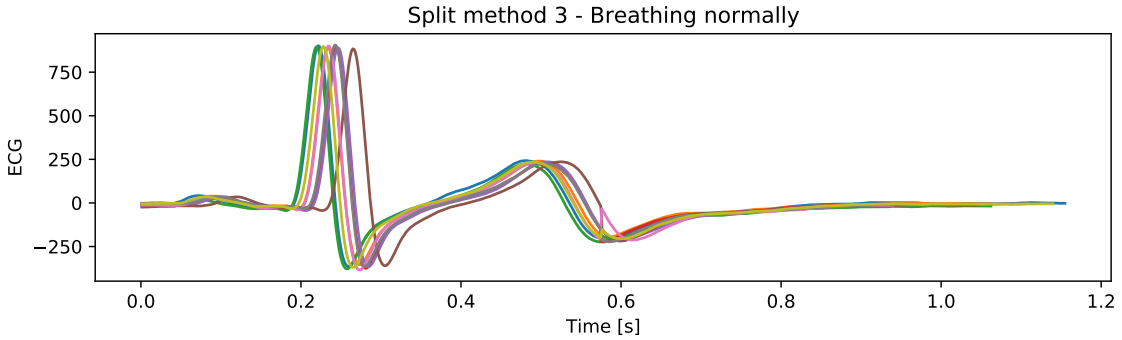

Figure 27: Dataset A0 for *Situation I: Breathing normally* separated with triggers provided with calculations of the mean of frame.

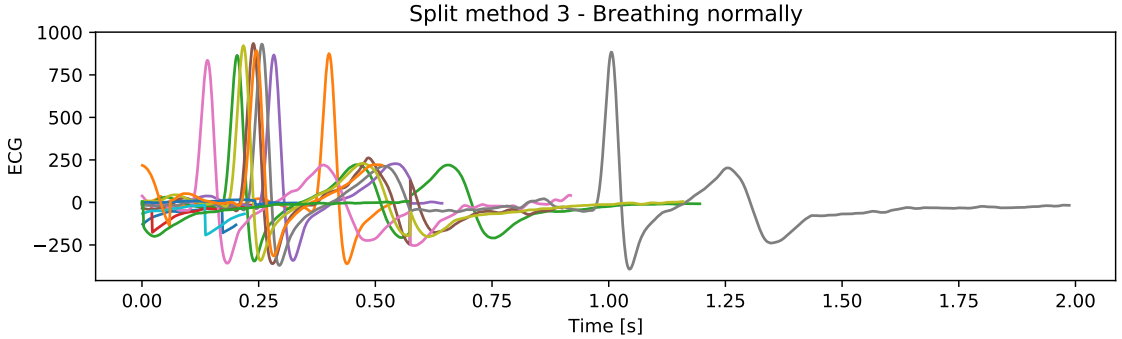

Figure 28: Dataset A10 for *Situation III: Breathing heavily* separated with triggers provided with calculations of the mean of frame.

4.2.2 Cycle normalization for preserving timing information

The comparison of normalization methods for the cycles in dataset A10 is seen in Figure 29. In the first plot are the cycles not normalized, seen by the differences in their lengths marked with an *"x"*. For the second plot are the cycles fully normalized between 0.0-1.0. The third and fourth plots normalize only the diastole. The trigger time for the transition between systole and diastole is the end of systole (ES) and is found by two methods. The first ES, *(*calculated trigger), is calculated based on the heart rate from equation (3.3) and the second ES, *trigger from ML*, is provided by the machine learning package. Both methods determine the ES triggers to be in the interval of 0.3-0.4.

The Pearson correlation coefficient is calculated between all combinations of pairs of cycles within a dataset as shown in Figure 31, as a study of quantitatively investigate the normalization methods. The mean of the coefficient for each pair is found for the four methods *No normalization*, *Normalizing whole cycle*, *Normalizing diastole*, and *Normalizing scaled/late diastole* and for all datasets (in Data A).

The first plot in Figure 29 shows that the cycles are fairly similar in the phase of systole and partly diastole, an interval of approximately 0.2-0.6. However, the lengths of diastole vary. After normalizing all full cycles between 0.0-1.0 a stretch in the interval 0.2-0.6 is visible. The cycles are no longer similar in this interval, and by joining these cycles will the Supercycle contain discrepancies in the timing of phases and no longer preserve the timing model of a cardiac cycle.

The third and fourth plots in Figure 29 normalize only the diastole, motivated by the prior results in plots one and two. Both diastole normalization methods show improved performance preserving phase information. Some irregularities are seen for both in early diastole, around $t = 0.5$, motivating the idea of scaling the ES trigger to only normalize late diastole. The performance after scaling the ES trigger by a factor of 1.8 is seen in Figure 30. The scaling factor was chosen to be later in the diastolic phase, where 1.8 gave triggers between 0.5-0.75. These results show an even higher similarity in the early phase of diastole.

The settings for normalization were further investigated by the Pearson correlation coefficients plotted in Figure 31. As expected are the correlation coefficients for *No normalization* and *Normalizing whole cycle* lowest. However, *Normalizing diastole* is performing better than *Normalizing scaled diastole* even though Figure 30 show the opposite. Notice also the datasets with very low correlation, below 0.80 for the *No normalization* case. These datasets are mostly for the examination *Sitation III: Breathing heavily*, showing that the variation in ECG cycles is increased for heavy breathing.

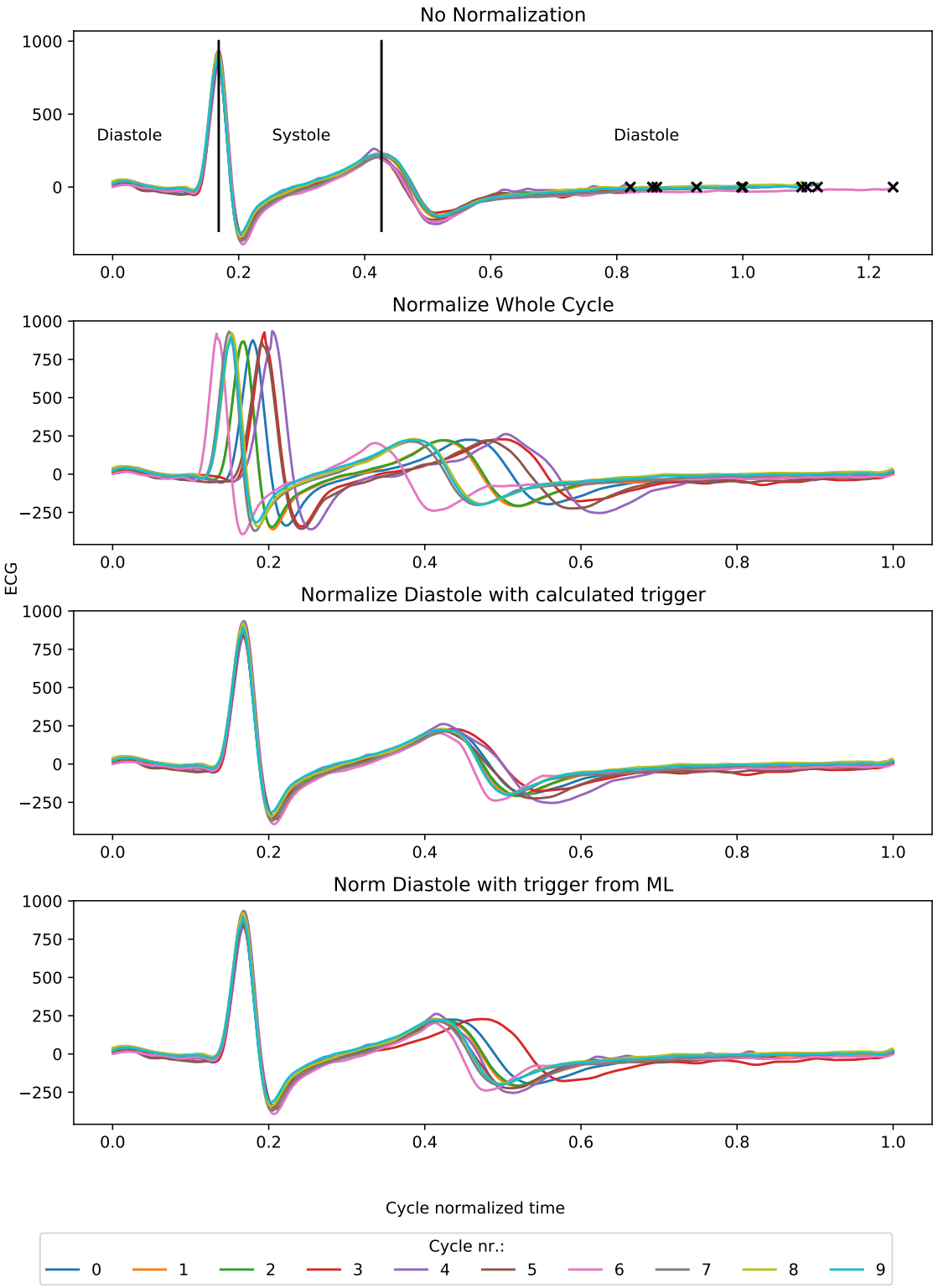

Figure 29: ECG cycles for dataset A10 are plotted by four normalization methods. For the first plot are the phases *Systole* and *Diastole* marked by two vertical lines, in addition to the marking of the end of each cycle with an *"x"*. The normalization of diastole shows improved performance over no normalization and normalization of the whole cycle. The normalization of diastole is performed with ES trigger calculated by equation (3.3) and ES trigger found by the machine learning package.

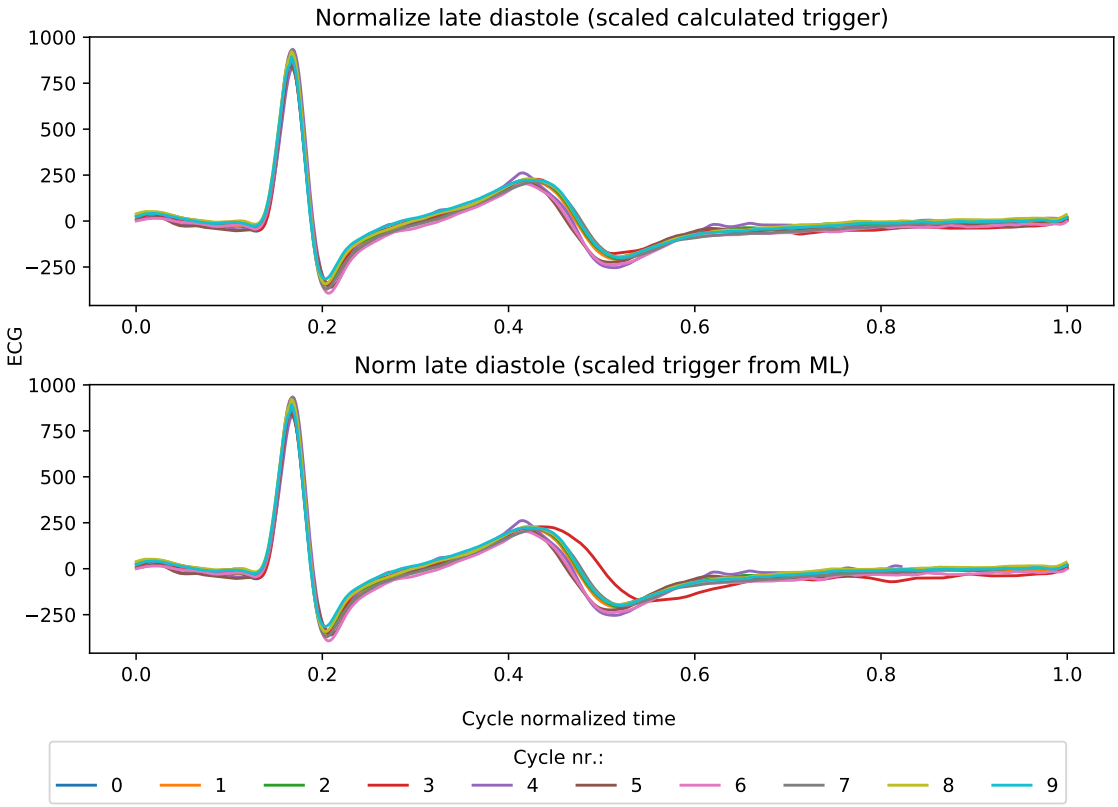

Figure 30: ECG cycles for dataset A10. By scaling ES with 1.8 the normalization showed even better results for both ES trigger extraction methods, as they appear more similar throughout the cycle period.

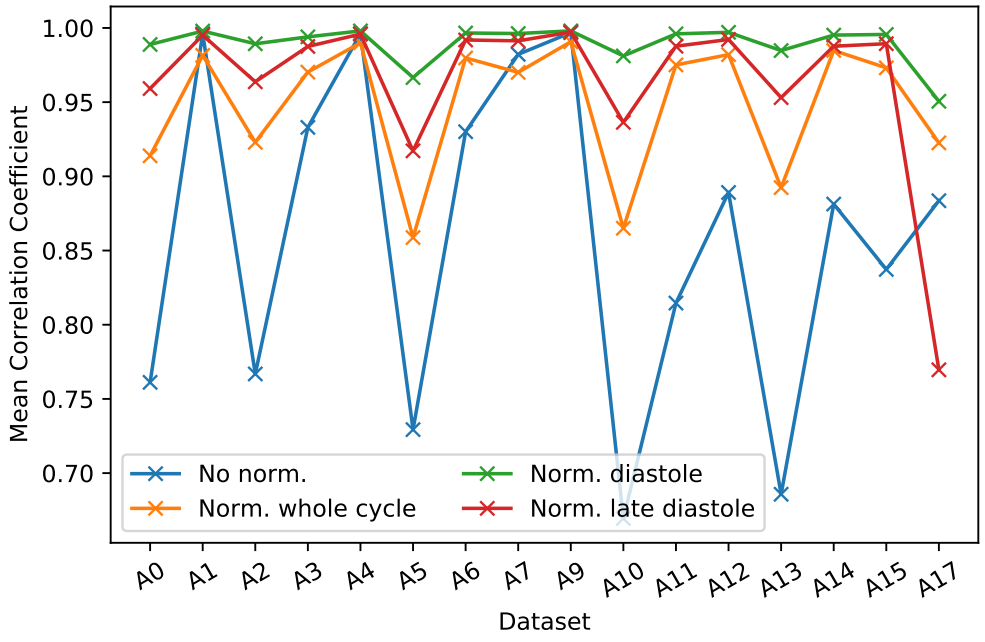

Figure 31: The mean of Pearson Correlation Coefficient calculated between all pairs of cycles. Here showed for all datasets (in Data A). Even if visual inspection of the ECG cycles in Figure 30 shows the scaled diastole normalization (late diastole) as the best, the Pearson coefficients show higher correlation for a normalization of the whole diastolic phase.

4.2.3 Settings of spline interpolator for creating a uniform time grid

The influence of different interpolation orders and smoothness factors are visualized by M-mode images seen in the Figures 32 - 36. The interpolation order is tested for $o = [0, 1, 3]$, corresponding to nearest neighbor interpolation, linear interpolation and cubic interpolation. The smoothness factor is tested for $s = [1 \cdot 10^{-4}, 1 \cdot 10^{-5}, 1 \cdot 10^{-6}]$ for B-mode images and for $s = [1 \cdot 10^{-3}, 1 \cdot 10^{-4}, 1 \cdot 10^{-5}]$ for CFI images.

The influence of the interpolator order

The smoothness factor is kept constant in Figure 32, visualizing the influence of three different B-spline orders. Small differences are seen when going from nearest neighbor fitting, $o = 0$, to linear fitting, $o = 1$, when creating a Supercycle from $n = 10$ cycles. However, around valve opening around $t = 0.4$, the linear interpolated Supercycle shows a bit higher precision even though the nearest neighbor interpolated Supercycle looks brighter. The results of the cubic B-spline Supercycle attract attention as the flickering artifacts are reduced giving a smoother valve movement. Similar results are seen for the M-mode acquisition for CFI in Figure 33. For cubic B-splines, is the CFI continuous and without unnaturally flickers over time. Both imaging modalities show the most natural movement in the case of cubic B-splines, setting this as the default order for the remapping procedure in the Supercycle.

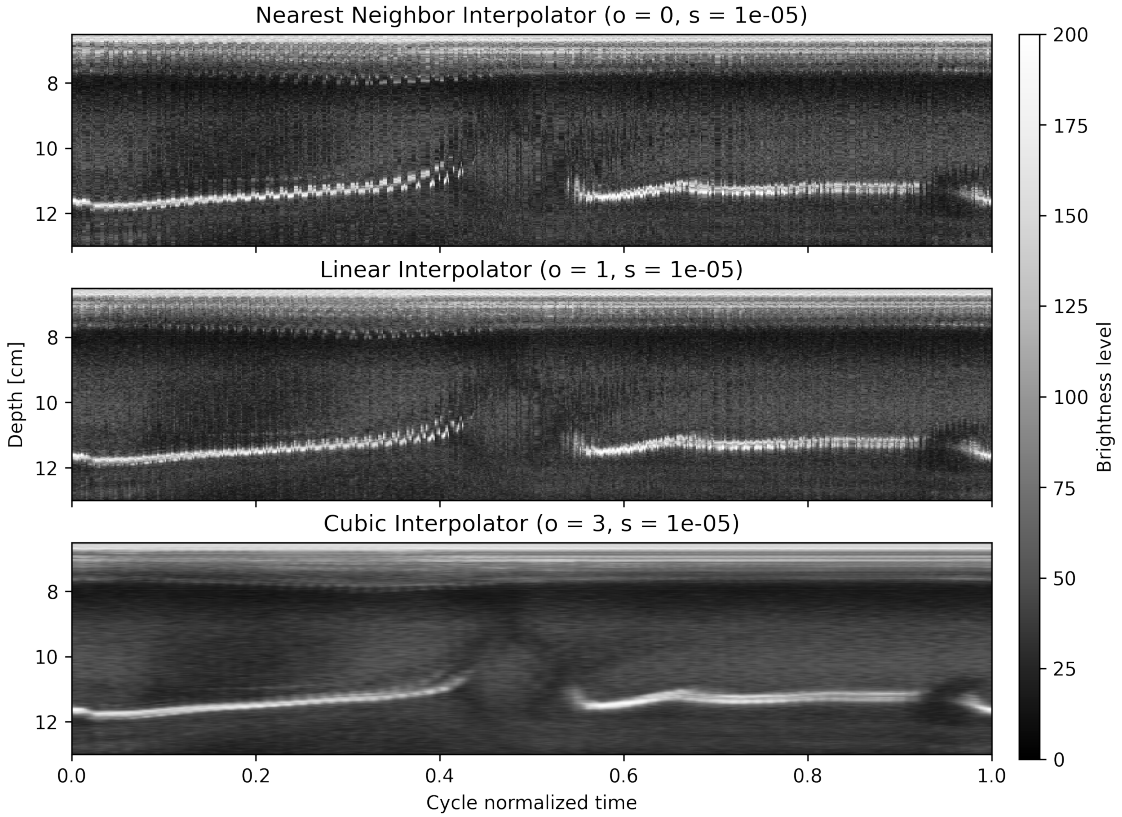

Figure 32: Three interpolation orders are tested, smoothness factor $s = 1 \cdot 10^{-5}$ is kept constant. B-mode images from dataset A1 with $n = 10$ cycles.

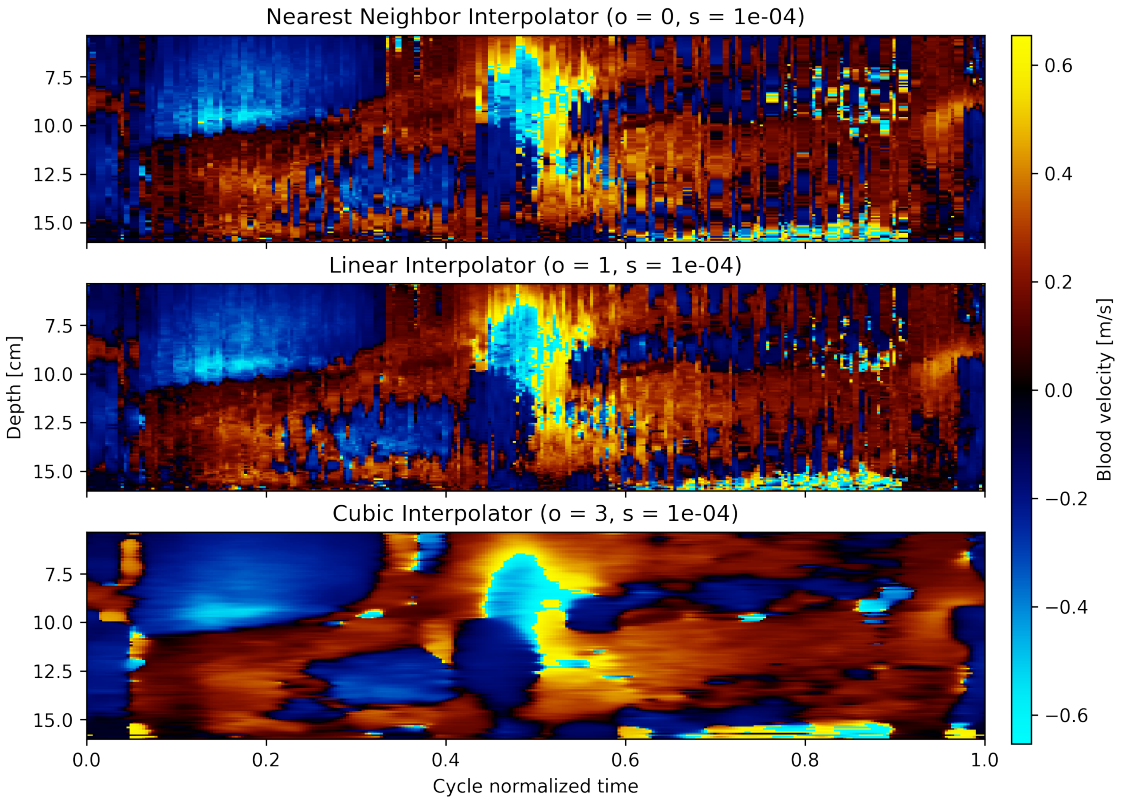

Figure 33: Three interpolation orders are tested, smoothness factor $s = 1 \cdot 10^{-4}$ is kept constant. CF images from dataset A4 with $n = 10$ cycles.

The influence of the smoothness factor

In Figure 34 is the order constant equal to cubic B-splines, $o = 3$ and the smoothness factor varied for three situations. The results show increased smearing of the valve movement as the factor increases. However, for the smallest smoothness factor of $s = 1 \cdot 10^{-6}$ is the flickering artifact again visible. A compromising default setting for Supercycle is choosing the smoothness factor for B-mode as $s = 1 \cdot 10^{-5}$. The trade-off between reducing flickering and reducing the loss of spatial information due to smoothing is again evident. The trade-off is also apparent in the 2D B-mode sectors in Figure 35. The sector with the lowest smoothness factor shows some more details and has higher contrast compared to the other two.

However, even though it is desirable to remove flickering artifacts this comes to the expense of increased smoothing. The spatial resolution decrease with more smoothing as details fade. These effects are seen in both the M-mode acquisitions, but also for 2D B-mode sectors in Figure 35. The sector with the lowest smoothness factor shows some more details and has higher contrast compared to the other two. The trade-off between flickering artifacts and spatial resolution reduction is an important discussion.

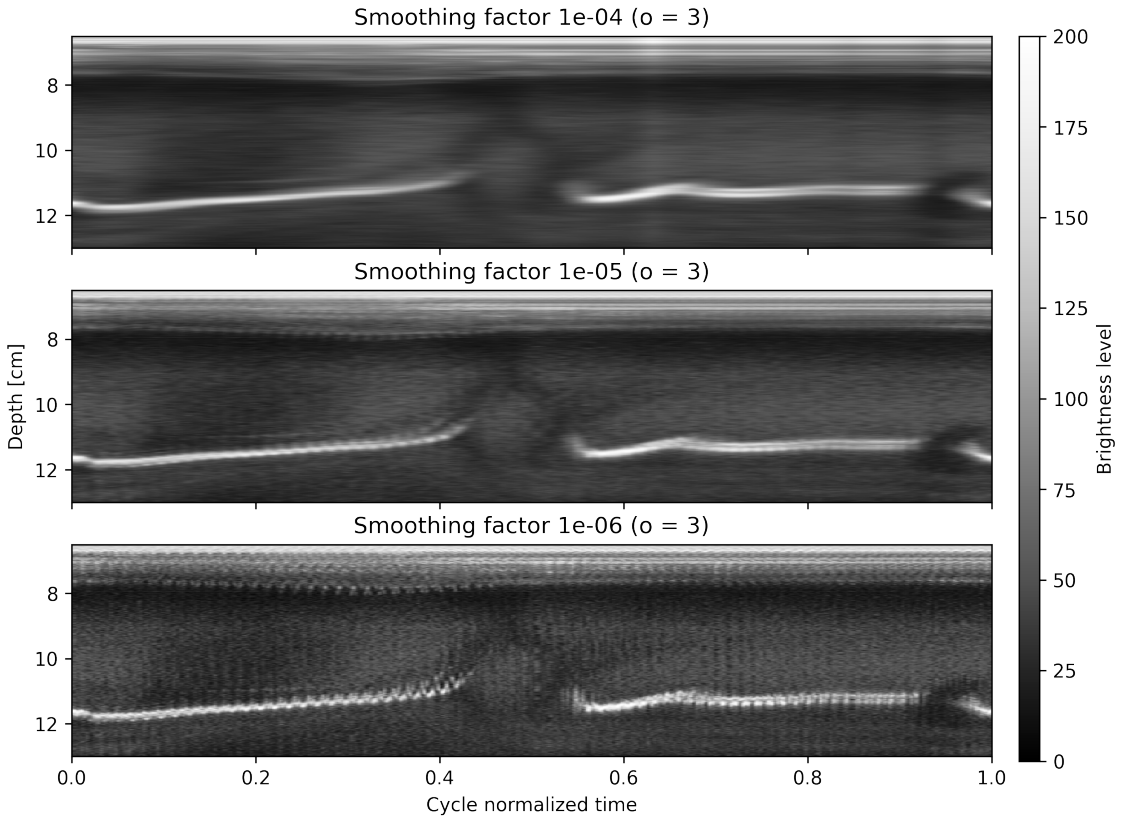

Figure 34: Three smoothness factors are tested, cubic interpolation order $o = 3$ is kept constant. M-mode from B-mode images from dataset A1 with $n = 10$ cycles.

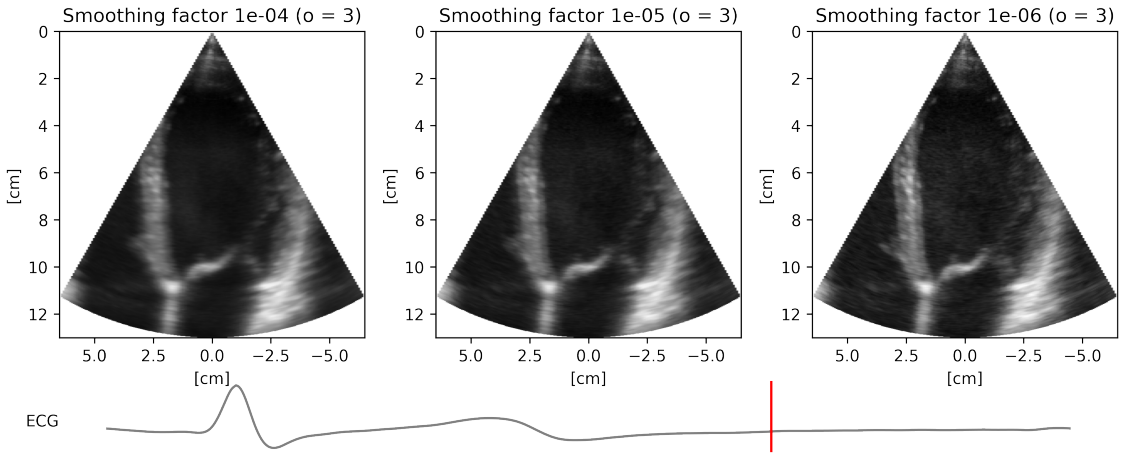

Figure 35: 2D B-mode with the same settings of constant interpolation order $o = 3$ and varying smoothness factor. The images are from normalized time, $t = 0.69$, as marked in the ECG plot with a red line.

Figure 36 compares the varying smoothness factors for CFI shown for M-mode acquisition. There is increased smearing of details as the smoothness factor increase also for CFI. A higher smoothness factor as the default setting is however chosen for CFI than B-mode, as the frame rates are often lower and details smaller in the original data for CFI meaning it can handle more smoothing without loss in resolution. However, too much smoothing decrease the resolution in both time and space, so a compromise for smoothness factor for a Supercycle for CFI is by default chosen as $s = 1 \cdot 10^{-4}$.

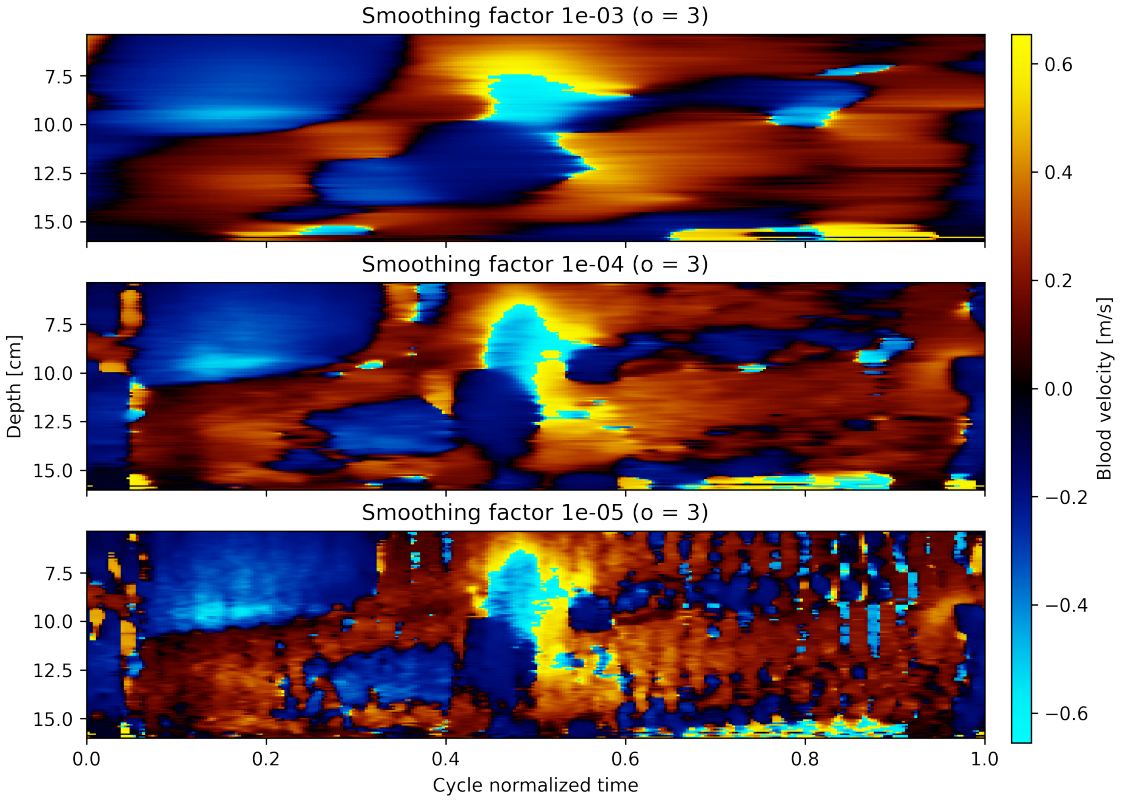

Figure 36: Three smoothness factors are tested, cubic interpolation order $o = 3$ is kept constant. M-mode from CF images from dataset A4 with $n = 10$ cycles.

4.3 Supercycle's performance for triplane imaging

A comparison of the performance of Supercycle to a single cycle for triplane imaging is shown by the M-mode images in the Figures 37-43. Recordings of triplane lower the frame rate as several views and modes are captured, as a consequence are these recordings providing increased spatial information. This motivates the interest in a simultaneous increase of frame rate, potentially provided by the Supercycle.

4.3.1 B-mode triplane performance

Figure 37 and Figure 38 show the performance of a single cycle and the Supercycle on B-mode imaging. The used dataset, A12, is a triplane dataset with B-mode FR equal to 14 Hz. The single cycle has the same setup as the Supercycle, for comparison reasons, with cubic B-splines and a smoothness factor of $s = 1 \cdot 10^{-5}$.

Comparing the M-mode of a single cycle in Figure 37 with M-mode of Supercycle in Figure 38 it is seen a denser and more detailed M-mode signal. The signal of Supercycle looks more natural and has an evidential overall increase in information.

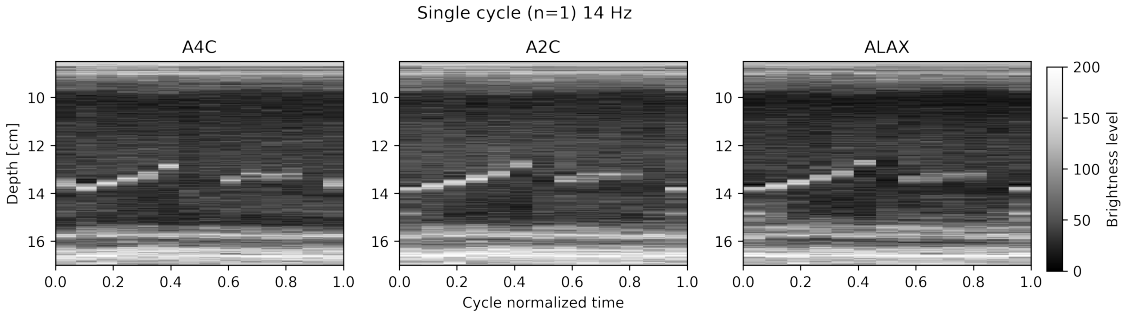

Figure 37: M-mode image of a single cycle from dataset A12. As the original frame rate of the dataset is 14 Hz with a cycle lenght of 0.968 s, this M-mode image contains 14 frames. The cycle is data fitted and remapped by cubic B-splines and smoothness factor, $s = 1 \cdot 10^{-5}$. The setup is equal as for the Supercycle, but only for one cycle (n=1).

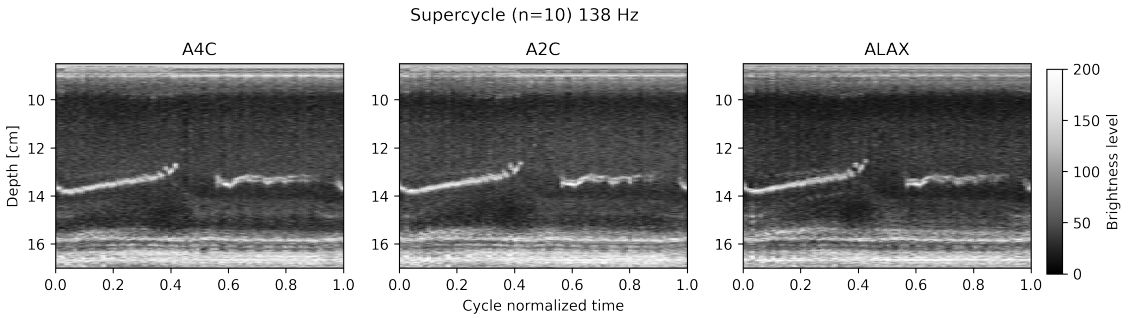

Figure 38: M-mode image of Supercycle from dataset A12. The Supercycle is constructed by combining n = 10 cycles, giving the target frame rate for Supercycle as 138 Hz.

The three apical views are seen in Figure 39, Figure 40 and Figure 41 for normalized time, t ≈ 0.54 (the time is visualized as the red line in the ECG graph below the plots). Notice the differences in the images between a single cycle in Figure 41 and the Supercycle. The differences are because the combined cycles adds information which causes a slightly different view for the same normalized time. Notice also the valve ambiguity in Figure 40, which are not seen in the two other figures. The valve ambiguity is not there in this case of the Supercycle, and further results show that Supercycle has less of these artifacts than data fitting of a single cycle. There are however several results where also Supercycle contains valve ambiguity, an undesired artifact reducing the performance of the method.

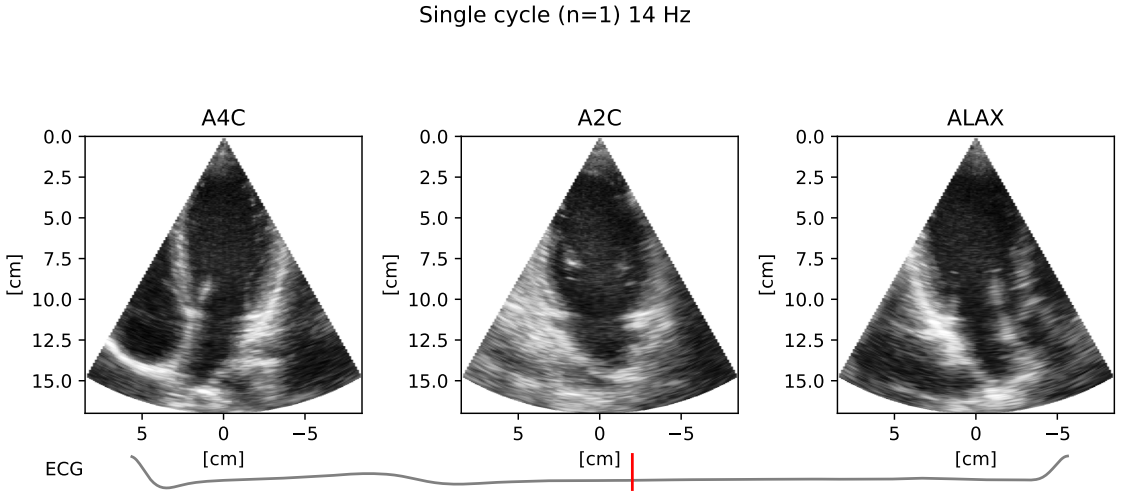

Figure 39: B-mode image of a single cycle for dataset A12.

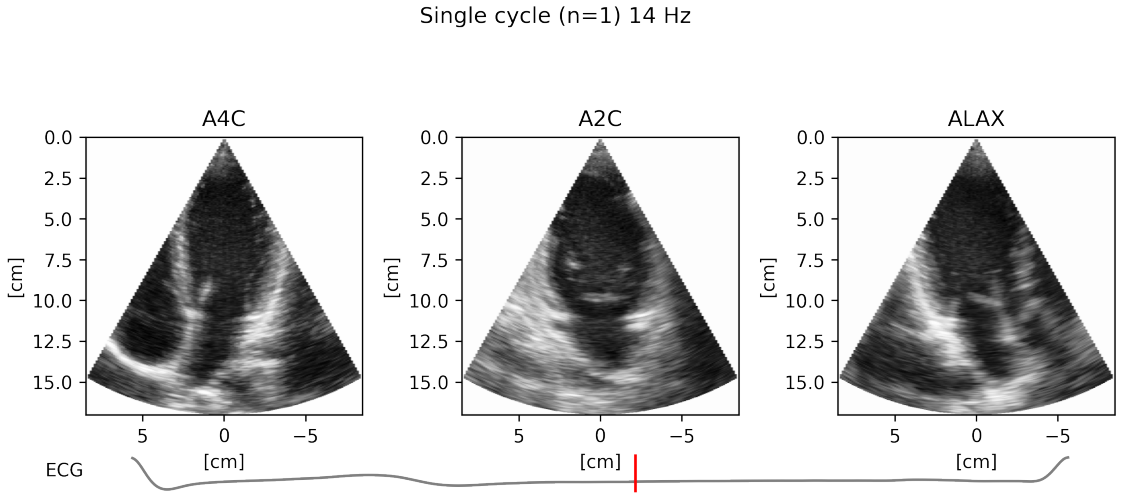

Figure 40: B-mode image of a single cycle for dataset A12. The cycle is data fitted and remapped by cubic B-splines and smoothness factor, s = $1 \cdot 10^{-5}$. The setup is equal as for Supercycle, but only for one cycle (n=1).

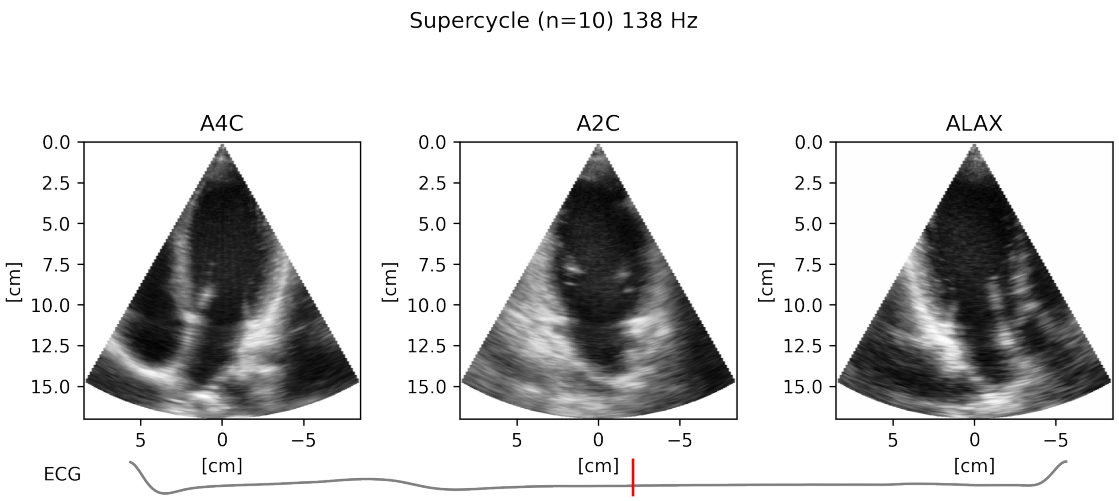

Figure 41: B-mode image of Supercycle for dataset A12.

4.3.2 CFI triplane performance

The same comparison is shown for CFI in Figure 42 and Figure 43. The single cycle has also the same setup as the Supercycle, for comparison reasons, with cubic B-splines and a smoothness factor of s = $1 \cdot 10^{-4}$.Also, the M-mode acquisition of CFI triplane shows a clear improvement in density and continuity for all three views. The target frame rate of 139 Hz is over the twice required frame rate (60 Hz), if calculations of i.e. pressure gradients are desired.

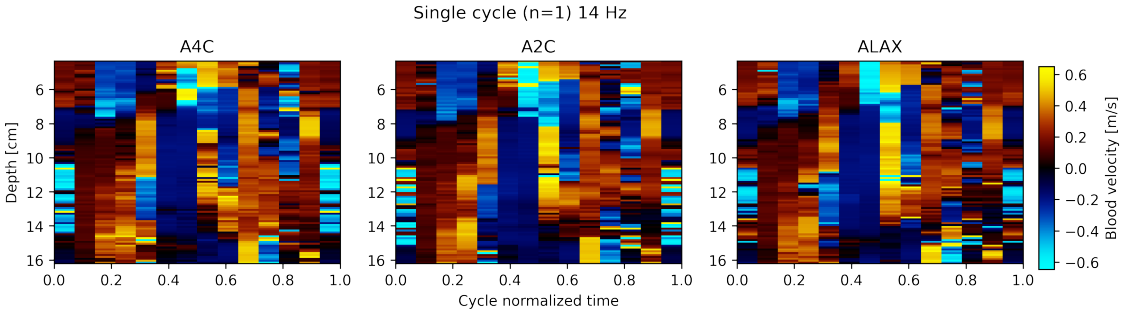

Figure 42: M-mode image of a single cycle from dataset A12. The cycle is data fitted and remapped by cubic B-splines and smoothness factor, s = $1 \cdot 10^{-4}$. The setup is equal as for the Supercycle, but only for one cycle (n=1).

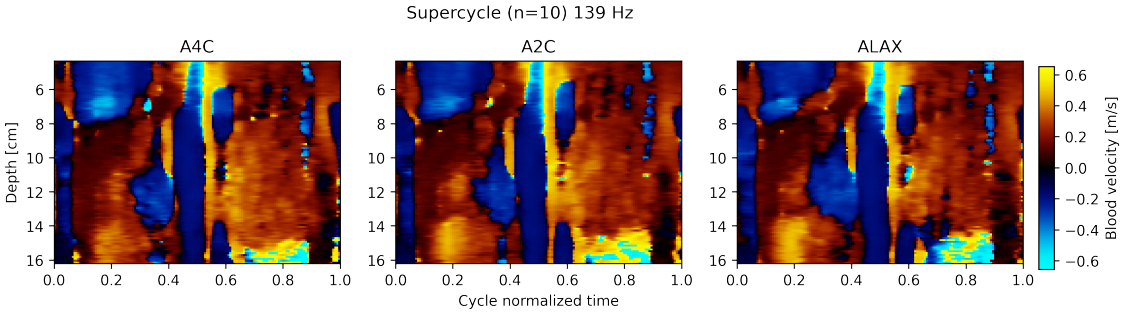

Figure 43: M-mode image of Supercycle from dataset A12. The Supercycle is constructed by combining n = 10 cycles, giving the target frame rate for Supercycle being 139 Hz.

4.4 Results of translation measurement and artifact reduction

After seeing the potential of Supercycle, the selection of cycles, the data foundation, and the sampling distribution were investigated to further improve the results.

4.4.1 Filtering cycle outliers from the cycle basis

Outlier detection is relevant for *Situation III: Breathing heavily* as heavy inhalation creates probe movement which transforms into translation in the FOV between frames. In Figure 44 it is seen a translation of key features located for the exact same time relative to one cardiac cycle. Often are one to three cycles creating flickering artifacts as the probe movement makes them fully out of the FOV as seen in trigger time 4, 5, and 6 in Figure 45. The outlier detection is able to remove these frames for several situations of type *III*.

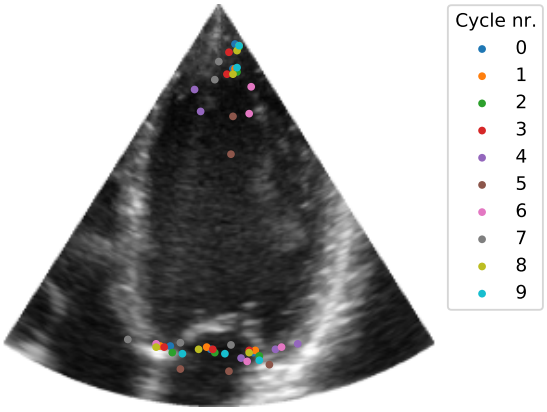

Figure 44: Showing the location of the five key features of dataset A10 for 10 trigger times given by the ECG signal. The spread in key features over time is evident.

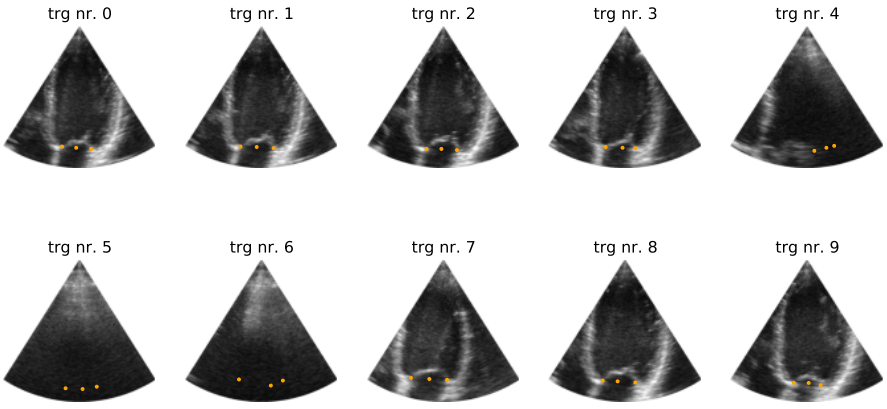

Figure 45: The outlier detection with a Z-score threshold of 1.4 meaning cycles more than 1.4 standard deviations away from the mean are filtered. Cycle 4, 5 and 6 are detected as outliers based on the key feature position in dataset A10.

The M-mode images in Figure 46 show Supercycle of different orders without and with outlier detection. When removing the outliers the white line representing the valve movement is more defined and dense as the flickering artifacts are decreased. Figure 47 shows the sampling distribution before and after outlier removal, notice that the sampling distribution is still relatively dense also after the reduction of cycles.

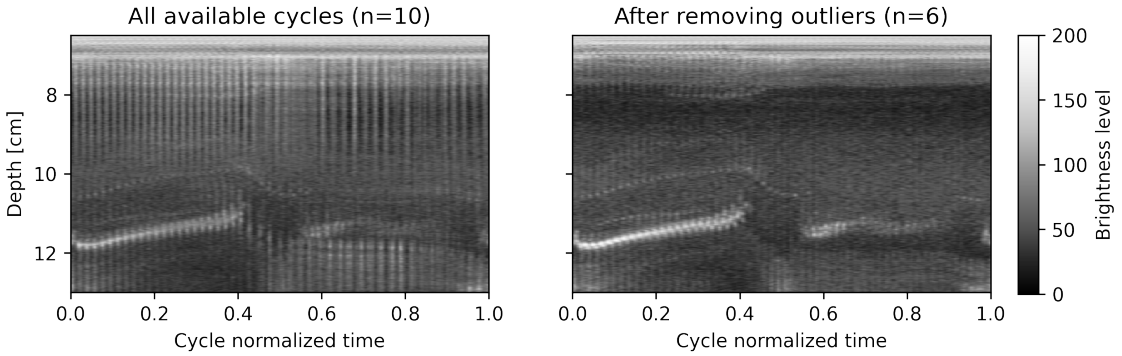

Figure 46: M-mode image of A10 without and with outlier removal. The flickering artifact is reduced after removing the outliers, giving a denser signal for the valve movement and less noise in the area around the valve.

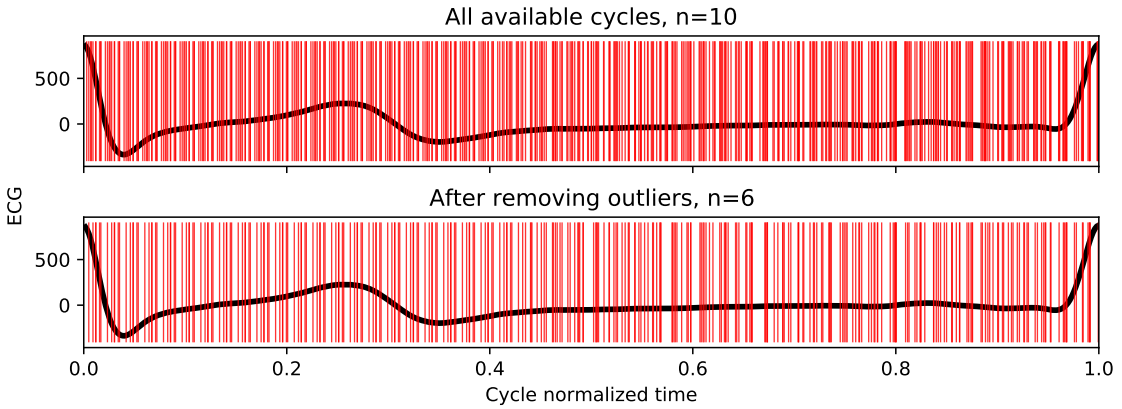

Figure 47: The sample distribution for dataset A10 before and after outlier detection, meaning the number of cycles are reduced from 10 to 6.

The results in Figure 48 - 49 shows the same results for another dataset A2.

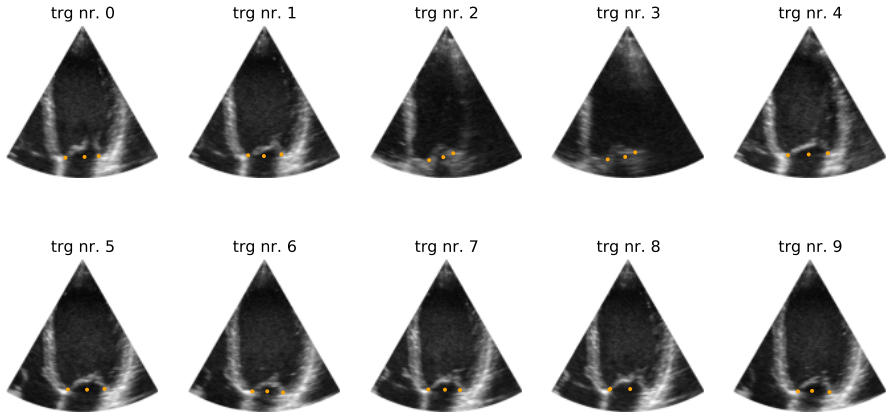

Figure 48: The outlier detection with a Z-score threshold of 1.4 detects cycle 2, 3 and 4 as outliers based on the key feature position in dataset A2. Noticing something wrong with the key features in cycle 8, uncovering a weakness of basing outlier detection on key features. The outlier detection filter out cycle 4 even if it by inspection looks decent. This might be due to the weakness of the Z-score for several data with high mean or standard deviation.

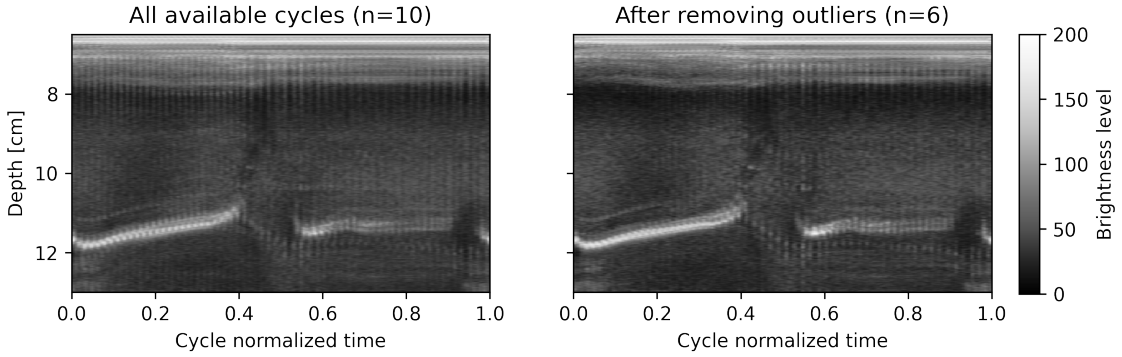

Figure 49: M-mode image of A2 without and with outlier removal. The flickering artifact is reduced after removing the outliers, giving a denser signal for the valve movement and less noise in the area around the valve.

4.4.2 Quantification of translation in FOV

A varying FOV makes an improper data foundation for the Supercycle in terms of stability in the resulting video stream and the basis for interpolating intermediate frames. As the patient breathes heavily the variation in FOV increases, a variation discovered as translation in location of key features. The result is expected due to respiratory motion and movement in the thorax during breathing.

Situational translation investigation

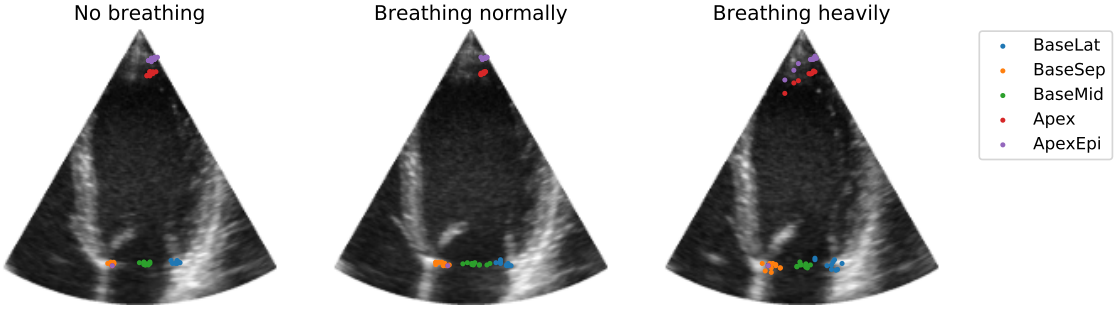

Figure 50: Datasets recorded during three different situations.The 10 cycles are separated by ECG triggers and the key features plotted at each trigger. The key features are found by the machine learning package described in Section 3.5. The B-mode image in the background is from the first frame in each dataset.

Three datasets recorded during different situations *Breathing normally*, *No breathing* and *Breathing heavily* are seen in Figure 50 with its key features marked at trigger time R-peak during 10 cycles. Table 4.2 summarize the translations between points with the use of the Euclidean distance, confirming the translation differences for the three situations where situation *no breathing* has lowest translation and situation *breathing heavily* has most translation. A comparison of all datasets in the three specified situations is shown in Table 4.3. The table confirms the results from Figure 50 and Table 4.2.

Key Feature	A1	A0	A2
BaseLat	14.0	42.8	34.9
BaseSep	4.0	18.4	23.5
BaseMid	11.3	17.1	16.8
Apex	13.5	15.1	65.5
ApexEpi	17.5	15.1	67.7

Table 4.2: The Max Euclidean Distance in pixels is calculated between all pairs of points for each key feature. The machine learning package is in some cases less precise in finding the key features. This results in wrong calculation of translation which can be seen in *BaseLat* for A0 which is equal to 42.8 pixels. The result is higher than *BaseSep* for A2.

Situation	Mean
I : No breathing	22.1
II : Breathing normally	35.1
III: Breathing heavily	110.9

Table 4.3: Mean of all Max Euclidean Distances for each situation. The situation of *breathing heavily* shows a notable translation increase which is due to massive FOV translation as the patient inhales deeply.

Figure 51 shows M-mode images of the three situational datasets for Supercycle constructed by n = 10 cycles. The visible white signal is the movement of the left valve over one cardiac cycle. Flickering artifacts appear as the translation increase making the white signal of valve movement less dense.

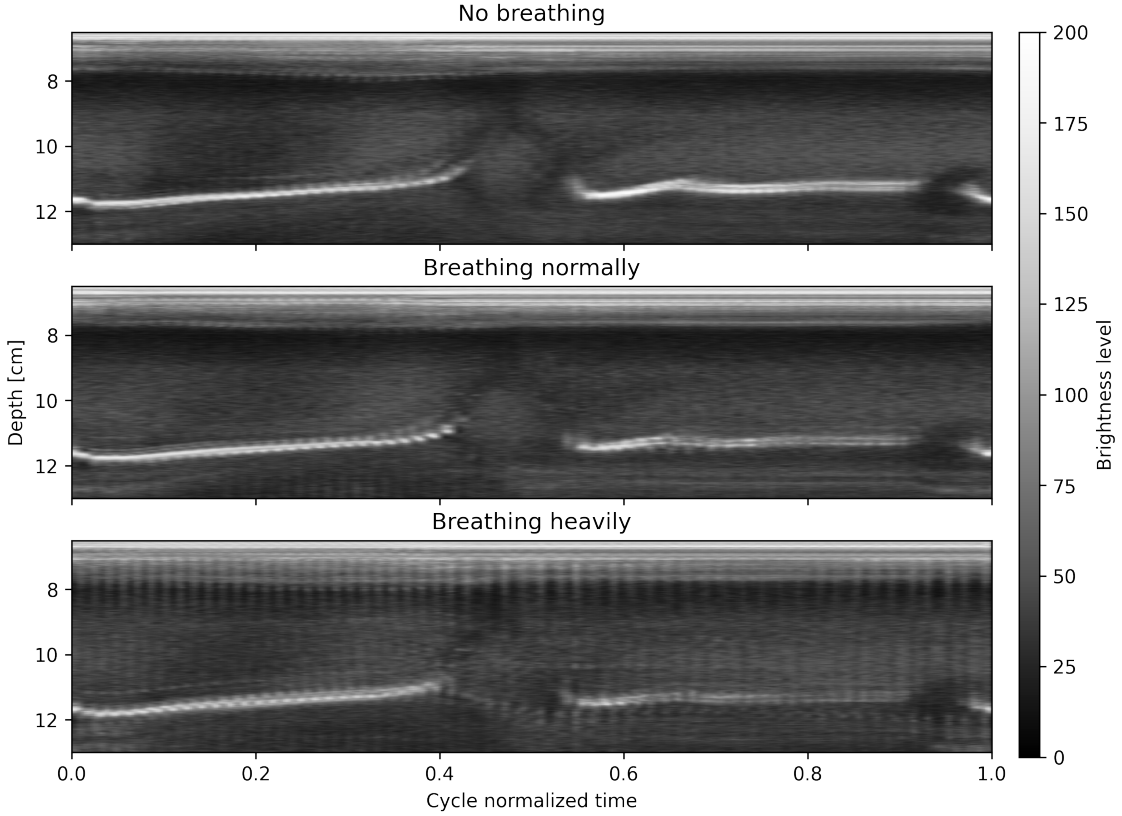

Figure 51: Construction of Supercycle for each dataset representet as M-mode images. As the amount of translation increase the less dense and defined is the valve movement. The frame rates for Supercycle for the three datasets are ≈ 650 Hz.

Translation quantification for all datasets (Data A) The max euclidean distance for each key feature in all datasets (in Data A) is seen in Figure 52 and shows the translation trends in the data sorted by key features. The trends show less translation in Apex and ApexEpi, which is confirmed by the mean, μ, noted below each feature name in the same figure. As the translation is less evident around apex it motivates the idea of doing a translation correction by a rotation around apex, as this will correct for more translation in base and less in apex (as described in Section 3.6). Section 4.4.3 shows results of using rigid co-registration for such translation.

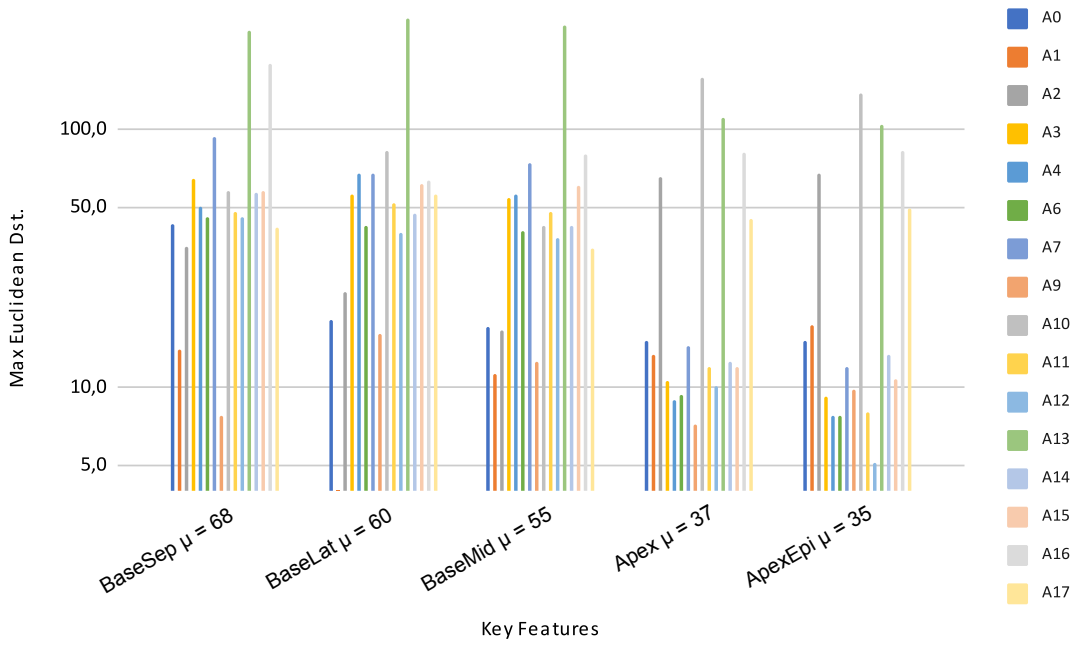

Figure 52: Chart of Euclidean distances for all datasets and key features.

4.4.3 Spatial alignment with rigid co-registration

Rigid co-registration is performed on dataset A4 as a first attempt for translation correction. The dataset contains translation which is slightly below average translation for all investigated datasets.

Figure 53-55 show the result of the transformed view by the rigid co-registration compared to a non-transformed view. The lines shown in the figures are the lines from Apex to BaseMid. The three figures correspond to the three different trigger times extractions, ECG, ED, and ES, as described in Section 3.6. Figure 53 and Figure 54 show that the transformation is able to correct for small displacements of the apex line. Even if larger displacements are corrected for in Figure 55, there still exists some displacement in especially the x direction.

In Figure 56-58 M-mode images are used for further investigation of the transformed results. The dataset, A4, is an example of how triggers from ECG and ED triggers show better performance than ES triggers. In several datasets, the ECG-provided triggers and ED triggers are more consistent in actually finding the correct key features, suggesting that these are preferred for trigger times. ECG is, in addition, able to provide more trigger times than the machine learning package. With extra trigger times, more information of the translation over the cycles is available when constructing transformation matrices for the rigid co-registration.

From Figure 56 it is seen fewer flickering artifacts in the transformed M-mode image of the valve movement compared to the transformed M-mode images from ED triggers in Figure 57 and especially ES triggers in Figure 58.

However, the Figures 56-58 all show that the non-transformed datasets have the best performance overall. They appear most precise and with less flicker in the valve movement than for the transformed data.

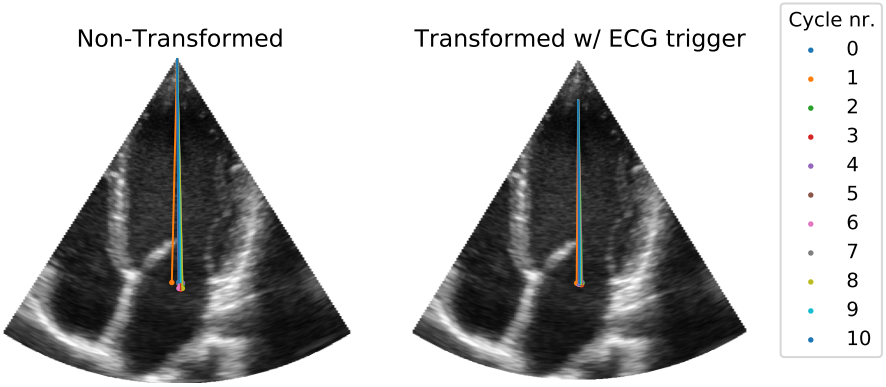

Figure 53: Some translation is reduced from the Non-Transformed to the Transformed Apex lines. Here is the transformation based on R-triggers from the ECG signal.

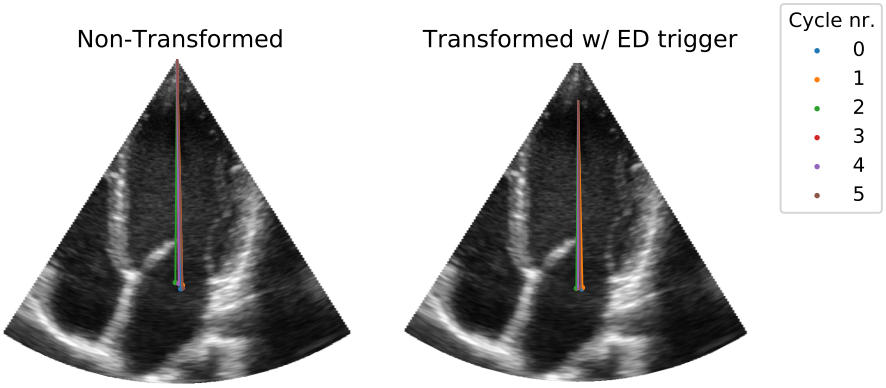

Figure 54: Similar results as for the ECG trigger based transformations. Here is the transformation based on ED trigger points from the machine learning package.

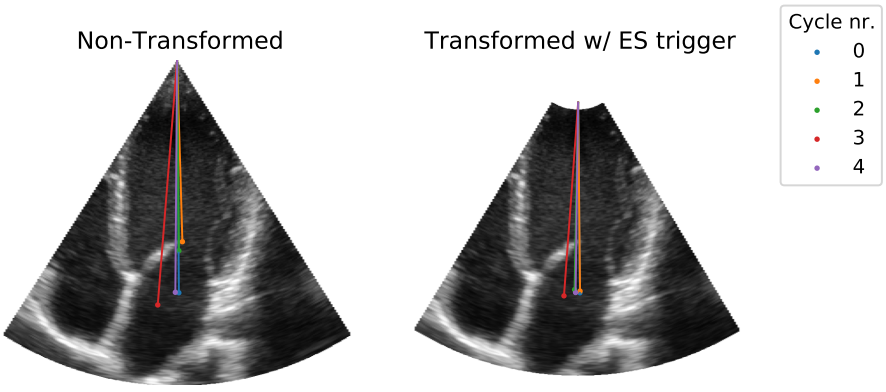

Figure 55: Some translation is reduced also when using ES trigger points from the machine learning package. However, there are still visible variations in the Apex lines.

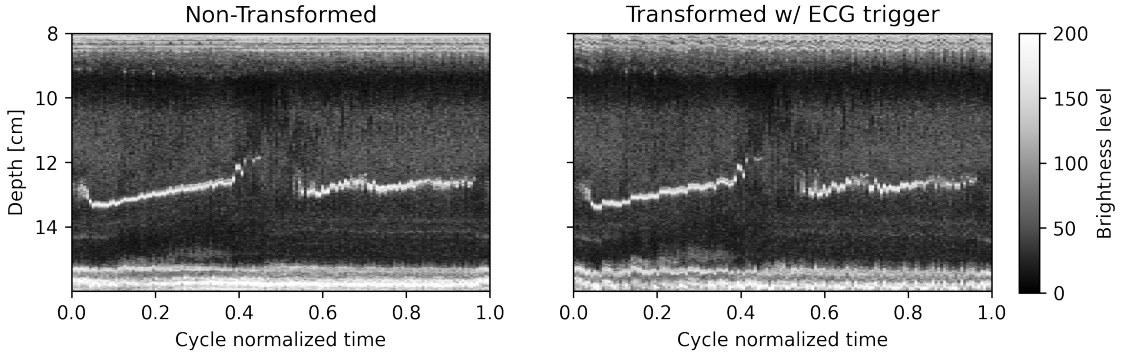

Figure 56: M-mode image of A4 before and after transformation based on trigger points from ECG.

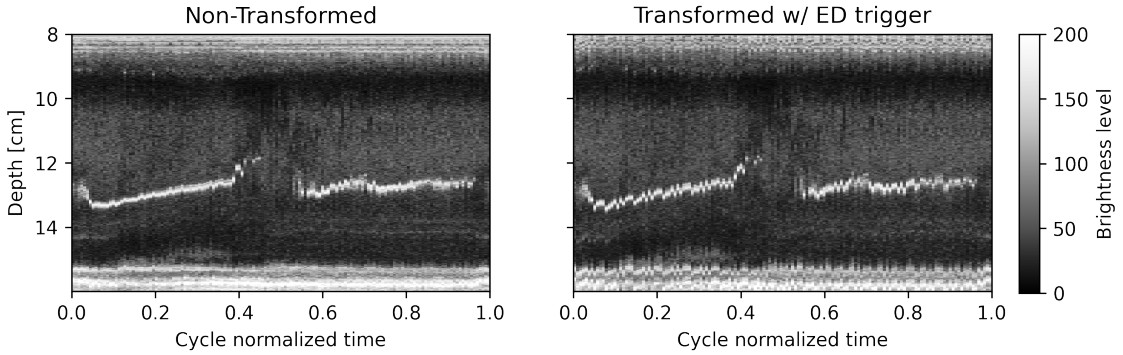

Figure 57: M-mode image of A4 before and after transformation based on ED trigger points.

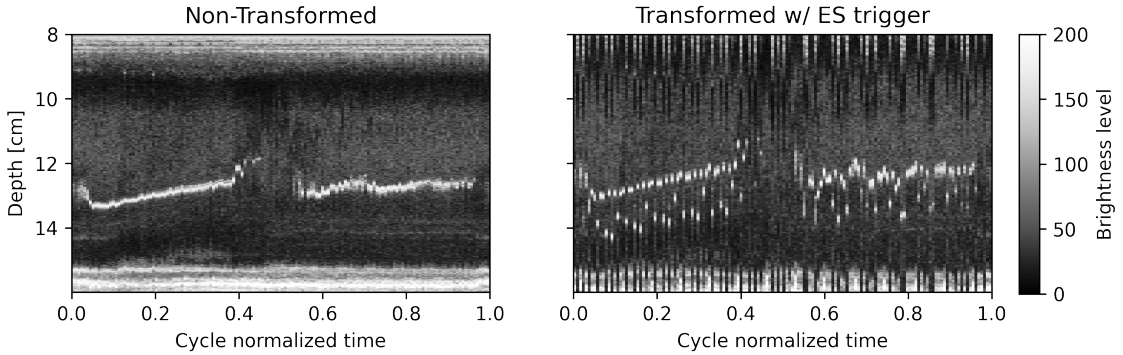

Figure 58: M-mode image of A4 before and after transformation based on ES trigger points.

4.5 The correlation between heart rate and frame rate

The sampling distribution is the offset between samples from consecutive cycles normalized to one overall cycle. The offset is determined by the relation between the heart rate (HR) and the sampling frequency, the frame rate (FR).

Figure 59 shows an example of a sample distribution for dataset, B5, shown on top of one ECG cycle. The $n = 11$ cycles are normalized between 0.0 - 1.0 , from originally having a mean cycle length of 0.917 s and standard deviation of 0.034 s. The colored vertical lines represent the samples where each color corresponds to a cycle. The black vertical lines represent the first cycle, to mark the original sampling frequency.

The sample lines from different cycles appear for different normalized times due to the HR-FR offset. The samples are in addition not uniformly distributed due to inconsistency in HR as seen by its denser areas and more sparse areas.

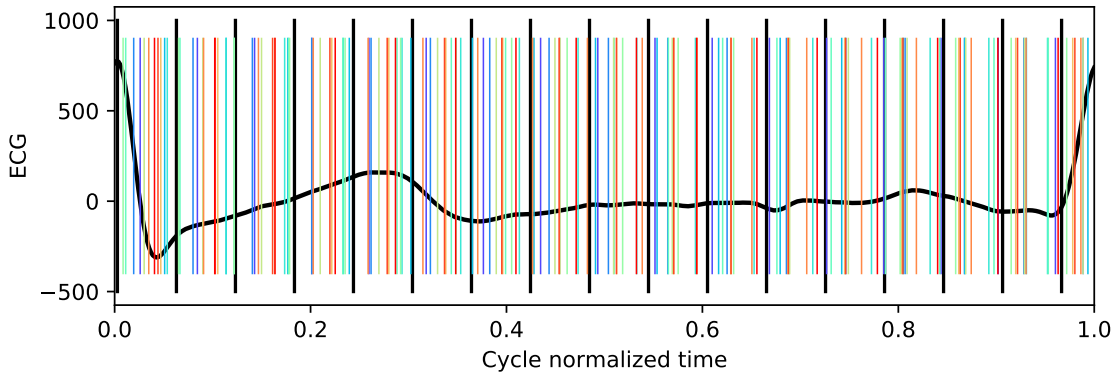

Figure 59: Visualizing the sampling distribution for B-mode data for dataset B5. The data is originally sampled with a frequency of 19 Hz. The 11 cycles concatenated shows non-uniformity in sampling, but still covers the heart cycle better than one cycle as the FR is increased by a factor of 11.

Comparisons of the sample distribution for different FRs are seen in Figure 60 - 62. The results show that increased FR on average increases the sample coverage of the overall cycle, as seen for the different FR's. However, Figure 61 shows a dataset with higher FR but less cycle coverage than the dataset in Figure 62. A very small offset between HR and FR gives clusters of samples and a less uniform distribution, underlining the sensitivity of the correlation between HR and FR.

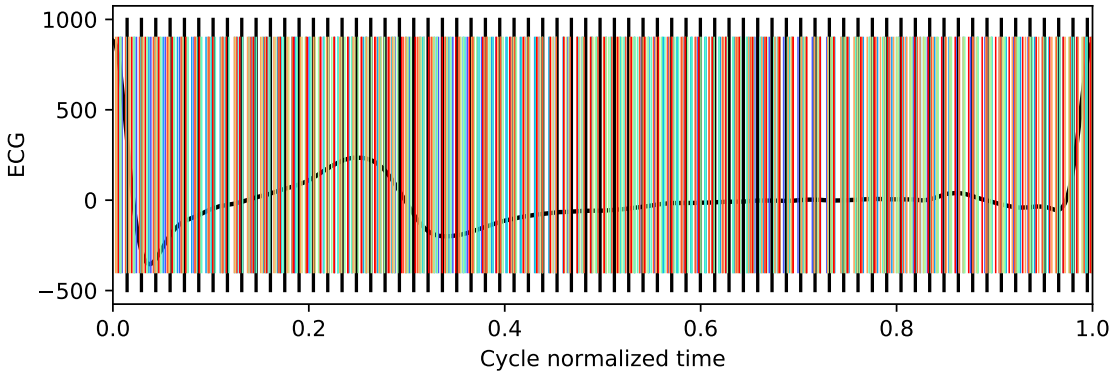

Figure 60: Dataset A1 with a high frame rate, $FR = 65$ Hz.

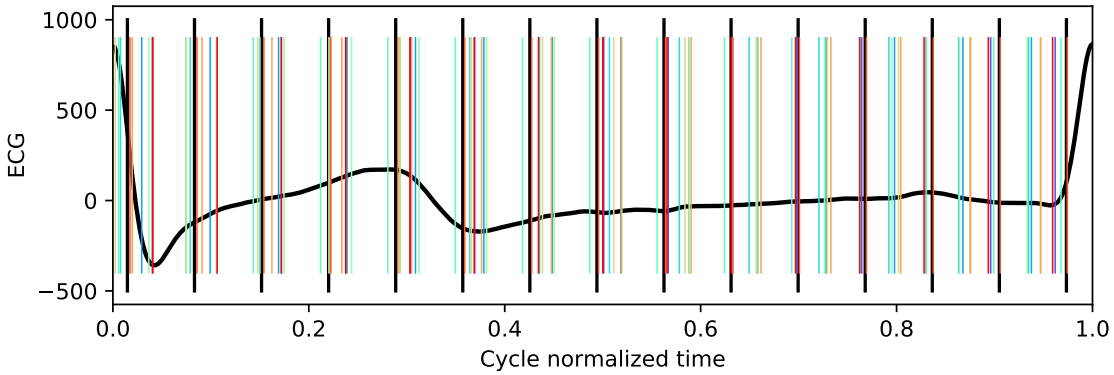

Figure 61: Dataset A14 with a medium frame rate, $FR = 15$ Hz.

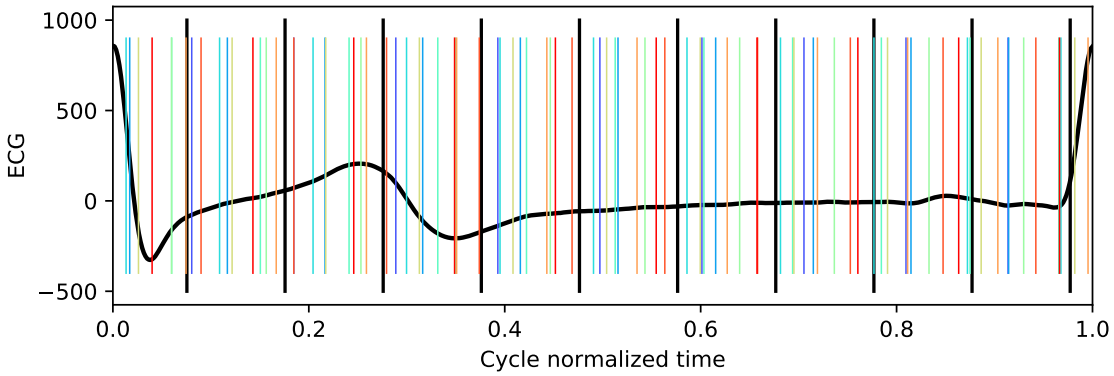

Figure 62: Dataset A15 with a low frame rate, $FR = 9$ Hz.

5 Discussion

5.1 Supercycle's performance

The principle of combining several cycles to increase the temporal information for an overall cycle is shown theoretically satisfactory already in Figure 1. It is seen as the sampling becomes denser and covers the overall cycle to a greater extent. The optimal frame rate from the Supercycle is an up-scaled version of the original sample rate. Scaled by a factor of n, suggesting that for a higher n, a higher frame rate is gained.

The result is confirmed in the M-mode acquisition of B-mode in Figure 20 and CFI in Figure 21. Even in the case of only $n = 3$ a substantial improvement is seen. This result is of importance because three cycles are often available in the old recordings. Further, recordings of only three cycles is in practice giving decreased acquisition time, which might decrease translation due to probe instability and easier breath holding.

In addition, the comparison between 2D B-mode of a single cycle and Supercycle in Figure 40 and Figure 41 show that some ambiguity of the valve movement is reduced when increasing n, a potential result of having more information of the valves over time and correct timing of the combined cycles.

The overall performance of Supercycle shows great potential in gaining more temporal information of the valve movements in addition to solving issues regarding low frame rates in e.g. determining pressure gradients and other quantitative measures from CFI. Supercycle is further potentially increasing the information gained from triplane imaging, as Supercycle provides frame rates with an upscaling of 10 compared to a single cycle and with more precision in space, especially for CFI.

5.2 The Supercycle framework

The chosen settings for Supercycle included using split method 1 for the most reliable performance. This method also performed well in the situation when the patient has a high pulse. This situation is interesting as it gives knowledge of the performance of the methods for patients that normally have a higher pulse, such as infants. Having a separation method working in these cases is an important factor as Supercycle is partly motivated by imaging of faster beating hearts. On the other hand, split method 1 shows notably increased spread for the high pulse situation compared to the situations for a lower pulse, but was able to separate cycles with an overall similarity in shape and precision in trigger time.

The results from the different normalization methods show potential in performing partly normalization of the cycles. As trigger times from ECG were most robustly defined, this setting was chosen for the Supercycle in combination with the normalizing the diastolic phase. A limitation of using the trigger from the machine learning package is if the package cannot find a trigger time within all cycles separated by trigger times provided by the ECG signal. This happens for datasets with either low FR or severe translation in the FOV, making it hard to analyze the images for timing information. When ES is not found within the cycle the method cannot correct for cycle differences and is not preserving original timing information.

5.3 Ambiguity in the valves

The valve ambiguity artifact is evident in several results of the Supercycle. The valve ambiguity suggests that there still exists some non-preserved timing, seen as duplicated valves for one frame. The valve ambiguity might also be due to different valve moving patterns from cycle to cycle, in this case, the artifact might happen even if the cycles are joined with preserved timing. In addition, for low frame rates, there could be an open valve in one frame and a closed in the next. The intermediate frame will then be an interpolation between those frames and thus contain information from both, giving valves in two places, still an issue also for Supercycle. However, several comparisons of a single cycle and Supercycle showed a decrease in these situations for the Supercycle.

5.4 The smoothness trade-off

The remapping of axes is for converting Supercycle to a uniform time grid. An order of the B-splines and a smoothness factor are chosen in this remapping process. The results when varying order and smoothness uncovered an important trade-off for the Supercycle framework.

The trade-off between flickering and smoothness needs to be evaluated in relation to the Supercycle application. As stated, small details are less important for CFI than B-mode, meaning a higher smoothness factor can be applied for CFI. In B-mode, the 2D images require a high quality resolution to precisely view the details of the mitral valve, however, M-mode acquisition allows some loss in spatial resolution if gaining a more natural view of the valve. An increased smoothing effect gives adequate results in this mode as it decreases flicker and variance. It is further desirable that the video recording of a full Supercycle appears physically correct and is perceived as reasonable as the state-of-the-art cardiac cycle. This is important in practice in interpreting the cardiac ultrasound for the clinicians.

With the discussed applications, the smoothess factor is a possible parameter when tuning the Supercycle for its respective application. In addition, for a poor data basis with high translation and severe flickering, the smoothness factor can be tuned for a compromised result still giving some information of the recorded heart.

The smoothness of Supercycle is not only due to B-spline settings. As observed in Figure 20 is the improvement of a Supercycle with $n = 10$ over $n = 3$ not obvious. As a matter of fact, the valve movement of the Supercycle with $n = 3$ is appearing brighter and more precise for normalized time $t = 0.4$. This is possibly a result of performing data fitting with cycles that are not accurately aligned. In theory, will a larger n decrease variation during data fitting, in practice, is however misalignment between frames smearing out details giving a smoothness effect and loss in spatial resolution. Consequently, is the number of cycles, n, and stability of the data foundation also affecting the spatial resolution of Supercycle. Choosing a big n when having sufficiently aligned frames is a form of information fusion potentially serving as an effective speckle reduction algorithm. As discussed is the smoothness effect beneficial in decreasing noise and variance in some applications, such as M-mode, again emphasizing the application-specific trade-off.

5.5 Outlier detection

A simple outlier detection also succeeds in decreasing flickering artifacts. The method works mainly on datasets where only the minority of cycles distinctly deviate from the rest by having a high amount of translation. This is often the case for the situation *Breathing heavily*, a situation that usually is avoided during the ultrasound examination. However, showing potential in increased performance for challenging situations uncover methods for also increasing Supercycle for regular situations.

The Z-score as outlier detection works as desired when the cycles are mainly similar. As the total number of available cycles is often small, $\approx 10 - 12$ cycles, it means only five diverging cycles will profoundly influence the outlier detector. This is a result of the calculation of the Z-score, based on the mean and standard deviation of cycle translation. Usage of the Z-score for deciding outliers is consequently challenging when a dataset contains many cycles that should have been categorized as outliers. Nevertheless, this kind of dataset is often containing unsatisfactory high amounts of translation which overall makes it unsuited for the Supercycle.

5.6 Pre-processing and artifact reduction

Instability in probe placement and respiratory motion are shown to affect the Supercycle performance and are mainly seen as a flickering motion. The artifact is both seen in resulting video streams and from several M-mode acquisitions in the results.

These artifacts are due to translation in the FOV as the cycles extend longer for large n, causing increased influence of probe displacement. In addition, is the artifact more evident in situations where the patient is either breathing normally or heavily as the respiratory motion increase and stable placement of the probe is challenging.

As discussed, the artifact is reduced when increasing the smoothness factor or the number of concatenated cycles, n. However, both procedures often limit spatial information, an unwanted effect. The trade-off motivated a pre-processing of the data for utilizing as much available spatial and temporal information as possible.

The quantitative measures of translation, calculated from the location of key features in each trigger frame, give a good indication of whether the dataset should be rejected or is fit for Supercycle. High translation measures were especially evident for the situation *Breathing heavily*, and based on these measures the datasets for this situation were mainly rejected for Supercycle.

As one of Supercycle's strengths is being a retrospective method with the possibility to be applied on old datasets it is not desirable to reject datasets even in case of visible translation. To overcome artifacts due to the translation a rigid co-registration was implemented.

The three Figures 53, 54 and 55 show potential in decreasing the translation seen in the apex lines, with variational results depending on the used trigger time. It is mainly the datasets with a low amount of translation originally that the transformation procedure works satisfactorily. The co-registered transformation based on the location of key features suffers from the not entirely precise location of key features in combination with a probably too simple co-registration only based on mean translation between Base features. The transformation was thus not deployed on the Supercycle results, as improvements in the co-registration and transformation are evident

for satisfactory performance. Even though the results were not satisfactory at this point, some potential is uncovered in using key features found by machine learning for co-registration of frames. The method is highly relevant as it is neither invasive nor in need of any additional equipment during the examination.

The results are a starting point for a more comprehensive study of the FOV alignment in 2D B-mode imaging. Being able to decrease misalignment is potentially highly effective for Supercycle performance. Accurately aligned frames will reduce variance without introducing heavily smoothing artifacts, meaning it could potentially be one solution to overcome the smoothness-flickering trade-off.

5.7 The heart rate and the frame rate

Samples from different cycles would end up at the same time in the overall cycle if it was not for the offset between HR and FR. The fact creates the idea of gaining more information of an overall cycle by joining several cycles, the idea of the Supercycle, and an effect visualized in Figure 59.

Even if it is common to assume a constant HR, and thus a constant offset (as FR is constant) the results show that there are in practice are variations in HR. These variations cause an inconsistent offset, which in practice is seen as clusters of samples throughout the overall cycle. However, an optimal offset could be determined if the HR was constant and FR tuned in real time[10]. In the term *optimal* is the idea of maximum gathered information for the n cycles, meaning a uniform sampling distribution. However, since HR varies over time an optimal calculated FR for one HR will not be optimal throughout the recording. Optimal sampling distribution could also be determined in the Supercycle framework by choosing the joined cycles as those covering the maximum amount of the overall cycle. Some investigations were performed for this, but results showed that maximum number of cycles after outlier removal gave best information.

5.8 Further work

The proposed method of the Supercycle has shown potential with contribution of higher frame rate ultrasound videos and preserved spatial information. Especially in the case of CFI has Supercycle potential in providing higher frame rate sequences for quantitative analysis of the blood flow, such as pressure gradients. The potential shown motivates a section describing potentially further improvements and research.

5.8.1 Independence of ECG

Even though the results show the best robustness when using ECG signals over machine learning for timing information, the ML has shown potential in separating Supercycle from its dependency on ECG. This independence of ECG is preferable as it simplifies the medical examination, making Supercycle even easier to utilize. Also, the mean of frames method for extracting trigger times in cycles worked for several cases. The method was fairly simple and needed manual tuning but showed the potential of utilizing the information from the ultrasound data directly for timing purposes.

5.8.2 Co-registration potential

The co-registration transformation method for aligning frames needs further investigation for satisfactory results. The procedure is potentially an efficient way of increase Supercycle performance by succeeding to resolve the discussed trade-off.

ML contributed with key feature localization used for translation calculation and FOV transformation. As described in 2.1.5 proposed methods for translation and respiratory motion detection contains holding the breath, using sensors for motion tracking, or invasively inserting markers. They all limit acquisition or challenge the strengths of ultrasound. Using ML to recognize and localize features between frames is simple as it's not influencing the actual medical examination but done in the pre-processing step of the Supercycle.

5.8.3 Increased complexity of interpolation grid

Higher-order B-splines were able to preserve spatial information while remapping the time axis. The complexity increased when introducing higher orders, however, the results often improved. This motivates even more complex interpolation grids.

The idea of a specifically designed interpolation grid containing the expected blood flow pattern is proposed for CFI in particular. The expected or estimated pattern for this grid could be the physical equations of flow, such as the Navier-Stokes equations. In addition, a pre-trained grid from machine learning of high temporal resolution blood flow or valve movement could also contribute with vital information in practice of the flow and motion during the cardiac cycle. Especially could optical flow be used for such pre-information for both B-mode and CFI.

6 Conclusion

This thesis aimed to investigate whether a retrospective combination of sequentially recorded cycles could improve temporal resolution without affecting spatial resolution for in-vivo ultrasound recordings. The Supercycle method was deployed and evaluated for both B-mode and CFI data separately, and the duplex modality for triplane acquisition. An additional purpose of the thesis was to uncover the influence and importance of surrounding conditions such as the data foundation and the relation of HR and FR.

The Supercycle was able to increase the triplane frame rates from 14 Hz and up to approximately 140 Hz, which is a notable improvement over the state-of-the-art performance. The increase in temporal resolution did in some cases decrease the distinctness of small structures. Especially in B-mode was a smoothing artifact evident, reducing the contrast of the mitral valve. However, the overall results showed a significantly higher temporal increase than spatial reduction.

The chosen default settings for the Supercycle framework included timing information from ECG signals as these showed significant robustness in defining trigger times. However, the machine learning package has potential in making the Supercycle independent of ECG, as it in most cases provided satisfying trigger times. Such independence is desirable to simplify the medical examination, making the Supercycle fully based on ultrasound imaging data.

To preserve the timing information after concatenation of cycles, they were normalized. Normalization of diastole shown improved performance, as the cycles vary most in this phase. A set of B-splines satisfactory remapped the normalized cycle time to a uniform axis. Cubic B-splines were chosen as the default order to minimize smoothing and further prevent unnatural patterns introduced by very high orders.

The Supercycle was however suffering from several artifacts. Undesirable smoothing was evident for several situations. Firstly the smoothness factor itself had to be small enough to preserve maximum spatial information. And secondly, a high n introduced smoothness when the combined frames were not properly aligned.

On the other hand, some smoothing improved the overall results by decrease the flickering artifact and variance of not properly aligned frames. The trade-off between smoothness and flickering is an important discussion for improved performance of the Supercycle.

However, these flickers can be removed already in the pre-processing of the data, if being able to determine a robust transformation method for aligning frames An attempt was made for improving the stability of the Supercycle data foundation by a simple co-registration based on machine learning key localization. Using machine learning for this purpose showed great potential, even if the specific co-registration method did not meet its requirements this time.

If future research focuses on the before-mentioned data instability correction, in addition to an application-specified interpolation grid, the Supercycle might have potential as a novel method in multiple applications. Such applications include pressure gradient calculations in patients with higher pulses. The Supercycle method has shown potential, suggesting it to be a future contributor to vital data in clinical cardiology.

Bibliography

[1] A. Timmis, N. Townsend, C. P. Gale *et al.*, 'European society of cardiology: Cardiovascular disease statistics 2019', *European Heart Journal*, vol. 41, no. 1, pp. 12–85, 2020, ISSN: 15229645. DOI: 10.1093/eurheartj/ehz859.

[2] 'Hjerte- og karsykdommer i Norge', *Folkehelserapporten - Helsetilstanden i Norge [nettdokument]*, [Online]. Available: https://www.fhi.no/nettpub/hin/ikke-smittsomme/Hjerte-kar/?term=%7B%5C&%7Dh=1.

[3] *Hjertefeil*, 2019. [Online]. Available: https://www.ffhb.no/hjertefeil/ (visited on 3rd Jun. 2021).

[4] R. R. Richardson, MD, *Atlas of Acquired Cardiovascular Disease Imaging in Children*. 2017, ISBN: 9783319441139. DOI: 10.1007/978-3-319-44115-3.

[5] E. Chérin, R. Williams, A. Needles, G. Liu, C. White, A. S. Brown, Y. Q. Zhou and F. S. Foster, 'Ultrahigh frame rate retrospective ultrasound microimaging and blood flow visualization in mice in vivo', *Ultrasound in Medicine and Biology*, vol. 32, no. 5, pp. 683–691, May 2006, ISSN: 03015629. DOI: 10.1016/j.ultrasmedbio.2005.12.015.

[6] A. Petrescu, 'Concepts and applications of ultrafast cardiac ultrasound imaging', no. December 2020, pp. 1–9, 2021. DOI: 10.1111/echo.14971.

[7] S. Wang, W. N. Lee, J. Provost, J. Luo and E. E. Konofagou, 'A composite high-frame-rate system for clinical cardiovascular imaging', *IEEE Transactions on Ultrasonics, Ferroelectrics, and Frequency Control*, vol. 55, no. 10, pp. 2221–2233, 2008, ISSN: 08853010. DOI: 10.1109/TUFFC.921.

[8] T. Tanaka, T. Okada, T. Nishiyama and Y. Seki, 'Relative pressure imaging in left ventricle using ultrasonic vector flow mapping', *Japanese Journal of Applied Physics*, vol. 56, no. 7, 2017, ISSN: 13474065. DOI: 10.7567/JJAP.56.07JF26.

[9] M. Cikes, L. Tong, G. R. Sutherland and J. D'Hooge, *Ultrafast cardiac ultrasound imaging: Technical principles, applications, and clinical benefits*, 2014. DOI: 10.1016/j.jcmg.2014.06.004.

[10] P. Kellman, C. Chefd'hotel, C. H. Lorenz, C. Mancini, A. E. Arai and E. R. McVeigh, 'High spatial and temporal resolution cardiac cine MRI from retrospective reconstruction of data acquired in real time using motion correction and resorting', *Magnetic Resonance in Medicine*, vol. 62, no. 6, pp. 1557–1564, 2009, ISSN: 15222594. DOI: 10.1002/mrm.22153.

[11] Z. Sun, 'Multislice CT angiography in cardiac imaging: Prospective ECG-gating or retrospective ECG-gating?', *Biomedical Imaging and Intervention Journal*, vol. 6, no. 1, pp. 1–7, 2010, ISSN: 18235530. DOI: 10.2349/biij.6.1.e4.

[12] F. Contijoch, L. Fernandez-De-Manuel, T. Ngo, J. Stearns, K. L. Grogan, M. B. Brady, P. M. Burlina, A. Santos, D. D. Yuh, D. A. Herzka, M. J. Ledesma-Carbayo and E. R. McVeigh, 'Increasing temporal resolution of 3D transesophageal ultrasound by rigid body registration of sequential, temporally offset sequences', *2010 7th IEEE International Symposium on Biomedical Imaging: From Nano to Macro, ISBI 2010 - Proceedings*, pp. 328–331, 2010. DOI: 10.1109/ISBI.2010.5490342.

[13] D. P. Perrin, N. V. Vasilyev, G. R. Marx and P. J. Del Nido, 'Temporal enhancement of 3D echocardiography by frame reordering', *JACC: Cardiovascular Imaging*, vol. 5, no. 3, pp. 300–304, 2012, ISSN: 18767591. DOI: 10.1016/j.jcmg.2011.10.006.

[14] S. Brekke, C. B. Ingul, S. A. Aase and H. G. Torp, 'Increasing frame rate in ultrasound imaging by temporal morphing using tissue doppler', *IEEE Transactions on Ultrasonics, Ferroelectrics, and Frequency Control*, vol. 53, no. 5, pp. 936–946, 2006, ISSN: 08853010. DOI: 10.1109/TUFFC.2006.1632684.

[15] T. G. Haga, 'The Ultrasound Cardiac Supercycle - for high temporal and spatial resolution', 2020.

[16] C. Bruneel, R. Torguet, K. M. Rouvaen, E. Bridoux and B. Nongaillard, 'Ultrafast echotomographic system using optical processing of ultrasonic signals', *Applied Physics Letters*, vol. 30, no. 8, pp. 371–373, 1977, ISSN: 00036951. DOI: 10.1063/1.89436.

[17] D. Shattuck, M. D. Weinshenker, S. W. Smith and O. T. von Ramm, 'Explososcan: A parallel processing technique for high speed ultrasound imaging with linear phased arrays', *Journal of the Acoustical Society of America*, vol. 75, no. 4, pp. 1273–1282, 1984, ISSN: NA. DOI: 10.1121/1.390734.

[18] R. Mallart and M. Fink, 'Improved imaging rate through simultaneous transmission of several ultrasound beams', in *New Developments in Ultrasonic Transducers and Transducer Systems*, vol. 1733, SPIE, Nov. 1992, pp. 120–130. DOI: 10.1117/12.130591.

[19] B. Brekke, L. C. Nilsen, J. Lund, H. Torp, T. Bjastad, B. H. Amundsen, A. Stoylen and S. A. Aase, 'Ultra-high frame rate tissue doppler imaging', *Ultrasound in Medicine and Biology*, vol. 40, no. 1, pp. 222–231, 2014, ISSN: 1879291X. DOI: 10.1016/j.ultrasmedbio.2013.09.012.

[20] M. Tanter, J. Bercoff, L. Sandrin and M. Fink, 'Ultrafast compound imaging for 2-D motion vector estimation: Application to transient elastography', *IEEE Transactions on Ultrasonics, Ferroelectrics, and Frequency Control*, vol. 49, no. 10, pp. 1363–1374, Oct. 2002, ISSN: 08853010. DOI: 10.1109/TUFFC.2002.1041078.

[21] Z. Huang, T. Zhang, W. Heng, B. Shi and S. Zhou, 'RIFE: Real-Time Intermediate Flow Estimation for Video Frame Interpolation', Nov. 2020. arXiv: 2011.06294. [Online]. Available: http://arxiv.org/abs/2011.06294.

[22] H. N. Mirarkolaei, S. R. Snare, A. H. Schistad Solberg and E. N. Steen, 'Frame rate up-conversion in cardiac ultrasound', *Biomedical Signal Processing and Control*, vol. 58, p. 101 863, 2020, ISSN: 17468108. DOI: 10.1016/j.bspc.2020.101863. [Online]. Available: https://doi.org/10.1016/j.bspc.2020.101863.

[23] K. A. Kaproth-Joslin, R. Nicola and V. S. Dogra, 'The history of US: From bats and boats to the bedside and beyond', *Radiographics*, vol. 35, no. 3, pp. 960–970, May 2015, ISSN: 15271323. DOI: 10.1148/rg.2015140300.

[24] C. Doppler, 'Ueber das farbige Licht der Doppelsterne und einiger anderer Gestirne des Himmels.', 1842, ISSN: 1803-1853. [Online]. Available: https://m.ngiyaw-ebooks.org/ngiyaw/wikisource/doppler/Ueber%7B%5C_%7Ddas%7B%5C_%7Dfarbige%7B%5C_%7DLicht%7B%5C_%7Der%7B%5C_%7DDoppelsterne%7B%5C_%7Dund%7B%5C_%7Deiniger%7B%5C_%7Danderer%7B%5C_%7DGestirne%7B%5C_%7Ddes%7B%5C_%7DHimmels%7B%5C_%7DChristian%7B%5C_%7DDoppler.pdf.

[25] F. Duck, ''The electrical expansion of quartz' by Jacques and Pierre Curie', *Ultrasound*, vol. 17, no. 4, pp. 197–203, 2009, ISSN: 1742271X. DOI: 10.1179/174227109X12500830049951.

[26] B. A. Angelsen, *Ultrasound imaging : Waves, signals, and signal processing.* Trondheim: Emantec AS, 2000.

[27] S. D. Solomon, *Essential Echocardiography. A Practical Handbook With DVD.* New Jersey: Humana Press Inc, 2007.

[28] H. Torp, 'Signal processing in Ultrasound Doppler and Color Flow Imaging', vol. 360, pp. 2605–15, 2009. [Online]. Available: http://www.nejm.org/doi/full/10.1056/NEJMoa0903810.

[29] J. Udesen, F. Gran, K. Hansen, J. Jensen, C. Thomsen and M. Nielsen, 'High frame-rate blood vector velocity imaging using plane waves: Simulations and preliminary experiments', *IEEE Transactions on Ultrasonics, Ferroelectrics and Frequency Control*, vol. 55, no. 8, Aug. 2008, ISSN: 0885-3010. DOI: 10.1109/TUFFC.2008.858.

[30] H. Torp, *Color Flow Imaging*, Trondheim, 2010. [Online]. Available: https://folk.ntnu.no/htorp/Undervisning/TTK4165/.

[31] J. R. McClelland, D. J. Hawkes, T. Schaeffter and A. P. King, *Respiratory motion models: A review*, Jan. 2013. DOI: 10.1016/j.media.2012.09.005.

[32] Wapcaplet, Yaddah and License-CC-BY-SA-3.0, *Diagram of the human heart*, 2003. [Online]. Available: https://en.wikipedia.org/wiki/File:Diagram%7B%5C_%7Dof%7B%5C_%7Dthe%7B%5C_%7Dhuman%7B%5C_%7Dheart.svg.

[33] H. Fukuta and W. C. Little, 'The Cardiac Cycle and the Physiological Basis of Left Ventricular Contraction, Ejection, Relaxation, and Filling', Tech. Rep.

[34] DestinyQx, DanielChangMD, Xavax and License-CC-BY-SA-2.5, *Wiggers diagram*, 2012. [Online]. Available: https://commons.wikimedia.org/wiki/File:Wiggers%7B%5C_%7DDiagram.svg.

[35] W. Li, 'Wavelets for electrocardiogram: Overview and taxonomy', *IEEE Access*, vol. 7, pp. 25 627–25 649, 2019, ISSN: 21693536. DOI: 10.1109/ACCESS.2018.2877793.

[36] P. Kellman, C. Chefd'hotel, C. H. Lorenz, C. Mancini, A. E. Arai and E. R. McVeigh, 'Fully automatic, retrospective enhancement of real-time acquired cardiac cine MR images using image-based navigators and respiratory motion-corrected averaging', *Magnetic Resonance in Medicine*, vol. 59, no. 4, pp. 771–778, 2008, ISSN: 15222594. DOI: 10.1002/mrm.21509.

[37] T. Lyche and K. Morken, 'Basic properties of splines and B-splines', vol. 35, no. x, pp. 36–55, 2002.

[38] T. Grønli, M. Wigen, P. Segers and L. Lovstakken, 'A Fast 4D B-Spline Framework for Model-Based Reconstruction and Regularization in Vector Flow Imaging', *IEEE International Ultrasonics Symposium, IUS*, vol. 2018-Octob, no. 1, pp. 2–5, 2018, ISSN: 19485727. DOI: 10.1109/ULTSYM.2018.8579767.

[39] M. Unser, 'Splines: A Perfect Fit For Signal and Image Processing', *IEEE Signal Processing Magazine*, no. NOVEMBER, pp. 22–38, 1999.

[40] J. L. Rodgers and W. A. Nicewander, 'Thirteen Ways to Look at the Correlation Coefficient', vol. 42, no. 1, pp. 59–66, 1988.

[41] S. A. Aase, A. Stoylen, C. B. Ingul, S. Frigstad and H. Torp, 'Automatic timing of aortic valve closure in apical tissue Doppler images', *Ultrasound in Medicine and Biology*, vol. 32, no. 1, pp. 19–27, Jan. 2006, ISSN: 03015629. DOI: 10.1016/j.ultrasmedbio.2005.09.004.

[42] A. Stoylen, U. Wisløff and S. Slørdahl, 'Left ventricular mechanics during exercise: A Doppler and tissue Doppler study', *European Journal of Echocardiography*, vol. 4, no. 4, pp. 286–291, Dec. 2003, ISSN: 15252167. DOI: 10.1016/S1525-2167(03)00008-8.

[43] J. M. Pouget and W. S. Harris, *Systolic time intervals in man*, 1973. DOI: 10.1016/0002-8703(73)90266-4. [Online]. Available: http://ahajournals.org.

[44] L. Zhang, L. Zhang, X. Mou and D. Zhang, 'FSIM: A feature similarity index for image quality assessment', *IEEE Transactions on Image Processing*, vol. 20, no. 8, pp. 2378–2386, 2011, ISSN: 10577149. DOI: 10.1109/TIP.2011.2109730.

Appendix

A Supercycle object initialization

The initialization of the Supercycle showing the possible parameters to tune.

```
class Supercycle:
def __init__(self, filepath, **kwargs):
    # Location of the file
    self.path = filepath

    # A dataloader object (object created from GEDICOM)
    self.data = kwargs.get('data', None)

    # Modality: BMODE, CF, RO
    self.datatype = kwargs.get('datatype', 'BMODE')

    # Decimation factor (int)
    self.downsample = kwargs.get('downsample', None)

    # Normalization method: "none", "whole", "diastole", "diastole_ML"
    self.norm = kwargs.get('norm', 'diastole')

    # Separation method: "ecg_split", "ml_split"
    self.split = kwargs.get('split', 'ecg_split')

    # Number of wanted cycles
    self.n_wanted = kwargs.get('n', 10)
    # Wanted cycles to be joined: list of idx(int) < #recorded cycles
    self.cycle_basis_wanted = kwargs.get('cycle_basis_wanted', [])

    # B-spline order: int
    self.interp_order = kwargs.get('interp_order', 3)

    # B-spline smoothness factor: float >= 0.
    self.smoothing = kwargs.get('s', -1)

    # B-spline period: float
    self.interp_period = kwargs.get('interp_period', 1.)

    # Output time grid: list of times (float)
    self.interp_times = kwargs.get('interp_times', [None])

    # Output target frame rate: int
    self.fps = kwargs.get('fps')
```

B A simple pipeline

A simple pipeline of how to construct the Supercycle showing it as an application is seen at the two next pages.

Import packages

_**Supercycle*construction*** contains the actual procedure of setting up a Supercycle with som chosen parameters and methods as seen in Appendix A.

util contains helping functions such as a data-loader, a cycle object, a cycle ultrasound separator, a cycle ecg separator, a cycle sorting and concatenation method, normalization methods, Tensorspline for remapping procedure, optimal cycle selection, timing and feature extractions from ML, scan convert functions and plotting functions. The data-loader, Tensorspline and ML framework are developed by the ultrasound team at St.Olavs, and adapted for the use in this thesis.

In [1]:
```
from Supercycle_construction import Supercycle
import util
```

Construction of Supercycle for B-mode ultrasound

Load Ultrasound data

Choose whether to load CFI, R0 or BMODE data, and in addition if the data is triplane mode.

In [2]:
```
file = 'C:/Users/Toragh/Documents/Master/ultrasound_data/DP/1'

# Ultrasound datatype: CF, R0, BMODE(default)
mode = "BMODE"

# If wanting to extract triplane data
triplane = False

if triplane:
    # us is a list with three data
    us = util.load_triplan(file, mode)
else:

    bmode, ecg, r1, r0, geo, params, FS = util.load_us(file, mode)

print("Sampling frame rate ("+mode+"): ", FS, "Hz")
```

```
Sampling frame rate (BMODE):  64 Hz
```

Specify Supercycle parameters

Setting the parameters for initialization in the Supercycle object as shown in Appendix A

In [3]:
```
number_of_cycles        = 6
separation_method       = "ecg_split"
normalization_type      = "diastole"
spline_order            = 3
smoothness_factor       = 1e-5
```

Construct the Superycle object with the specified parameters

In [4]:
```
SC_B = Supercycle(file, datatype=mode, n=number_of_cycles, split=separation_method, norm=normalization_type, interp_order=spline_order, s=smoothness_factor)
```

Summarization of parameters and methods for Supercycle

The object provides a simple summary of the chosen parameters and methods for simple supervision of the procedure and recap of the process.

In [5]:
```
SC_B.get_info()
```

```
Dataset:  1
Ultrasound imaging type:  BMODE
Original frame rate[Hz]:  65
Cycle basis size:  6
Cycle basis idx:  [1 2 3 6 7 9]
Mean length of cycles in basis:  1.097 s
Standard dev. of cycles in basis:  0.039 s
Dataset splitted into cycles by 'R' triggers (ECG)
Cycles joined with concatenation and sorting by normalizing diastole
B-spline order:  3
B-spline smoothing factor:  1e-05
Supercycle target fr [Hz]:  390
```

Plot 2D sector and M-mode of Supercycle

The red line in the 2D sector visualize the position of the acquired M-mode.

In [6]:
```
SC_B.sc2_data.shape
```

Out[6]:
```
(428, 182, 735)
```

In [7]:
```
util.plot_mmode(mode, SC_B.sc2_times, SC_B.sc2_data, geo, params)
```

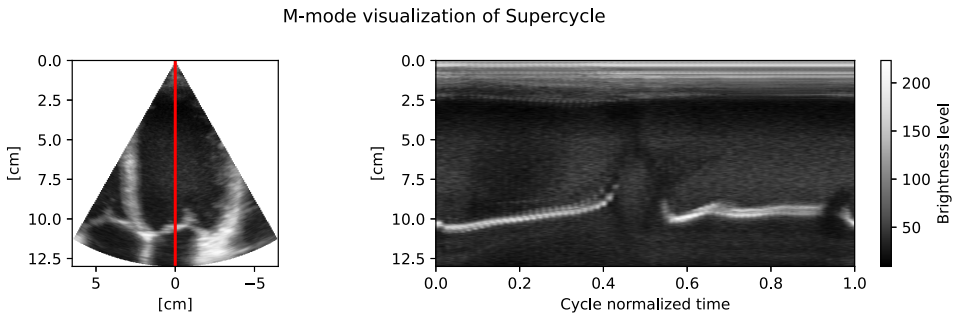

Construction of Supercycle for CFI

Load Ultrasound data

Choose whether to load CFI, R0 or BMODE data, and in addition if the data is triplane mode.

In [8]:
```
file = 'C:/Users/Toragh/Documents/Master/ultrasound_data/DP/4'

# Choosing CFI mode
mode = "CF"

bmode, ecg, r1, r0, geo, params, FS = util.load_us(file, mode)
print("Sampling frame rate ("+mode+"): ", FS, "Hz")
```

```
Sampling frame rate (CF):  26 Hz
```

Specify Supercycle parameters

Setting the parameters for initialization in the Supercycle object as shown in Appendix A

In [9]:
```
# number_of_cycles      = 6
cycle_basis             = [1,2,5]
separation_method       = "ecg_split"
normalization_type      = "whole"
spline_order            = 2
smoothness_factor       = 1e-4
```

Construct the Superycle object with the specified parameters

In [10]:
```
SC_CF = Supercycle(file, datatype=mode, cycle_basis_wanted=cycle_basis, split=separation_method, norm=normalization_type, interp_order=spline_order, s=smoothnes
```

Summarization of parameters and methods for Supercycle

The object provides a simple summary of the chosen parameters and methods for simple supervision of the procedure and recap of the process.

In [11]:
```
SC_CF.get_info()
```

```
Dataset:  4
Ultrasound imaging type:  CF
Original frame rate[Hz]:  26
Cycle basis size:  3
Cycle basis idx:  [1, 2, 5]
Mean length of cycles in basis:  1.07 s
Standard dev. of cycles in basis:  0.031 s
Dataset splitted into cycles by 'R' triggers (ECG)
Cycles joined with concatenation and sorting by normalizing whole
B-spline order:  2
B-spline smoothing factor:  0.0001
Supercycle target fr [Hz]:  80
```

Plot 2D sector and M-mode of Supercycle

The red line in the 2D sector visualize the position of the acquired M-mode.

In [12]:
```
util.plot_mmode(mode, SC_CF.sc2_times, SC_CF.sc2_data, geo, params)
```

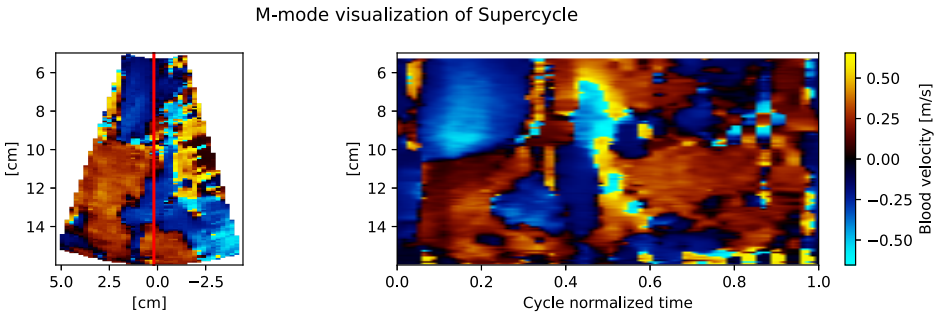

C Datasets

Name	Modes	FR B-mode [Hz]	FR CFI [Hz]	# Cycles	Situation	Mean cycle lenght [s]	Cycle length std.dev [s]
A0	B-mode	65		10	BN	1.041	0.092
A1	B-mode	65		10	NN	1.097	0.037
A2	B-mode	65		10	BH	1.026	0.089
A3	B-mode, CFI	14	27	10	BN	1.084	0.052
A4	B-mode, CFI	14	27	10	NN	1.096	0.030
A5	B-mode, CFI			10	BH	1.044	0.138
A6	B-mode, CFI	14	27	10	BN	1.045	0.041
A7	B-mode, CFI	8	15	10	BN	1.079	0.047
A8	B-mode, Triplan	54		10	BN	1.059	0.042
A9	B-mode, Triplan	54		10	NN	1.118	0.023
A10	B-mode, Triplan	54		10	BH	1.003	0.129
A11	B-mode, CFI, Triplan	14	14	10	BN	0.936	0.038
A12	B-mode, CFI, Triplan	14	14	10	NN	1.057	0.040
A13	B-mode, CFI, Triplan	14	14	10	BH	1.023	0.111
A14	B-mode, CFI, Triplan	15	15	10		0.909	0.029
A15	B-mode, CFI, Triplan	9	9	10		1.036	0.045
A16	B-mode, CFI	12	24	10	HP	0.662	0.044
A17	B-mode	64		10	HP	0.702	0.051
B0	B-mode	70		12		0.986	0.986
B1	B-mode	70		12		0.975	0.093
B2	B-mode	83		12		0.872	0.060
B3	B-mode	83		12		0.833	0.032
B4	B-mode	44		12		0.878	0.047
B5	B-mode, CFI	19	19	12		0.917	0.034
B6	B-mode, CFI	14	29	12		0.864	0.032
B7	B-mode, CFI	14	29	12		0.852	0.033
B8	B-mode, CFI	16	16	12		0.922	0.035
B9	B-mode, CFI	11	11	12		0.973	0.052
B10	B-mode, Triplan	33		12		0.863	0.034
B11	B-mode, CFI, Triplan	15	15	12		0.914	0.023
B12	B-mode			12		0.948	0.058
B13	B-mode			12		0.871	0.043
B14	B-mode			12		0.871	0.043
C0	B-mode	70		12		1.049	0.029
C1	B-mode	83		12		0.995	0.030
C2	B-mode	38		12		1.022	0.030
C3	B-mode	149		12		0.981	0.064
C4	B-mode, CFI	17	34	12		1.044	0.042
C5	B-mode, CFI	18	18	12		1.019	0.034
C6	B-mode, CFI	9	9	12		1.005	0.034
C7	B-mode, CFI	14	14	12		1.077	0.020
C8	B-mode, CFI	14	14	12		1.039	0.037
C9	B-mode, Triplan	30		12		1.093	0.025
C10	B-mode, CFI, Triplan	12	12	12		1.047	0.034
C11	B-mode	15		12		1.010	0.167
C12	B-mode	6		12		1.070	0.042

Table C.1: Overview of the datasets used throughout the study. Some cells lacks information as these were not available. Situation abbreviations: BN = *Breathing normally*, NN = *No breathing*, BH = *Breathing heavily*, HP = *High pulse after activity*

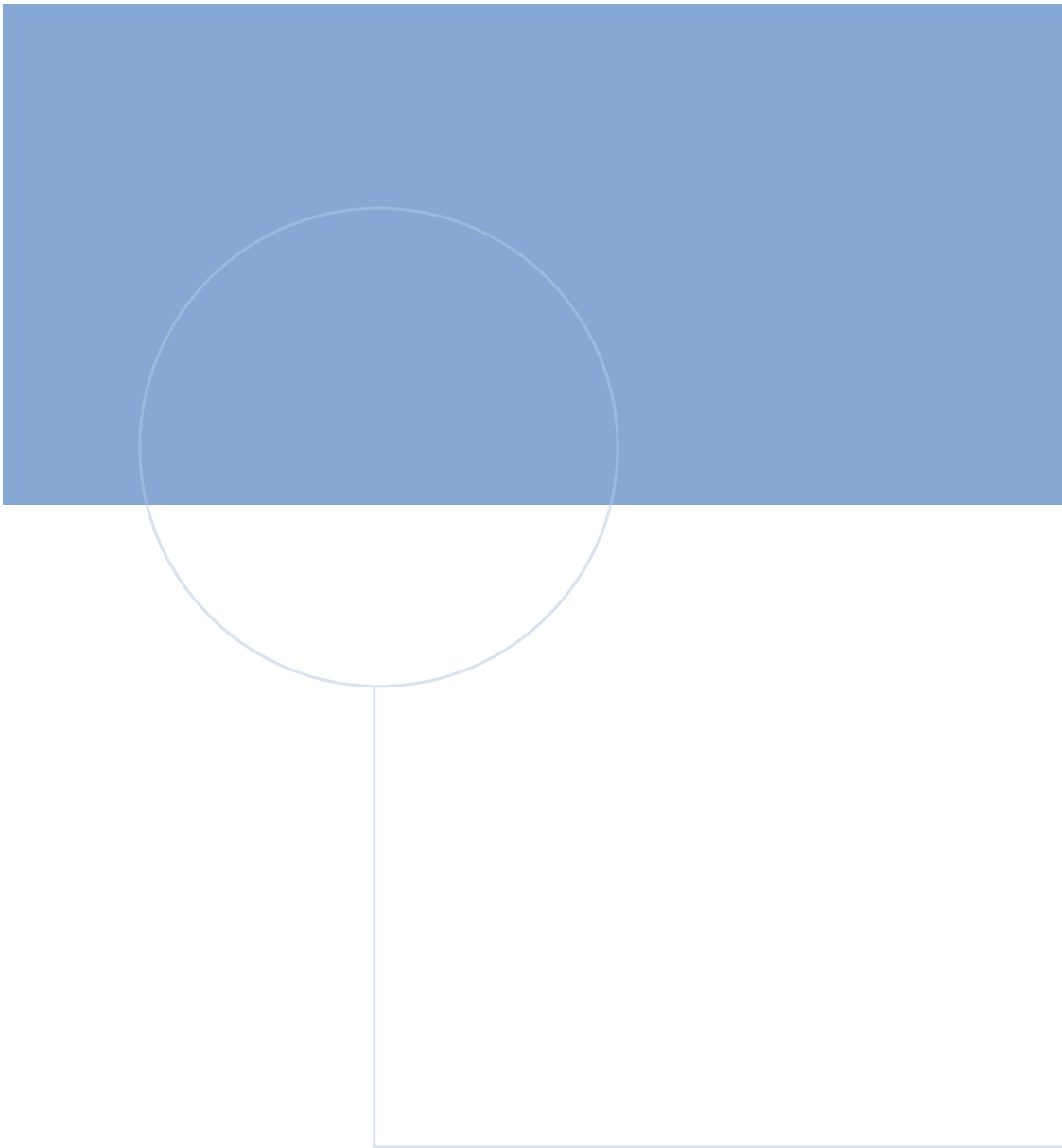

NTNU

Norwegian University of
Science and Technology